MRI ASSESSMENT OF *in vivo* EPIMUSCULAR MYOFASCIAL FORCE TRANSMISSION

by

Alper Yaman

B.Sc., Physics, Boğaziçi University, 2000

M.Sc., Biomedical Engineering, Boğaziçi University, 2003

Submitted to the Institute of Biomedical Engineering

in partial fulfillment of the requirements

for the degree of

Doctor

of

Philosophy

Boğaziçi University

2014

ACKNOWLEDGMENTS

I would like to offer my immense gratitude to my advisors Prof. Cengizhan Öztürk and Assoc. Prof. Can A. Yücesoy for their great help and support. I am grateful to Prof. Peter Huijing for his precious suggestions and Guus Baan for his valuable help while preparing 3D reconstructions. I also would like to thank my master thesis advisor Prof. Mehmed Özkan for his help and to Prof. Ahmet Ademoğlu, Assoc. Prof. Burak Acar, Assoc. Prof. Albert Güveniş, and Prof. Mustafa Karahan for participating in the thesis progress committee, and to my boss Prof. Ahmet Duyar whom I have learned the ways to apply academic research to industry.

I wish to thank my friend Onur Özyurt and MR technicians in Kozyatağı Acıbadem Hospital for their help during MRI experiments, Prof. Alp Dinçer his support, Dr. Dilek Göksel Duru and Dr. Uzay Emrah Emir for discussing diffusion tensor imaging, Bora Büyüksaraç for discussing perfusion, Serkan İnanç and Erhan Uyanık for their help in preparing pilot experimental setups, Ekberjan Derman for his help in image registration, Nermin Topaloğlu, Dr. Ömer Şaylı, Dr. Bilal Biçer and Assoc. Prof. Yaşar Tatar for their valuable support in EMG studies, Assist. Prof. Esin Öztürk Işık and Hüseyin Şimşek for their help in statistics, Assist. Prof. Ümit Uğurlu and Assoc. Prof. Ekin Akalan for their suggestions in orthopaedic materials for experimental setup, Assist. Prof. Rafet Irmak for discussions about manual therapy, and my sister Derya Sema Yaman, MD for discussions about muscle anatomy and physiology.

I would like to thank my friends Tolga Karalar, Murat Günal, Ragıp Gökalp Tülek, Yahya Civelek, Ali Bayram, Aytaç Durmaz, Arda Arpak, Abdülkadir Yazıcı, Umut Ağyüz, Meltem Yorulmaz, Murat Tümer, Emre Özdal, and my brother Ziya Yaman for their support during MRI experiments; and other Bogazici University Medical Imaging Lab (BUMIL) members Özlem Özmen Okur, Esin Karahan Şenvardar, Meltem Sevgi; Biomechanics Lab members Ahu Nur Türkoğlu, Önder Emre Arıkan and especially to Dr. Filiz Ateş for discussions about muscular mechanics, and also

Osman Kaytazoğlu for his guidance about university entrance exam.

Special thanks to Ertuğrul Burteçin Aksel, Dr. Şenol İşçi, Dr. Temel Bilici, Dr. Özgür Tabakoğlu, Alper Öztürk, Gökmen Hurşit Özer, Gökhan Işık, Ozan Erciyas, Dr. Ulaş Başar Gezgin, and Mehmet Yumak for their friendship.

I have always been passionate about science and engineering since my very early childhood. I am very grateful to former technicians in İzmir Çamaltı Tuzlası Technical Department for their support during my studies about electromechanics and robotics, the pharmaceutics who gave me free serum tubes, injectors etc. for my chemistry and biology studies, the butcher who gave me free sheep heart and kidney for my anatomy studies, Abdurrahman Çakmakçı for teaching me electronic circuits, and all my teachers in İzmir Karşıyaka High School for their support.

I would like to express my gratitude and love to my parents Cafer and Ragıbe Yaman, and to my brother Ziya and sisters Dilek Nuriye and Derya Sema Yaman for being such a great and united family. I would like to thank them for being so patient and always supportive even when I disassembled all small electronics at home to examine how they work and failed to assemble, when I accidentally exploded the Hydrogen balloon I made in the kitchen, when I made burns on carpets while I soldered, when I tripped the fuse many times, when I hybridized the white and red roses to get a pink rose, when I worked on stones, dangerous solutions, dead scorpions, bats etc., and when I operated on sheep heart and kidney to observe their anatomy in the kitchen. I would like to thank my parents for buying me a microscope, magnifying glasses, multimeter, soldering iron, and other stuff that were priceless to me. I would like to thank them for sharing my happiness when I built my first working bird-like robot from scratch. And I am really sorry for being such an unmanageable and maverick kid.

Finally, I would like to express my special thanks to my lovely wife Emine for her endless supports and being always by my side. This thesis would not have been possible without her support and patience.

This study was supported by (1) the Turkish State Planning Organization (DPT) under grants 2007K120610 and 2009K120520 to Cengizhan Öztürk, (2) The Scientific and Technological Research Council of Turkey (TÜBİTAK) under grants 107E274 (Cengizhan Öztürk) and 111E084 (Can A. Yücesoy) and (3) The Turkish Academy of Sciences (TÜBA) under Distinguished Young Scientist Award (Can A. Yücesoy).

ABSTRACT

MRI ASSESSMENT OF *in vivo* EPIMUSCULAR MYOFASCIAL FORCE TRANSMISSION

Recent developments have been evolving magnetic resonance imaging (MRI) to a combined tool in order to assess human anatomy and physiology *in vivo*. In the present thesis 3D high resolution anatomic and diffusion weighted imaging capabilities of MRI were combined with nonrigid registration technique in order to quantify principal strains and fiber direction strains locally. The presented method was used to assess the effects of epimuscular myofascial force transmission (EMFT) and external mechanical load simulating ischemic compression manual therapy technique in human lower leg *in vivo*.

In healthy subjects, global length changes of gastrocnemius muscle-tendon complex were shown to cause sizable and heterogeneous local principal strains and fiber direction strains within the all muscles of the limb. It was concluded that EMFT has determinant role in human muscles that affects the mechanical characteristics of synergistic and antagonistic muscles as changing heterogeneity of fiber lengths. Thus it was proven that muscles are not isolated functioning units *in vivo*.

Even all muscles of lower leg were kept isometric, external mechanical load imposed on gastrocnemius muscle caused pronounced and quite heterogeneous principal strains not only within that muscle but also in other muscles of the limb. These findings may lead therapists to relate the mechanical load and the size and penetration of deformations it creates.

Keywords: Epimuscular myofascial force transmission, manual therapy, magnetic resonance imaging, diffusion tensor imaging, nonrigid registration, *in vivo* biomechanics, motion analysis.

ÖZET

EPİMÜSKÜLER MİYOBAĞDOKUSAL KUVVET İLETİMİNİN MRG İLE İN VİVO ANALİZİ

Son gelişmelerle birlikte manyetik rezonans görüntüleme (MRG) insan anatomi ve fizyolojisini araştırmada tümleşik bir araç haline gelmiştir. Bu tezde MRG'nin yüksek çözünürlüklü 3B anatomik ve difüzyon ağırlıklı görüntü alma yetenekleri esnek çakıştırma tekniğiyle birleştirilerek yerel asal gerinimler ve fiber yönü gerinimleri nicellenmiştir. Mevcut yöntem insan alt bacağında epimüsküler miyobağdokusal kuvvet iletiminin (EMKİ) ve iskemik kompresyon manuel terapi yöntemini taklit eden dış mekanik baskının etkilerinin insanda *in vivo* incelenmesi için kullanılmıştır.

Sağlıklı deneklerde gastroknemius kas-tendon kompleksindeki genel boy değişimlerinin aynı uzuvdaki tüm kaslarda büyük ve heterojen yerel asal ve fiber yönü gerinimlerine sebep olduğu gösterilmiştir. EMKİ'nin insanda fiber boyunun heterojenliğini değiştirerek sinerjistik ve antagonistik kasların mekanik özelliklerini etkileyen belirleyici bir rolü olduğu sonucuna varılmıştır. Böylece kasların birbirinden izole halde çalışan birimler olmadığı kanıtlanmıştır.

Alt bacaktaki tüm kaslar izometrik tutulsa bile gastroknemius kasına uygulanan dış mekanik baskı sadece bu kasta değil aynı uzuvdaki diğer kaslarda da çok heterojen ve büyük asal gerinimlere sebep olmuştur. Bu bulgular terapistlere uyguladıkları dış baskı miktarı ve bu baskının dokularda oluşturduğu deformasyon büyüklüğü ve dağılımını ilişkilendirmede yol gösterebilir.

Anahtar Sözcükler: Epimüsküler miyobağdokusal kuvvet iletimi, manuel terapi, manyetik rezonans görüntüleme, difüzyon tensör görüntüleme, esnek çakıştırma, *in vivo* biyomekanik, hareket analizi.

TABLE OF CONTENTS

LIST OF FIGURES

LIST OF TABLES

LIST OF SYMBOLS

T	Tesla
Hz	Hertz
cm	Centimeter
mm	Millimeter
mm^2	Square millimeter
s	Second
ms	Milli second
kg	Kilogram
$\circ$	Degree
N	Newton
π	Pi
∇u	Displacement gradient tensor
u	Displacement vector containing displacements in x- and y- direction
α	Positive weighting factor to avoid instabilities in the algorithm for smal
I	Identity matrix
F	Deformation gradient matrix
E	Strain tensor
V	Volume
ΔV	Volume change
G	Gaussian kernel
T	Translation matrix
R	Rotation matrix
S	Scaling matrix
T_0	Shifting matrix
M	Transformation matrix

LIST OF ABBREVIATIONS

MFT	Myofascial Force Transmission
EMFT	Epimuscular Myofascial Force Transmission
GM	Gastrocnemius Medialis
GL	Gastrocnemius Lateralis
SOL	Soleus
DF	Deep Flexors
PER	Peronei
ANT	Anterior Crural
EDL	Extensor Digitorum Longus
EHL	Extensor Hallucis Longus
TA	Tibialis Anterior
FCU	Flexor Carpi Ulnaris
m. gastrocnemius	Musculus Gastrocnemius
m. soleus	Musculus Soleus
PCSA	Physiological Cross-Sectional Area
BTX-A	Botulinum Toxin Type A
Δl_{m+t}	Muscle-Tendon Complex Length
MVC	Maximal Voluntary Contraction
EMG	Electromyography
MRI	Magnetic Resonance Imaging
RF	Radio Frequency
PD	Proton Density
Cine-PC MRI	Cine Phase Contrast Magnetic Resonance Imaging
TMRI	Tagged Magnetic Resonance Imaging
PCMRI	Phase Contrast Magnetic Resonance Imaging
HARP	Harmonic Phase
DENSE	Displacement Encoding with Stimulated Echoes
SENC	Strain Encoding

Turbo Flash	Turbo Fast Low-Angle Shot
MRE	Magnetic Resonance Elastography
DTI	Diffusion Tensor Imaging
DWI	Diffusion Weighted Image
FA	Fractional Anisotropy
λ	Diffusivity
CT	Computerized Tomography
SNR	Signal-Noise-Ratio
2D	Two Dimensional
3D	Three Dimensional
4D	Four Dimensional
FEM	Finite Element Modeling
IQR	Inter Quartile Range
ref	Reference
SE	Standard Error
SD	Standard Deviation
IPP	Image Position Patient
IOP	Image Orientation Patient

1. GENERAL INTRODUCTION

1.1 Muscle Structure and Intramuscular Connections

Skeletal muscle, also known as striated muscle is composed of very long cells which are called muscle fibers. Their length can reach over 30 cm, elongated within fascicles (i.e. bundles consisting of muscle fibers and surrounding connective tissues). Sarcoplasm (i.e. cytoplasm of a muscle fiber) contains myofibrils which are the contractile units of the fiber. Myofibrils consist of thick and thin filaments (composed largely of the protein myosin and actin, respectively). These filaments are arranged regularly representing the repeating unit of a myofibril called as *sarcomere*. Sarcomere is the smallest unit producing force within a muscle fiber: The contraction is brought about as thin filaments at each end of a sarcomere slides toward each other with the help of cross-bridges extending from thick to thin filaments. According to this *Sliding Filament Theory*, generation of force within sarcomere is explained by the overlap of the filaments. In addition to myosin and actin proteins, there are various types of proteins such as titin, troponin, nebulin, and tropomyosin included in the intracellular space [1]. The extracellular space between muscle fibers contains collagen fibrils constituting a wide web among muscle fibers and other components of the extracellular space. Collagen fibers help to organize the muscles within three different layers: endomysium, perimysium, and epimysium embraces each individual muscle fiber, fascicle, and the whole muscle, respectively. After removing muscle fibers and using electron microscope, Trotter and Purslow demonstrated that endomysial tubes are continues 3D structures (Fig. 1.1) [2]. These tubes are linked to perimysium which is linked to epimysium [3, 4]. These form continuous paths from each muscle fiber to the outside of the muscle.

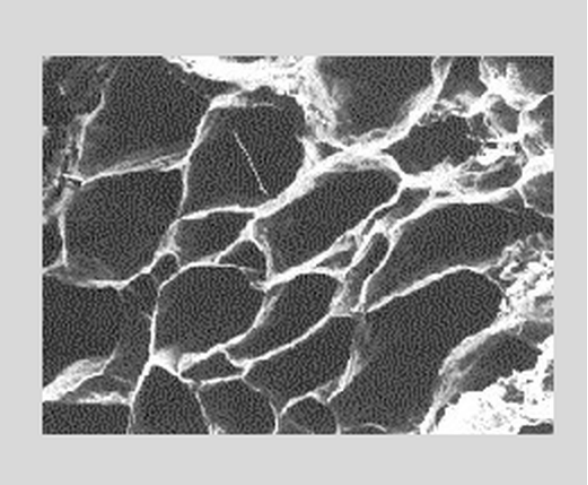

Figure 1.1 Endomysial tunnels. Transversely cut surface of the bovine taken by scanning electron micrograph indicating the endomysial tunnels [2].

1.2 Inter and Extramuscular Connections

The epimysium merges into deep fascia between adjacent muscles and superficial fascia between the muscle and skin. Compartmental Boundaries (e.g. intermuscular septa, interosseal membranes, periostea, and compartmental fascia) bundle the synergistic muscles with shared epimysium. Apart from muscles, bones, and fascia, a limb contains collagen reinforced neurovascular tracts which embed the nerves, blood and lymph vessels. The main nerves and vessels entering the limb branch into each muscle therefore make another continuous pathway among muscles. See Appendix C for detailed 3D reconstructions.

1.3 Transmission of Muscle Force: Myotendinous and Myofascial Pathways

1.3.1 Myotendinous Pathways

In classical point of view, muscles are independent units producing forces and there is little or no force transmission among muscles via intra-, inter-, and extramus-

cular connective tissues. Therefore all forces produced are transmitted onto the bones via tendons by mechanical connections between the ends of muscle fibers and aponeurotic tissue (myotendinous junctions) [5]. Epimysium is merged into the periosteum, the fibrous sheet around a bone directly or through the tendon indirectly [6].

1.3.2 Myofascial Pathways

In addition to the myotendinous junctions there are mechanical linkages among muscles emerging from the proteins within each muscle fiber in cellular level, extends through collagen fibers to macro levels; endomysium, perimysium, and epimysium in order. Taking into consideration these myofascial pathways, the neurovascular tracts and fascia part of a force produced by muscle fibers can be transmitted (i) to adjacent muscle fibers and (ii) between muscles, and (iii) surrounding non-muscular tissues (i.e. bones, neurovascular tracts). It can be transmitted even to more distant muscles within the same limb [7, 8]. Transmission of this kind is referred to as the term "myofascial force transmission" (MFT) introduced by Huijing and his colleagues [9]. The initial studies on EMFT were made on gastrocnemius medialis (GM) and extensor digitorum longus (EDL) muscles of the rat *in situ* [10]. Since EDL muscle has a single proximal tendon and four separate distal ones, it was ideal candidate in order to study myofascial force transmission within intramuscular environment. The subsequent experiments were performed by measuring the length and produced force as extra and intermuscular connective tissues were manipulated systematically [11]. It was shown that the interactions between adjacent muscles and extramuscular connective tissues have direct effect on muscle length-force characteristics. After proximal lengthening proximo-distal force differences were found was caused by these interactions in EDL muscle of the rat [9, 12, 13]. The relation between the size of myofascial force transmission and the relative position of the muscle with respect to adjacent muscles and extramuscular connective tissues was indicated [14]. In the light of these experiments, MFT have been categorized:

1. Intramuscular MFT occurs due to presence of multimolecular complexes which

connect sarcomeres to elements of the subsarcolemmal cytoskeleton which is extended and connected to the extracellular matrix by trans-sarcolemmal molecules [10]. In addition, continuity between intramuscular connective tissues and inter- and extramuscular connective tissues and bones allows the force to be transmitted to the other muscles and non-muscular tissues.

2. Intermuscular MFT is the transmission of force from the extracellular matrix of a muscle to the extracellular matrix of an adjacent muscle via direct collagenous connections [15].

3. Extramuscular MFT is the transmission of force from the extracellular matrix of a muscle to surrounding non-muscular tissues and bone [16, 15]. If inter- and extramuscular MFT connections cannot be distinguished, the integral of inter- and extramuscular MFT is referred to as epimuscular myofascial force transmission (EMFT) [17].

These results were supported by finite element modeling (FEM) in new experiments focused on the anterior crural compartment of the rat [15]. Connective tissues were left intact while those muscles were stimulated. During the experiment, extensor digitorum longus (EDL) muscle was lengthened distally while the length of tibialis anterior (TA) and extensor hallucis longus (EHL) muscles kept constant. The major results of such experiments are:

1. Inter- and extramuscular MFT cause substantial force differences between proximal and distal ends of the muscles [13, 12, 18].

2. Muscle length-force characteristics are altered (e.g., muscle optimum length shifts to a higher length and muscle optimal force is changed) [17, 15].

3. Relative position is a major determinant of muscle force in addition to muscle length [19, 18].

Based on these results, it was hypothesized that if there is force difference between proximal and distal ends of the muscle, the strain and hence distribution of

lengths of the sarcomeres in series should be heterogeneous even if the muscle is kept at constant length. The strain and therefore distribution of lengths of the sarcomeres in parallel are also conceivably heterogeneous because of inter- and extramuscular MFT [15, 20, 18]. This hypothesis was confirmed using FEM. This shows that in addition to physiological parameters (i.e. physiological cross-sectional area PCSA, fiber length, and pennation angle) size and diversity of MFT determines the length-force characteristics of a muscle. However no direct evidence was provided in previous studies.

1.3.3 Implications of EMFT

One of the major implications of EMFT is expected to be in tendon transfer surgeries in patients suffering from spastic paresis. To achieve undesired joint positions, distal tendon of the muscle is detached and reattached to another location in order to balance the load exerted on the joint. Even acute effects of this surgery are as desired, joints turn to their undesired positions in long-term. Using cine phase contrast magnetic resonance imaging (Cine-PC MRI) Asakawa et al. studied on the clinical outcome of rectus femoris transfer surgery which aims to convert rectus femoris muscle from a knee extensor to a knee flexor. They showed that after transfer of distal tendon rectus femoris muscle is not converted to a knee flexor but its capacity on knee extension is reduced ([21, 22]. Smeulders et al. demonstrated that dissecting partially the muscle belly of flexor carpi ulnaris (FCU) from its surroundings achieves better results [23, 24]. In muscle lengthening surgeries Ates et al. showed that EMFT causes (i) differential effects at the proximal and distal ends of a poly-articular muscle, and (ii) sizable effects at non-targeted synergistic muscles [25]. Using previously developed method [26] they concluded that if spastic human muscle is activated alone (i.e. the effects of EMFT are negligible) it does not show abnormal mechanics representing the joint movement disorder. It is indicated that EMFT may affect the abnormality in spastic muscle mechanics [27]. Furthermore, in surgeries targeting spastic muscle with botulinum toxin type A (BTX-A) both injected and noninjected muscles were affected. It indicates the effects of EMFT within the adjacent compartment [28]. It was also shown that BTX-A administration affects EMFT mechanism [29]. Therefore in surgeries based on

tenotomy, fasciotomy, aponeurotomy, and BTX-A injection the role of EMFT should be taken into consideration in order to enhance the outcome of the surgery for both short and long term.

1.4 Compartments of Human Lower Leg

1.4.1 Superficial Posterior Compartment

Biarticular, bipennate musculus gastrocnemius (m. gastrocnemius) is located in posterior compartment with its synergistic musculus soleus (m. soleus) (Fig. 1.2). The medial and lateral heads of m. gastrocnemius originate from medial and lateral condyle of the femur. m. gastrocnemius and m. soleus are attached to Achilles tendon distally. It extends the foot at the ankle joint (i.e. plantarflexion) and flexes the leg at the knee joint. It is supplied by tibial nerve.

m. soleus has three compartments: (i) unipennate posterior compartment, (ii) bipennate anterior crural compartment, and (iii) marginal compartment [30]. The intramuscular aponeurosis (i.e. anterior aponeurosis [31]) separates anterior crural and posterior compartments. Fibers are attached to this aponeurosis proximally from both anterior and posterior sides and contact distally to median septum and posterior aponeurosis of m. soleus [32]. The marginal compartment lies around the periphery of the muscle. It connects the edges of posterior aponeurosis to the edges of anterior aponeurosis, tibia, and fibula. The function of m. soleus is plantarflexion of the foot. Tibial nerve enters m. soleus as two distinct branches from anterior and posterior surface whose distribution within the whole muscle in three-dimension was studied previously [33]. Sural, tibial, and posterior arteries enter m. soleus and m. gastrocnemius. Using ultrasonography, the architecture of m. gastrocnemius and m. soleus was studied and significant differences were found between genders [31]. Because of this, only male subjects were studied in this dissertation.

1.4.2 Deep Posterior Compartment

There are four muscles within this compartment: Popliteus, flexor digitorum longus, flexor hallucis longus, and tibialis posterior (Fig. 1.2). Popliteus muscle acts on knee joint weakly to unlock it. The functions of other muscles are (i) plantarflexion, (ii) inversion of the foot, and (iii) flexion of toes. This compartment is separated from anterior crural and posterior superficial compartments by interosseous membrane and transverse intermuscular septum, respectively. The muscles are attached to interosseous membrane and posterior surfaces of tibia and fibula. They are supplied by tibial nerve and fibular (peroneal) artery and posterior tibial artery.

1.4.3 Peroneal (Lateral) Compartment

There are two muscles within this compartment: Fibularis (peroneous) longus and brevis muscles which plantarflex and evert the foot (Fig. 1.2). This compartment is separated from anterior crural and posterior superficial compartments by anterior and posterior intermuscular septums, respectively. Peroneal muscles are attached proximally to lateral surface of fibula. They are supplied by superficial fibular (peroneal) nerve branching from common fibular (peroneal) nerve and fibular (peroneal) artery which is a branch of posterior tibial artery.

1.4.4 Anterior Crural Compartment

There are four muscles within this compartment: tibialis anterior, extensor hallucis longus, extensor digitorum longus, and fibularis (peroneus) tertius muscles (Fig. 1.2). Their function is (i) dorsiflexion of the foot and (ii) extension of toes. This compartment is separated from deep posterior and peroneal compartments by interosseous membrane and anterior intermuscular septum, respectively. These muscles are attached proximally to tibia, fibula, and interosseous membrane. They are supplied by deep fibular (peroneal) nerve branching from common fibular (peroneal) nerve and

by anterior tibial artery.

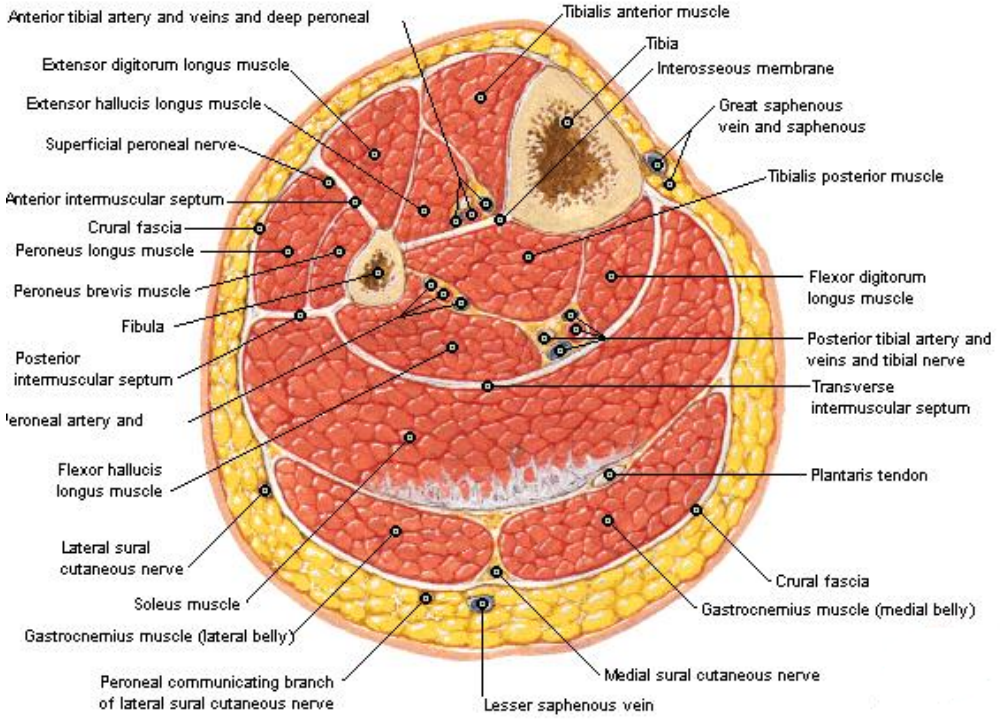

Figure 1.2 Compartments of lower leg. Transversal slice is demonstrated just above middle of lower leg (Courtesy of Netter's Atlas of Anatomy 5th Edition) [34].

1.4.5 Human Lower Leg Compartment Focus of This Dissertation

In this dissertation, lower legs of human subjects were imaged using MRI as the ankle was fixed, knee and hip angles are passively changed. This provides passive movement of m. gastrocnemius while other muscles within the lower leg were kept isometric. In order to assess the effects of this movement on synergistic and antagonistic muscles, we divided lower limb into five anatomical regions: (i) m. gastrocnemius, (ii) m. soleus, (iii) deep flexor muscle group (i.e. muscles in deep posterior compartment), (iv) peroneal muscle group (i.e. muscles in peroneal compartment), and (v) anterior crural muscle group (i.e. muscles in anterior crural compartment).

1.5 Magnetic Resonance Imaging

Magnetic resonance imaging (MRI) is based on the intrinsic angular momentum of the protons in hydrogen atoms generating dipole moments. Normally these dipole moments are randomly oriented and can be aligned under external magnetic field. The precession (i.e. rotation of dipole moments) frequency of this longitudinal magnetization, called also Larmor frequency depends on external magnetic field strength and a constant gyromagnetic ratio. When an external radio frequency (RF) electromagnetic wave with Larmor frequency is applied the protons resonate and create a net transverse magnetization which is orthogonal to longitudinal magnetization direction. When the external magnetic field and RF pulses are turned off protons, start to relax and turn to their random orientations in both longitudinal and transverse directions. While they are returning to their exponential relaxation states they generate electromagnetic wave received by coils in MRI scanner.

Time duration of spin moment relaxations of longitudinal and transverse magnetization depends on two time constants T1 and T2. T1 depends on the interactions between hydrogen protons and the structure of their molecular environment whereas T2 depends on the interactions between hydrogen protons. The physical density of hydrogen protons gives proton density (PD). T1, T2, and PD differ among tissues therefore create contrast in MR images.

Changing the external constant magnetic field with small magnetic field gradients (i.e. phase encoding and frequency encoding gradients) modifies Larmor frequency and phase of the signal which helps to relate the signal with the physical position of protons.

Combination of RF pulses and magnetic gradients is called a pulse sequence in which the timings of RF pulses and gradients were carefully specified. Total duration of measurement specifies if the image is T1 weighted or T2 weighted. These basic types of images have been widely used clinically for visual inspection of anatomy and physiology of soft tissues. Apart from these types of sequences, real-time sequences

have been developed in order to quantify deformations caused by tissue movement. These techniques are especially successful in cardiac motion since they require periodic motion. They are useful also to quantify deformations in skeletal muscles if the subject is able to provide periodic joint movement. These techniques are: (a) tagged magnetic resonance imaging (TMRI) [35], b) phase contrast MRI (PCMRI) [36, 37], c) pulse field gradient based MRI methods (HARP and DENSE) [38, 39], d) strain encoding imaging (SENC) [40]. In this dissertation T1 weighted Turbo Flash based anatomical images are used to quantify deformations using Demons registration.

1.6 Quantifying Deformations

In order to quantify deformations and hence strains within tissues two 3D anatomic high resolution MR image sets are aligned using Demons algorithm [41] i.e., a non-rigid and non-parametric image analysis technique. Utilizing arrays of voxel grayscale values, this algorithm relies on (i) gradients of images and (ii) differences between images i.e., differences between voxel grayscale values of consecutive voxels within each image and corresponding voxels in deformed and undeformed images, respectively. Image differences calculated iteratively are used to characterize displacement values for each voxel. During each iteration, updated displacement fields are smoothed by a Gaussian kernel for regularization of local displacements and global motion. Finally, after a successful alignment of images obtained by minimizing image differences, information on real deformation is available for each cubic shape comprised of four adjacent image voxels. See Appendix A for description of the steps of Demons algorithm.

1.7 Diffusion Tensor Imaging

Diffusion of water molecules in tissues is a random process of translational motion which is called Brownian motion. During diffusion molecules probe tissue struc-

tures beyond usual image resolution [42]. Based on this concept diffusion tensor imaging (DTI) has been developed by encoding diffusion effects with the help of bipolar magnetic field gradient pulses [43].

Gradient terms in diffusion equation derived by Stejskal and Tanner [44] are gathered in a single term referred to as "b value". Diffusion normal to image plane causes signal loss and therefore less contrast in diffusion weighted images (DWI). In order to get 3D information about diffusion one image with zero b value and images with non-zero b value in at least six different orthonormal directions should be acquired.

3D diffusion tensor calculated per voxel gives the information about structural and geometric organizations of tissues. The principal eigenvalue extracted from diffusion tensor indicates the size of longitudinal diffusivity (i.e. diffusivity in local muscle fiber direction) and the corresponding eigenvector is aligned with local fiber direction. This was previously proven in rat calf muscles by direct anatomical inspection using protractor under a dissecting microscope [45] as well as in human muscles [46]. Heemskerk et al. demonstrated that the repeatability of fiber tracking is acceptable [47]. Various fiber tracking algorithms have been developed based on DTI. All these data and fiber tracking are quite beneficial in order to assess the function and structure of soft tissues. Aside from fiber tracking, DTI parameters are useful to explore the injuries in human skeletal muscle [48].

1.8 Goals and Outline of the Dissertation

Previous findings of epimuscular myofascial force transmission were obtained in animal experiments *in situ* and should be verified in human and *in vivo*. Moreover, the hypotheses on sarcomere length heterogeneity has been supported by finite element modeling and such heterogeneity was not made evident experimentally [15, 20, 18].

The aim of this PhD. study is to show the effects of EMFT on muscular mechanics using MRI in human *in vivo*. For this purpose, deformations within the lower leg

are studied and local fiber direction strains are analyzed to show evidence on heterogeneous distribution of sarcomeres. Additionally, the present method is used in order to show the effects of external mechanical loading which simulates ischemic compression.

Chapter 2: Basic information about MRI and real-time MRI techniques to quantify muscle deformations is presented. With the initial results of our manual therapy experiments, it is published as a book chapter:

Ozturk, C., Yaman, A., Yucesoy, C.A. and Huijing, P.A., 2012. Advanced MRI Techniques for *in vivo* Biomechanical tissue Movement Analysis. In: Fascia: The Tensional Network of the Human Body. R. Schleip, T. Findley, L. Chaitow and P. A. Huijing Eds. London, Elsevier Health Sciences imprint Churchill Livingstone: 489-495.

Chapter 3: The present method is used to assess the effects of EMFT on m. soleus. The results are explained in the light of cadaver studies in order to show the differences in passive global motion of the joint and its more pronounced local effects on tissues. It is published as a journal paper:

Huijing, P. A., Yaman, A., Ozturk, C., and Yucesoy, C. A., 2011, "Effects of knee joint angle on global and local strains within human triceps surae muscle: MRI analysis indicating *in vivo* myofascial force transmission between synergistic muscles," Surg Radiol Anat, 33(10), pp. 869-879.

Chapter 4: The present method is used to quantifying deformations caused by passive joint movement is detailed. It is verified against synthetic rigid body motion and imposed known deformations in order to show that the method developed is useful and proper for the analysis of deformations within the whole lower leg muscles in human *in vivo*. The limitations of the method are indicated. It is published as a journal paper:

Yaman, A., Ozturk, C., Huijing, P. A., and Yucesoy, C. A., 2013, "Magnetic resonance imaging assessment of mechanical interactions between human lower leg muscles *in vivo*," J Biomech Eng, 135(9), pp. 91003-91009.

Chapter 5: Using DTI the present method is extended to gain the capability of (i) quantifying strains in local fiber directions, (ii) to assess the changes in longitudinal diffusivity and fractional anisotropy (FA), (iii) to relate the fiber length heterogeneity with longitudinal diffusivity.

Chapter 6: The present method is used in order to quantify the effects of external mechanical loading. This type of loading simulates ischemic compression manual therapy technique. The effects of EMFT in penetration of deformations within deeper muscles are discussed, as well.

At the time of the submission of this dissertation, manuscripts for the last two chapters were not published yet.

Chapters (2-6) are all organized in such a way that they could be read independently. Small changes are made and additional figures are presented so they could differ slightly from their submitted manuscript form to combine all the results in this dissertation format.

Chapter 7: The relevance and implications of this dissertation are discussed in order to describe future studies.

2. ADVANCED MRI TECHNIQUES FOR *in vivo* BIOMECHANICAL TISSUE MOVEMENT ANALYSIS

2.1 Introduction

If a moving body can be observed directly (whole body or its extremities), surface markers can be used and commercially available movement analysis systems (e.g., for gait analysis) exist for biomechanical analysis. Our focus in this chapter is on much more detailed quantitative analysis of moving tissues inside the body using magnetic resonance imaging (MRI).

MRI has sufficient soft tissue contrast and ability to view into different compartments, so it is ideal for and utilized heavily in routine anatomical soft tissue imaging. In recent years, with combined advances in fast imaging hardware, innovative movement imaging protocols and advanced computational image processing tools; dynamic musculoskeletal imaging moves more and more into the mainstream of clinical imaging practice. Although most of its current use remains qualitative: just showing 2D or 3D image sets in series as movies, practical techniques for detailed quantitative biomechanical analysis of moving tissues are available today, for inquisitive clinicians and for researchers who are trying to unravel delicate relationships between soft tissue components during locomotion *in vivo*.

In the past, dynamic motion imaging utilized clinically inapplicable methods, such as 3-D X-Ray stereophotogrammetry that required insertion of metal balls into the bones [49]. Computerized tomography (CT), with recent advances in its hardware and speed, could be utilized for the same purpose, if the focus is predominantly on the bones [50]. CT with advanced post-processing tools eliminates the need for implantable markers; however, X-ray dose becomes critical when multiple 3D datasets are needed. In comparison, ultrasound imaging produces relatively low resolution images for soft tissue movement analysis with modest contrast only at some of the tissue boundaries,

but its use is much cheaper.

MRI, without ionizing radiation effects, is ideal for repeated and prolonged experiments, routinely required in musculoskeletal research. The basic principle is that molecules (e.g. hydrogen nuclei) acting like dipoles (their top-like movement is referred to as spin) are aligned by a static magnetic field and, by dynamic high-frequency radio signals, specific molecules are given special magnetic properties which can be imaged. Since these magnetic properties are temporary real tissue properties that can be used to study dynamic change of the tissues. MRI has an additional advantage that images can be acquired at positions and orientations defined by the user; as long as the subjects are not claustrophobic and the planned movement can be performed within scanner's confined spaces. Ongoing efforts of providing non-claustrophobic machines (such as open magnets) will help dynamic musculoskeletal imaging only in a limited way, since most of such systems suffer from signal-to-noise limitations due to their low static magnetic fields (yielding lower temporal and/or spatial resolution). Newer short- and wide-bore magnets with 1.5 T or higher magnetic fields provide some marginal solution, since movements are still restricted. Standing during MR imaging, most exercise routines and weight bearing is still not common practice except with few specialized systems [51] or creative solutions. Most of the time, equipment costs (both at startup and maintenance) and expertise required for its advanced utilization are the real limitations of dynamic MR imaging.

This chapter is divided into three additional sections: (1) introductory information about MR image formation. Also, it gives a brief overview of classical musculoskeletal movement imaging and tools utilized to analyze these dynamically acquired image sets. (2) a case study, involving aspects of therapeutic-like loading. (3) introduction of some more advanced movement imaging techniques, allowing *in vivo* measurements of local tissue displacement, velocity and even strain.

2.2 Dynamic MRI and *in vivo* Movement Analysis

Routine MR imaging is usually a slow process; image information is gathered step by step by collecting a set of signals (echoes) at different excitation scenarios. At each step, unique phase and frequency information is embedded on the individual signals based on their physical locations which later helps their actual coordinate identification. The combined signals are filled one echo at a time into the "k-space" and the image is obtained via Fourier transformation [52]. Since different echoes are obtained at different times, movement of the tissues could produce significant artifacts within images. Therefore, in routine MR imaging, movement is not welcomed; for example, cardiac MRI should deal with heart and respiratory motion during the image acquisition: first approach is acquiring consecutive images as rapidly as possible ("real-time" MRI) and second approach is segmented k-space imaging [53].

Real-time MRI has limited spatial resolution (due to the limited number of k-space lines that can be acquired at a give time), and relatively poorer temporal resolution (typically 50-300 ms depending on spatial resolution). Improvements are achieved using echo-planar techniques (i.e., collecting several k-space lines per excitation [54], by using longer and more exotic (e.g. spiral) k-space readout trajectories [55] and by employing parallel imaging techniques requiring multiple receiver coils [56], each with varying signal-noise-ratio (SNR) penalties.

Segmented k-space imaging is used extensively in cardiac imaging, permitting the acquisition of a set of images at multiple cardiac phases over the course of several heartbeats in a single ECG-gated, breath-hold scan. The main idea is to repeat the task and synchronize image acquisition and task repetition. This is achieved by partitioning the k-space data matrix into several "segments". The data of each k-space segment is acquired at a single repetition and successive segments are acquired in following repetitions (heartbeats). The image is effectively an average of all repetitions but could provide a series of temporal snapshot of a repetitive motion. The temporal resolution can be improved by reducing the segment size, at the price of increased number of repetitions and total imaging time. Segmented k-space imaging techniques employ

interpolation techniques to adjust for slight variations in the cyclic heart motion [57]. Please note that heart movements can usually be considered as reliably repeatable, but this is not the case for some dynamic musculoskeletal movements. For further reading on fast imaging techniques, the reader is referred to one of several review articles, focusing mostly on cardiac implementations [58]. Historically, heart movement analysis, especially the left ventricle, has been the main model focus. Generic deformable surface models [59], models exploiting curvature information [60], 4D models with temporal constraints [61] have been described previously for cardiac analysis.

In musculoskeletal imaging, detailed kinematical models are built using MRI-derived 3D structures. For example, the peritalar joint complex is analyzed *in vivo* using 3D data sets acquired during foot movement at eight positions, ranging from extreme pronation to extreme supination [62]. Similarly, shoulder kinematics is examined using sequential increments of arm endo-exorotation and comparison to 3D models of glenoid and humerus [63]. Other examples are movement analysis of the spine [64], patella [65], wrist [66] or building models for general locomotion [67].

Another set of applications of dynamic MRI involves detailed evaluation of internal movements occurring physiologically or in pathological conditions. For these applications, subjects are asked to perform certain maneuvers (e.g., straining) while inside the magnet, and newly acquired images are compared with control images (e.g. in assessment of pelvic floor defects [68]). Although the aim is to confirm initial diagnoses and evaluate the anatomy of defects of deeper structures, detailed quantitative analysis using the advanced techniques (previous section) could be performed in almost all cases, when needed.

The standard method of kinematics is to follow objects using temporal sequence of 2D and 3D data sets. All of these registration techniques utilize 4D datasets (3D surfaces or volumes plus time) are essentially similar among all imaging techniques. However, due to its intrinsic and "tunable" high tissue contrast and progressively improving spatial and temporal resolution, all registration-based movement modeling approaches are easier to implement for MRI. From these images, boundaries and edges

of target tissues are first identified by tissue segmentation techniques and subsequently tracked using standard object registration methods. As an alternative, volumes could be tracked solely using image intensity information; our study employs one of these techniques.

2.3 Using MRI to Quantify Deformations Caused by Mock Manual Therapy

3D high resolution magnetic resonance image sets were analyzed to quantify tissue deformations caused by therapeutic-like loading (e.g., Graston Technique [69]) of the human lower leg *in vivo*.

2.3.1 Methods

Five healthy subjects (male, 27 ± 3 years old, height = 175 ± 7 cm and weight = 73 ± 8 kg) participated were positioned prone in 3T MRI scanner. The target leg (left) of the subjects was brought to a reference position: the ankle angle was fixed at 90° using an MRI compatible ankle-foot orthosis. In the initial (i.e. *undeformed* state) 3D high resolution MR image sets were acquired. Subsequently, a rigid cylindrical indenter (diameter = 2.5 cm) was pressed against the posterior lower leg) to create comparable surface indentation (8.33 ± 2.07 mm) causing application of forces normal to mid-gastrocnemius region (Fig. 2.1a), predominantly loading its lateral head. A second image set was acquired in the *deformed* state.

Demons algorithm [41] was used to determine corresponding voxels in the images and their displacements. After calculating the strains for each voxel (size = 0.8 x 0.8 x 0.8 mm) principal strains representing peak local lengthening and shortening (predominantly first and third principle strains, respectively) were determined. It should be noted that the principal strain data is data that has been recalculated (actually the data matrix is rotated), so that shear strains are no longer present. A slice group con-

sisting of 30 consecutive axial slices was selected (Fig. 2.1b) for each subject such that the volume considered includes in the middle the cylindrical indenter. Within each slice, five anatomical regions representing muscles/compartments were distinguished by outlining their boundaries: m. gastrocnemius, m. soleus, deep flexors, peroneal and anterior crural compartment (Fig. 2.1c). For each anatomical region separately, the principle strains for all subjects were pooled and the mean ± standard error (SE) were calculated. The inter-quartile range (IQR) values for the box & whisker plots are considered as measures of strain heterogeneity within anatomical regions.

2.3.2 Results

Both the first and third principle strains within the m. gastrocnemius targeted directly by therapeutic loading were substantial: the first and third principle strains equaled 44% ± 8% and -17% ± 2% (mean ± SE), respectively. This indicates that manual therapy may cause very high length changes within soft tissues immediately within the treatment vicinity. Note, however, that, the principle strains within deeper m. soleus were also substantial: the first and third principle strains equaled 32% ± 9% and -17% ± 2% (mean ± SE), respectively. A remarkable finding is that effects of mock-therapeutic loading remains sizable even for tissues more distant to the location of intervention: (1) within tissues of the deep flexors, local lengthening (mean ± SE) was 16% ± 1% and local shortening -15% ± 5%, (2) within the tissues of the peroneal compartment these values were 17% ± 6% and -11% ± 3% respectively and (3) within the tissues of the anterior crural compartments 21% ± 10% and -10% ± 4% respectively. Note that local lengthening effects of such loading are profound in directly targeted m. gastrocnemius and drop at least by half at more distant locations, but remain sizable nevertheless. In contrast, the reduction in the local shortening effect remains rather limited at larger distances throughout the lower leg cross-section.

The present results show also the heterogeneity of the first and third principle strains (see Fig. 2.1d for a representation of variation of the first principle strains within each anatomical region studied). The IQR values of the principle strains were

high not only for the target muscle (0.68 and 0.21 for the first and third principle strains, respectively) but also for the synergistic m. soleus (0.44 and 0.15 for the first and third principle strains, respectively). This shows that therapeutic loading causes highly heterogeneous length changes for the tissues near the indenter. However, such effects are less heterogeneous for the tissues more distant tissues: (1) IQR values for the first and third principle strains, respectively equaled: (1) 0.17 and 0.14 for deep flexor, (2) 0.19 and 0.17 for peroneal and (3) 0.18 and 0.08 for anterior crural compartments.

This MRI analysis shows that the method developed allows detailed quantification of deformations caused by manual therapies within both muscular and non-muscular tissues. This may help improving the, so far fairly limited, understanding of acute effects of such treatment and can lead to more detailed consideration of its mechanisms. It is concluded that therapeutic loading causes sizable length changes not only within tissues in the immediate vicinity of the location of loading but throughout the cross section. This makes also deformation at other levels within entire lower limb likely and this may need special attention: (1) the therapist may have a higher control over the outcome by realizing where actions may also cause mechanical effects. (2) Such widespread effects also suggest the importance of epimuscular myofascial force transmission in the mechanical effects of manual therapies which needs to be assessed in new studies.

2.4 Advanced Motion Imaging Tools of MRI

MRI is an imaging modality that with some controlled changes in molecular magnetic spin properties (via precise timing of sequential steps of appropriate application of radiofrequency excitations and gradients) unique tissue movement imaging can be achieved *in vivo*. These techniques are: a) tagged magnetic resonance imaging (TMRI), b) phase contrast MRI (PCMRI), c) pulse field gradient based MRI methods (HARP and DENSE). d) strain encoding imaging (SENC). This is an active research area in basic MRI research and below we will introduce each technique briefly.

Conceptually, the simplest imaging technique for analysis of tissue movement is TMRI, where temporary magnetic fiducial markers, or *tags*, are created within tissues, and when imaged after a certain time, the shape changes of these tags reflect the underlying tissue motion. The parallel plane stripe pattern and the combination of two orthogonal plane tags forming a grid are the most common tags [70] (Fig. 2.2).

PCMRI is another approach to tissue movement analysis based on the sensitivity of the phase of the MR signal to motion. It was used mainly for blood flow measurements, but stronger gradients can be used to obtain tissue velocity per voxel (and subsequently local strain-rate and strain) measurements of muscles in segmented acquisitions such as for the myocardium. The basic principle is to acquire two datasets with two different velocity-encoding gradients, but otherwise identical acquisition parameters, and to subtract the two phase images. The resulting difference image will be proportional to the flow (or tissue movement) if the fluid (or underlying tissue) can be assumed to have a constant velocity during the acquisition window. The velocity field for a given image or space at different temporal snapshots can then be integrated to yield tissue displacement [71] (Fig. 2.2).

In DENSE and HARP, a uniform pattern of phase modulation is encoded into the tissue at a chosen time, and the deformation of that pattern is detected at a later time and utilized to estimate the motion [72, 38]. In SENC, a pattern similar to tagging is encoded into the tissue, and the strain in through-plane direction is directly measured by acquiring two images having different z phase encodes [40] (Fig. 2.3).

Currently, dynamic MR imaging of the musculoskeletal system is usually performed in dedicated or open MR systems. With advancing imaging technologies, low-field MRI systems claim now specificity and sensitivity that are comparable to high-field systems in identifying musculoskeletal pathologies. These low field systems allow also wide range of dynamic studies; these are routinely analyzed only visually or using surface-based motion-tracking techniques.

MRI can do much more than providing detailed anatomic images, as was shown

in our study. Advanced MRI techniques have the ability to yield even more direct quantitative tissue movement data. These are unique to MRI and are in sharp contrast with the movement analysis, which is derived from surface or volume matching techniques. We believe in the future there will be more and more dynamic musculoskeletal studies and significantly more utilization of advanced techniques that are unique to MRI.

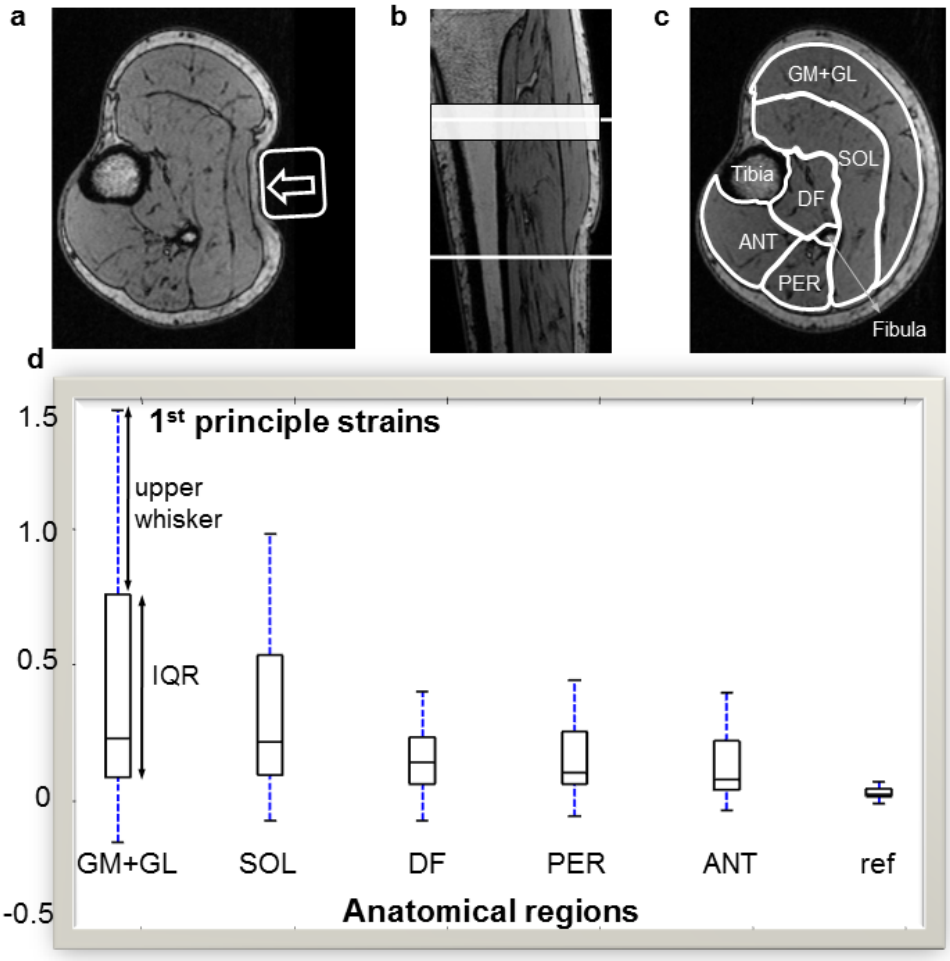

Figure 2.1 (a) The undeformed tissue marked for muscles/compartments considered: i) m. gastrocnemius (GM+GL), ii) m. soleus (SOL), iii) deep flexor compartment (DF), iv) peroneal compartment (PER) and v) anterior crural compartment (ANT). (b) The proximo-distal location of 30 consecutive axial slices studied. (c) The lower leg was loaded by pressing a cylindrical indenter (box with arrow) against the posterior leg. The cross-sectional image shows deformed contours of the calf area, but also deformation of other areas can be seen. (d) Box & whiskers plot of the first principle strains for each anatomical region. Reference data (ref) calculated by imposing rigid body motion quantifies the error of the strain calculation method. Small reference strain values (0.041 ± 0.006) indicate the methods' success. Note that high inter-quartile range (IQR) values calculated for passive m. gastrocnemius and m. soleus indicate strain heterogeneity in those muscles. The maximum value of first principal strains in each anatomical region is denoted by top edge of the upper whisker (dashed line above the box). The horizontal line in a box represents median value.

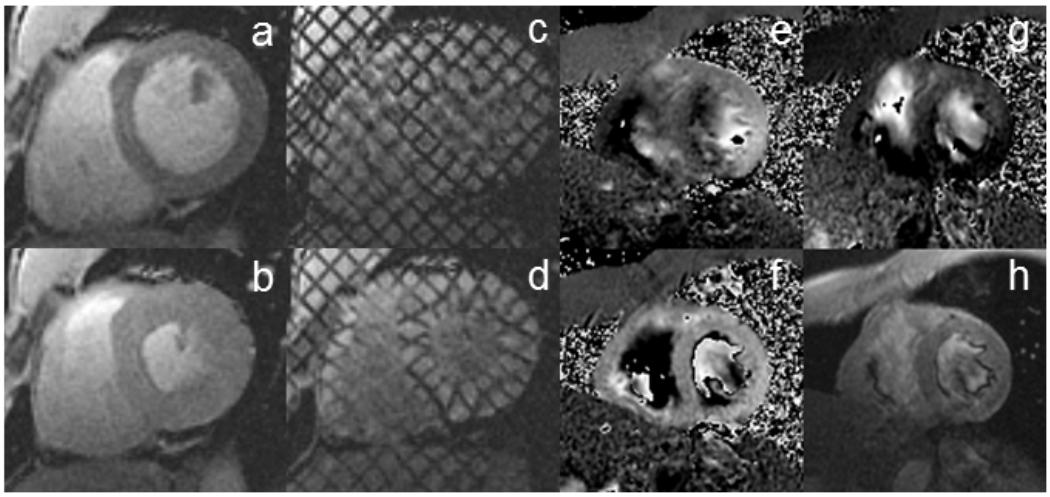

Figure 2.2 Advanced Motion Imaging Using TMRI and PCMRI. Normal cardiac cine MR image examples before and after the heart contraction (a,b). Same images when tags are laid just before contraction showing internal muscular patterns (c,d). Cardiac PCMRI images at mid contraction, where intensity on phase images is proportional to the tissue velocity in the horizontal (e), vertical (f), through-plane (g) directions and the corresponding anatomic image (h). (PCMRI images are courtesy of Richard Thompson, NHLBI, NIH)

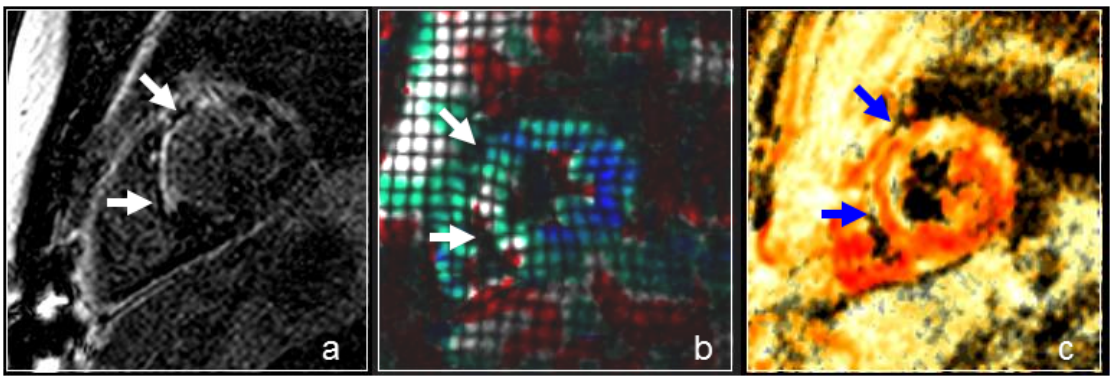

Figure 2.3 Advanced Motion Imaging Using SENC. Images of a subendocardial infarct in a short axis heart image as seen by: A) delayed enhancement MRI (arrows pointing contrast holding and more white looking infarct extent), B) Tagged MR imaging showing decreased function at the infarct zone (circumferential strain is overlaid; Blue color indicates normokinesia; green, hypokinesia; white akinesia) and C) SENC image, color indicating through-plane contraction (Red indicates normokinesia). Notice the subendocardial dysfunction (white color) matching that of the infarcted region but accompanying normal mid endocardiac contraction (red color). SENC seems to show more regional functional differentiation. Images are courtesy of Nael F. Osman, Johns Hopkins University & Nile University.

3. EFFECTS OF KNEE JOINT ANGLE ON GLOBAL AND LOCAL STRAINS WITHIN HUMAN TRICEPS SURAE MUSCLE: MRI ANALYSIS INDICATING *in vivo* MYOFASCIAL FORCE TRANSMISSION BETWEEN SYNERGISTIC MUSCLES

3.1 Introduction

During the last decade, *in situ* animal experiments involving unusually minor dissection of muscles (for reviews see [73, 74]) have indicated that, in addition to myotendinous force transmission, transmission of forces also occurs via alternative pathways, between muscles and between muscle and nonmuscular tissues. First force is transmitted onto the connective tissue of the stroma of the muscle (possible along the full perimeter along length of muscle fibers), *in vivo*, there will be several paths available for further transmission, so that not all force will be exerted at the muscle own tendons. The relative stiffness of the paths determining the fraction of force transmitted via them. Via the epimysium force may be transmitted directly between synergistic muscles, but this may also occur via indirect pathways involving the neurovascular tract (defined as the collagen reinforcements of blood vessels, lymphatics and nerves). It is the relative stiffness of neurovascular tracts that make them particularly fit for such transmission. In addition to intermuscular effects also force transmission between muscle and nonmuscular structures are expected. Also in this process the neurovascular tract may play an important role, as it is not only connected to muscle, but also via the periost to bones (in casu: tibia and fibula), either directly or via other fascial structures to which it may be connected (such as interosseal membrane, intermuscular septum or even the general fascia).

For humans such transmission has been confirmed by similar *in situ* experiments performed during an experimental interval of tendon transfer surgery on patients suf-

fering from spastic paresis [23, 75, 76, 77, 78, 79]. However, evidence for *in vivo* occurrence of such so called myofascial force transmission has been limited to, otherwise unexplained, forces exerted by small hand muscles [80].

The application of *in vivo* non-invasive imaging methods to this problem has been indicated as a potentially promising method (e.g. [12]) to address this question of *in vivo* importance of myofascial force transmission. Such methods are not only expected to be useful in healthy persons for the *in vivo* of physiological mechanisms, but also in patients with various afflictions with some muscular involvement. Here, the novel ideas of myofascial force transmission may yield new ways of looking at functional consequences of the pathology.

The purpose of the present work is, as a first step in this process, to test if magnetic resonance imaging methods, can be applied successfully and combined with mechanical engineering methods to test the hypothesis of *in vivo* myofascial force transmission occurring between synergistic muscles, and if so consider effects of such transmission. One of the features to be expected, if this is found to be the case, is that global strain imposed on the muscle-tendon complex by joint movement and local strains occurring with muscle will be quite different.

For that purpose, additional work was performed also on legs of human cadavers to quantify global strain on gastrocnemius muscle by movement of the knee, using a novel method of dissection involving the excision of major neurovascular tracts from the leg.

3.2 Methods

3.2.1 Cadaver Study: Length Change of Gastrocnemius Muscle Tendon Complex

3.2.1.1 Materials. Seven human cadavers (3 females, 4 males) were studied. These persons had legally arranged that their bodies were to be donated after death to the Vrije Universiteit for purposes of teaching and research. The cadavers were selected based on availability, but special attention was paid to obtain cadavers of a range of different body sizes. Shortly after death and well prior to the start of this project, the cadavers had been fixed by perfusion of a formaldehyde solution into their left femoral artery and subsequently the whole body was kept in a bath of formaldehyde-based bathing solution for at least 6 months.

3.2.1.2 Dissection and Preparation. Hemi-pelvectomy was performed on the fixed cadaver (frozen particularly for this purpose to prevent deforming the soft tissues too much) and the whole leg with half of the pelvis still attached was removed from the body and allowed to thaw. From such isolated legs, the skin and subcutaneous fat tissues were removed. After fasciotomy, the crural fascia and fascia lata were removed, exposing the muscles.

Muscles and muscle parts were dissected by severing intermuscular connective tissues. Major blood vessels and nerves and their major branches were removed, including the collagen fiber reinforcement of such neurovascular tracts. These tracts are very stiff even in living limbs, due to their collagen reinforcements and may even become stiffer due to fixation and they limit movement of the muscles in cadavers as a consequence. In addition it should be noted that for living animals these neurovascular tracts are considered as a major path for myofascial force transmission and the inter muscular interaction, that is a consequence of such transmission [11, 12, 16, 73, 74, 81].

In order to allow further creation of sufficient movement in the knee joint, both

heads of m. gastrocnemius were transected approximately at the middle of their muscle bellies. After dissection, a tube of Bandafix, a wide mesh elastic gauze bandage, was slipped around the leg to hold the muscles together in their original position.

In contrast to previous work with similar purposes [82] and [83], no muscles or parts thereof were removed and the joint capsules were left fully intact. After these preparatory actions, the leg was mounted in the experimental set up (Fig. 3.1) and the knee angle set to the values required.

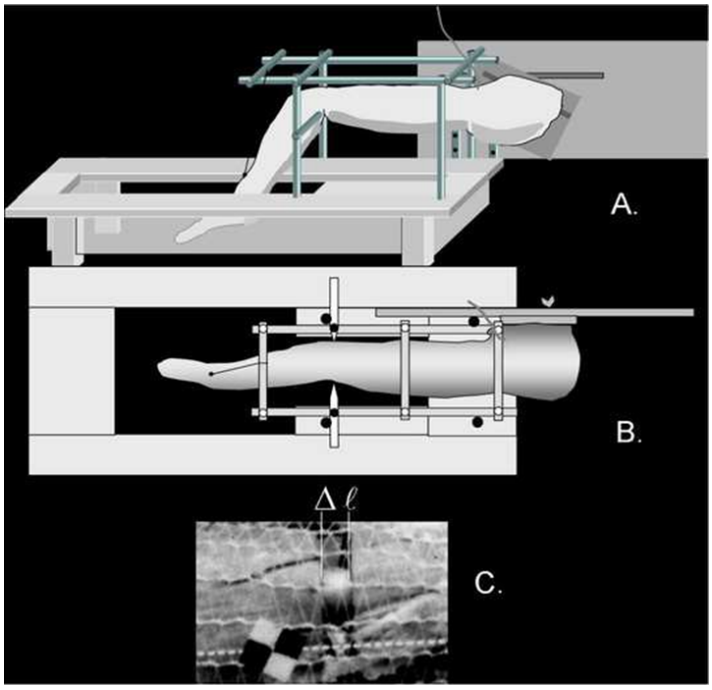

Figure 3.1 Schematic of the setup of the cadaver leg experiment. a) *Lateral view* of the leg mounted in the setup. The leg was suspended from a system of bars. Fixing the hip angle, the board attached to the pelvis was attached to a vertical board on the table. b) *Top view* The femur was fixed by pins at the epicondyles. The knee angle could be changed using the string attached to the tibia. c) Photograph of part of a muscle during the experiment. To keep muscles at their original position, the dissected leg was surrounded with an open-weave stocking, still allowing a good view of the muscle under study. The muscle was cut transversely upon which cut ends retracted somewhat (Δl). With changes of knee angle, changes of this value from its reference level (i.e. at a knee angle of 135°) are a measure of length changes of the muscle tendon complex

The essence of determination of muscle tendon complex length changes after knee angle changes were similar as used in those studies cited above: measuring changes in gap length between transected ends of the muscle with knee angle changes (e.g. Fig. 3.1c).

Segment length of the lower leg was defined as the perpendicular distance between the lateral aspect of the knee joint cavity and the lateral tip of the lateral malleolus. All measurements were performed by one experimenter to avoid interindividual experimenter variation effects on the measurements.

3.2.1.3 Treatment of Data. All changes in muscle-tendon complex lengths (Δl_{m+t}) were calculated as the deviation from the gap value at the reference positions (i.e. a knee angle of 135°, with 180° representing the fully extended knee) and normalized for segment length.

Such data was least square fitted using the following polynomial equation:

$$\Delta l_{m+t} = A_n \Phi^n + A_3 \Phi^3 + A_2 \Phi^2 + A_1 \Phi + A_0 \tag{3.1}$$

In 3.1, ϕ represents the knee joint angle (degrees) and A_n to A_0 are constants determined in the fitting procedure.

Progressively higher order polynomials (maximally sixth order) were fitted to the joint angle length change data of each individual gastrocnemius head, until no statistically significant improvement of the description of the specific data set could be obtained.

3.2.2 MRI Analysis

3.2.2.1 Subjects. As this part of the experiment was performed in Istanbul, experimental procedures were in strict agreement with the guidelines and regulations concerning human welfare and experimentation set forth by Turkish law, and approved by a Committee on Ethics of Human Experimentation at Boğaziçi University, Istanbul. Five healthy subjects (male, 27 ± 3 years old, height = 175 ± 7 cm and body mass = 73 ± 8 kg) volunteered for this study. In order to minimize anthropometric differences

between subjects, only males were recruited. After a full explanation of the purpose and methodology of the experiments, the subjects gave their informed consent.

3.2.2.2 Experimental Protocol. During the experiment, each subject was positioned prone in the MRI scanner. The target (left) leg of the subject was brought to a reference position: (1) the ankle angle was fixed at 90° (Fig. 3.2) by using an MRI compatible ankle-foot orthosis. (2) The knee angle in this prone position with fixed ankle angle (referred to as the *undeformed state*) was (mean ± SD) 173 ± 3.

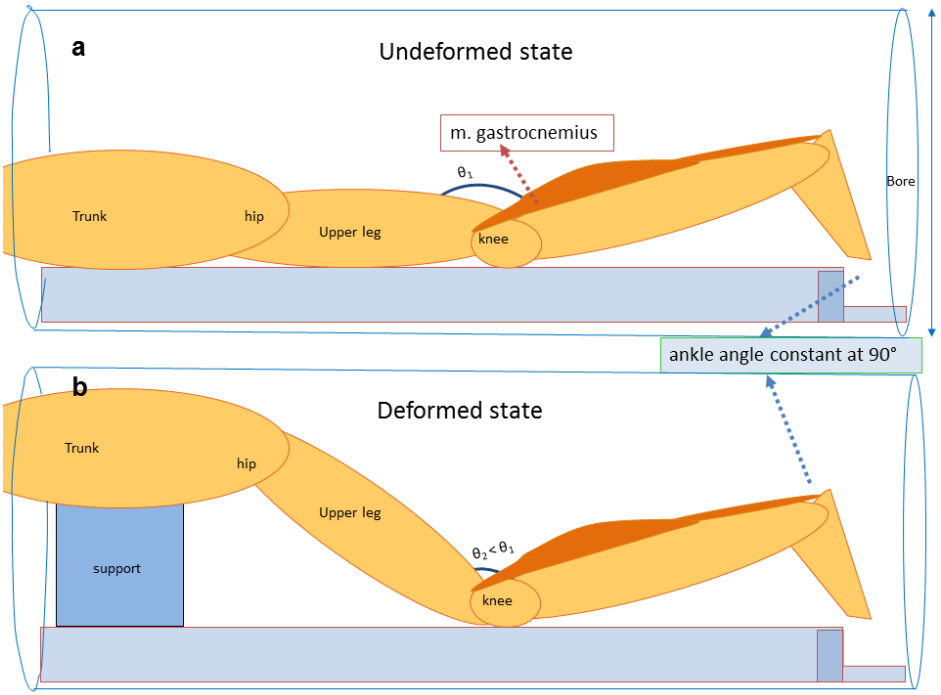

Figure 3.2 The subject is placed in prone position within the bore of the machine. An MRI compatible ankle-foot orthosis (*triangle*) is applied to fix ankle joint angle at 90°. A small space between posterior side or the lower leg and ankle-foot orthosis and also between anterior side of the lower leg and MR table is allowed to avoid exertion of other external forces. a) Condition arbitrarily defined as the undeformed state, with knee joint angle at ≈ 173°. b) Condition arbitrarily defined as the deformed state, with knee joint angle at ≈ 150°. This condition was attained by placing a support (*rectangle*) under the trunk which changed hip and knee joint angles, but left the position of the lower leg unchanged

After acquiring sets of 3D high resolution MR images in the undeformed state, the hip and knee joints were brought in flexion by repositioning the upper body: by a support of the chest using MR compatible material: the trunk was elevated until reaching the spatial limits of the MRI machine bore (diameter = 60 cm). In this

deformed state, the knee angle equaled 150 ± 6°. Subsequently, a second MR image set was collected. Imaging each set took 10 min.

3.2.2.3 Image Acquisition. 3D Turbo Flash based MR coronal image sets were collected using a 3T Siemens Trio scanner with 6-channel cardiac array coil (matrix size = 320 x 320 x 144, voxel size = 0.8 x 0.8 x 0.8 mm, TR = 2,000 ms, TE = 3.94 ms, no fat suppression, flip angle = 12°, band-width = 130 Hz per pixel). The region between the most proximal part of the head of the fibula and the most proximal location of the transverse crural ligament was imaged.

3.2.2.4 Calculation of Strain Fields. In order to align images of the deformed and undeformed states as well as possible, Demons algorithm [41] an intensity based non-rigid non-parametric image analysis technique, was applied to the MR image sets. Demons algorithm has been improved by several authors (a) to prevent instabilities for small image gradient values by additional constants [84], (b) to extend the algorithm using optimizers (i.e. gradient descent [84]) and limited use of memory [85], (c) to adapt for large deformations by multiresolution approach and (d) to accelerate by extending the equation using also the image gradients at the deformed state [86]. Note that, in our present study a version including these improvements of Demons algorithm was used.

After alignment of images, information on real deformation is contained in minimized image differences. Simultaneously with alignment process, the algorithm recalculates the exact cubic shape made up of four original voxels from the undeformed state into a deformed shape of approximately constant volume, again by an iterative process, while still trying to fit undeformed and deformed states. The volume elements of the deformed shapes corresponding to the original undeformed elements are assigned using three criteria: (1) the arrays of voxel gray scale values, (2) their array of grey scale differences (i.e. difference images), and (3) their grey scale gradients within the images. During each iteration performed, the displacement fields are smoothed by a

Gaussian kernel for regularization of global motion.

To calculate the strain tensor, the deformation gradient matrix, F was calculated first by using displacement gradient tensor (∇u) in material coordinates:

$$F = \nabla u + I \tag{3.2}$$

Green-Lagrange strain tensor, E was calculated as:

$$E = \frac{1}{2}\left[F^T F - I\right] \tag{3.3}$$

This tensor is then rotated, to remove shear effects, and calculate principle strains. The first and third principle strains were used separately in the analyses, since they represent local lengthening and shortening, respectively.

3.2.2.5 Estimation of Errors Introduced by Applying Demons Algorithm.

Image sets for each subject of the undeformed state were transformed by a "rigid body motion". This means that no real deformation was introduced. The rigid body motion imposed on the data consisted of (1) a 10° rotation within the cross-sectional plane corresponding to an endorotation of knee that may be expected as the knee flexed [87] and any global movement that may occur when changing the knee angle as described. (2) A 3° rotation in the coronal plane, (3) a 3° rotation in the sagittal plane and (4) a 4 mm translation in the axial direction. Since in reality, the position of lower leg was kept constant, rotations in cross-sectional and sagittal planes and the translation in axial directions should be infinitesimal. The original and transformed image sets were then aligned and compared as described above and principle strains were calculated. Note that, since in reality, the position of lower leg was kept constant, rotations in cross-sectional and sagittal planes and the translation in axial directions should be infinitesimal. Therefore, the rigid body motion imposed representing a much larger scale motion than caused by moving the knee joint allows a fairly critical testing of

artifacts during strain calculations, since by definition such motion should cause no deformation. Therefore, deviation of calculated principle strains from zero after rigid body image rotation is used as estimates of errors in strain calculations.

3.2.2.6 Further Treatment of Data. In order to assess tissue effects of changing knee angle, a slice group consisting of 30 consecutive cross-sectional slices was selected manually for each subject (Fig. 3.2a): the most proximal slice of the group was located at the upper third of the length of imaged portion of the lower leg in a longitudinal image (a level corresponding approximately to the mid-belly of m. gastrocnemius).

For each slice analyzed, anatomical regions representing muscles or compartments (i.e. muscle groups) were distinguished manually by outlining their boundaries. Doing so, m. gastrocnemius, m. soleus, deep flexor muscles, were marked (Fig. 3.2b).

Effects of changing the knee angle on deformations within passive lower leg muscles were assessed per marked area: Note that due to the fixed ankle angle, the muscle tendon complexes of lower leg muscles not crossing the knee (all except m. gastrocnemius, i.e. m. soleus, deep flexors, peroneal and anterior crural muscles) remain isometric. For each anatomical region separately, mean $\pm$ SE of principle strains were calculated occurring due to (1) the knee angle change and (2) errors introduced by the algorithm.

3.2.2.7 Statistics. For each anatomical region separately, sample of principle strains and error strains were compared. Since the calculated principle strains and error strains are, by definition, not distributed normally, nonparametric Wilcoxon rank sum tests ($p<0.05$) were used to test for significant differences.

If principle strains were significantly bigger than error strains, we concluded that the effect should be assigned to altered body position (most important: knee joint angle).

3.3 Results

3.3.1 Global Strain in Gastrocnemius Muscle as a Consequence of Knee Movement

As human gastrocnemius muscle functions as a knee flexor, changes in knee joint angle will lead to changes of muscle-tendon complex length (lengthening for knee extension, shortening for knee flexion), the size of which is determined by actual moment arm length and actual knee movement imposed. Figure 3.3 shows results measured in human cadavers for a sizable range in knee joint angles.

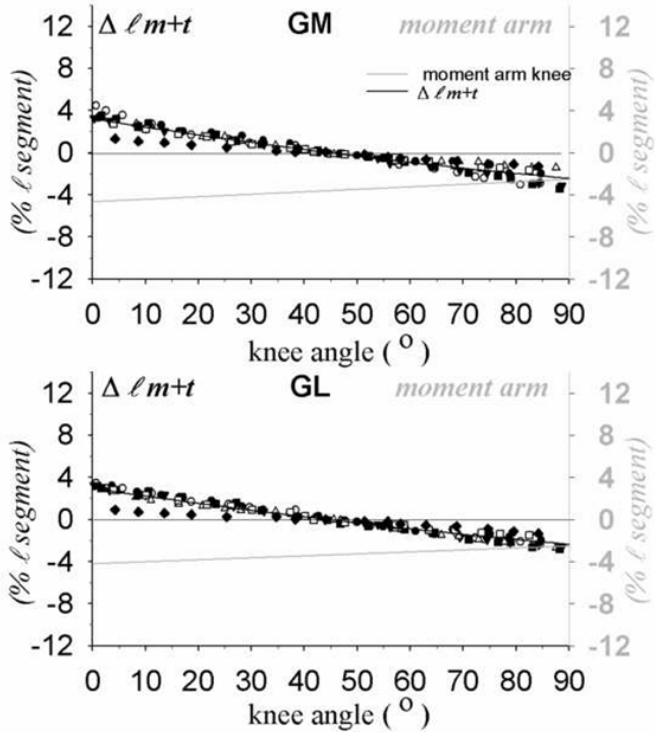

Figure 3.3 Gastrocnemius muscle-tendon complex length changes as a function of knee angle. *Upper panel* m. gastrocnemius caput medialis (GM). *Lower panel* m. gastrocnemius caput lateralis (GL). Length change (Δl_{m+t}, use left Y-axis) is plotted as individual (n = 7) data and normalized for tibia length (l segment) A polynomial is fitted to the data (*drawn black line*, use left Y-axis). The *gray lines* (use right Y-axis) describe the relation of moment arm and knee joint angle, as calculated from the fitted knee angle-length change curve by differentiation. 180 ° represents a fully extended knee.

To facilitate further use of the fitted curves, the values their coefficients selected in the fitting process are shown in Table 3.1. Polynomial ($\Delta l_{m+t} = A_3\phi^3 + A_2\phi^2 + A_1\phi + A_0$) is fitted to knee angle-gastrocnemius length change data (shown in Fig. 3.3), where

ϕ represents knee joint angle, defined according to the conventions described in the methods. Note that knee angle length change curves were statistically best explained by second order polynomials (A3 being equal to zero), explaining the linear nature of the knee angle moment curves (as obtained by differentiation).

Table 3.1
Polynomial coefficients obtained by fitting pooled joint angle - normalized length change data sets for each muscle head

Joint	Muscle head	A_3	A_2	A_1	A_0
knee	GM	0	0.000206	-0.081560	3.240837
knee	GL	0	0.000163	-0.073618	2.951952

The data show that gastrocnemius moment arms at the knee are not constant, but increase with knee flexion. Differences between medial and lateral heads of the gastrocnemius in both length change moment arm are quite small. For the much smaller range of knee joint angles to be considered below in human subjects using MRI analysis the values of length change normalized for tibia length amounted to only approximately 1.5% of tibia length. As gastrocnemius muscle-tendon complex is somewhat longer than tibia length, expected imposed global strain due to length changes of the muscle tendon complex will be somewhat less than 1.5%.

Within the context of this experiment (constant ankle joint angle, i.e. a globally isometric soleus muscle), length changes of gastrocnemius muscle with changing knee angles are also indicative for the relative movements of soleus and gastrocnemius muscles. This is important as the relative movement between muscles will co-determine stiffness of the connections between them.

3.3.2 MRI Analysis of Local Muscle Strain

3.3.2.1 Accuracy in Displacement and Local Strain Calculations. For the muscular regions studied, error strains calculated are small (mean$<$1.5%). Therefore, it is concluded that the image handling methods applied successfully aligns images and

does not introduce major errors or artifacts in the calculation of principle strains for gastrocnemius and soleus muscles.

3.3.2.2 Effects of Knee Angle Change on *in vivo* Passive Muscular Strains.

Figure 3.4 shows a typical example of a comparison of deformation of a regular grid mapped on a sample's most proximal slice in the undeformed state (Fig. 3.3b) and the deformed grid calculated for the deformed state (Fig. 3.3c). Note that, for clarity, this example (Fig. 3.3b) presents 2D results, while a 3D analysis was performed. Note also that grid deformations are encountered in subcutaneous fat tissues and skin, as well as in muscle tissue.

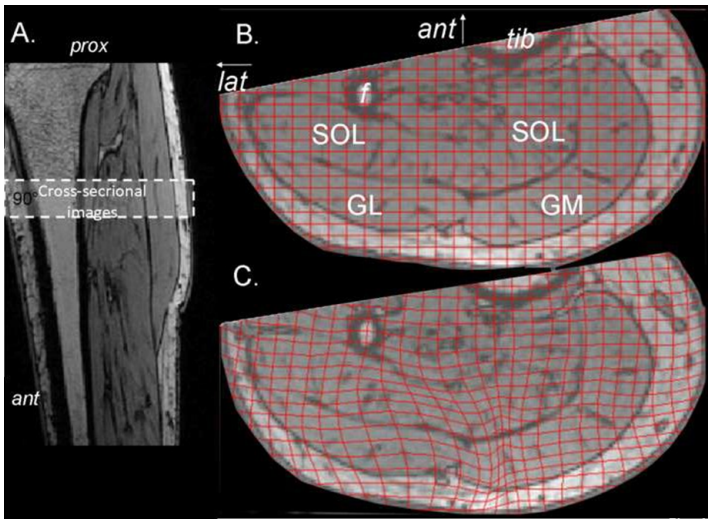

Figure 3.4 Typical example of MRI images with superimposed undeformed and deformed grids. a) Longitudinal image of the lower leg, indicating the location of the cross-sectional images taken. b) Cross-sectional MRI image of the lower leg (most proximal image of the stack) in the undeformed state, with the undeformed grid imposed and indications of anatomical structures to be seen. Knee joint angle $\approx 173°$ Ankle joint angle = 90°. c) Cross-sectional MRI image of the lower leg (most proximal image of the stack) in the deformed state, with the deformed grid imposed (Knee joint angle $\approx 150°$. Ankle joint angle = $90°$). *"Ant"* indicates anterior side or direction (*arrow*) and *"lat"* indicates lateral side and direction (arrow *"Tib"* and *"f"* indicate tibia and fibula, respectively, and the relevant muscles are indicated as follows: GL and GM represent m. gastrocnemius caput lateralis and medialis, respectively, and SOL indicates m. soleus.

Within m. gastrocnemius. Mean principle strains within m. gastrocnemius are significantly higher than error strains for this muscle (Fig. 3.5). Being a knee flexor for m. gastrocnemius, knee extension corresponds to overall lengthening strain and knee flexion to overall shortening strain. Mean local shortening in m. gastrocnemius

muscle remained limited to values $\approx 10\%$), but note that similar values were attained for local lengthening. This indicates the presence of considerable strain distributions within this muscle. In addition, note that such peak values are much bigger than the global strain imposed on the whole muscle-tendon complex.

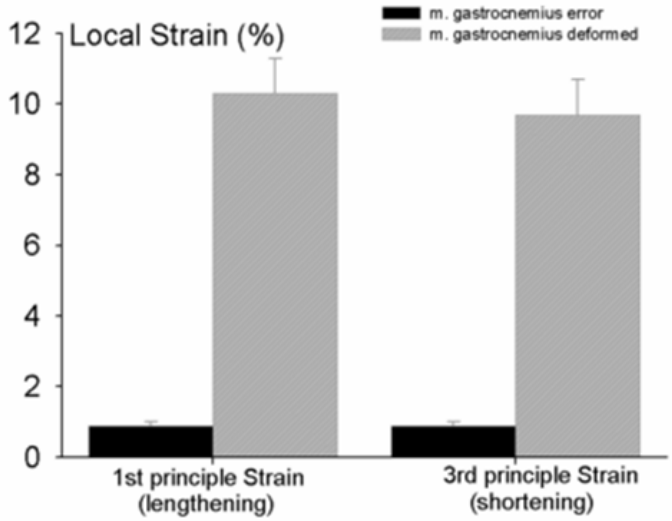

Figure 3.5 Mean principle local strains within m. gastrocnemius. The error strains (*dark bars*) were calculated after large scale solid body rotation of the images, i.e. involving no actual deformation of tissues. Principle strains calculated (*hatched bars*) by comparing images taken at knee joint angles equal to $173^\circ \pm 3^\circ$ and $150^\circ \pm 6^\circ$, respectively. Note that ankle joint angle remained at 90° while collecting both image sets. Mean values and SE are plotted.

Within m. soleus. It should be noted that if soleus and gastrocnemius muscle would be fully independent mechanically, no local strains should be encountered within soleus muscle, since this muscle-tendon complex does not cross the knee joint and as consequence, no global strains are imposed on this muscle-tendon complex. In contrast to such expectation, mean principle strains for m. soleus are also significantly different from error strain values and attain a considerable magnitude (between 8.5 and 9.4% for shortening and lengthening, respectively, Fig. 3.6).

Therefore, we conclude that considerable mechanical interaction between these synergistic plantar flexor muscles accompanies altered knee joint angles. Such local strains are very hard to explain, unless intimate connections between these synergistic muscles are assumed that transmit force between gastrocnemius having been exposed to length changes, with soleus muscle remaining at an overall intermediate muscle-tendon

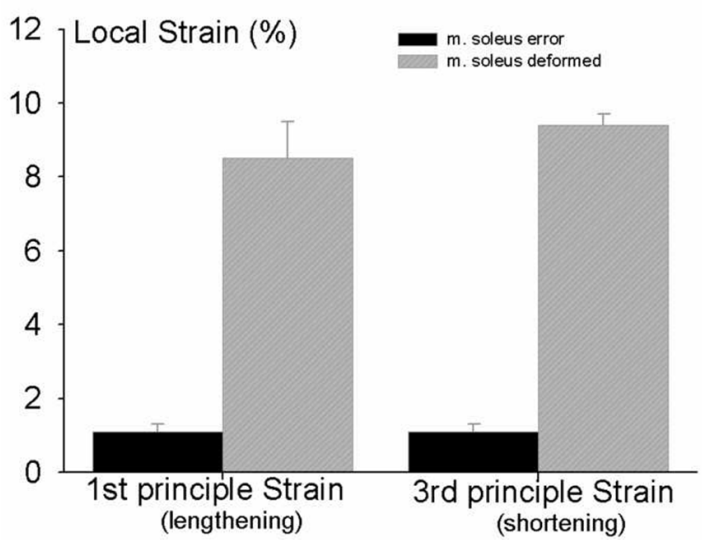

Figure 3.6 Principle strains within m. soleus. The error strains (*dark bars*) were calculated after large scale solid body rotation of the images, i.e. involving no actual deformation of tissues. The strains calculated (*hatched bars*) by comparing images taken at knee joint angles equal to $173° \pm 3°$ and $150° \pm 6°$, respectively. Note that ankle joint angle remained at $90°$ while collecting both images.

complex length (Fig. 3.7).

It also concluded that the pattern of strains is not a simple one: First, considerable variation between individuals was encountered. Some of this was also seen for global strain measurements for m. gastrocnemius (Fig. 3.3) However, variation in local strains is much higher (Fig. 3.5). It should, however, be remembered that these values contain individual sources of variation, as well as variation per location within muscles. Second, at different locations within soleus muscle local lengthening will occur simultaneously with local shortening at other locations.

3.4 Discussion

Major results of the present work are the findings that (1) local strains within the muscle are very much higher that the global strains imposed on it (2) such local strains are not limited to the specific muscle that is exposed to length changes, but also occur within synergistic muscle kept at constant muscle-tendon complex length (global isometric condition).

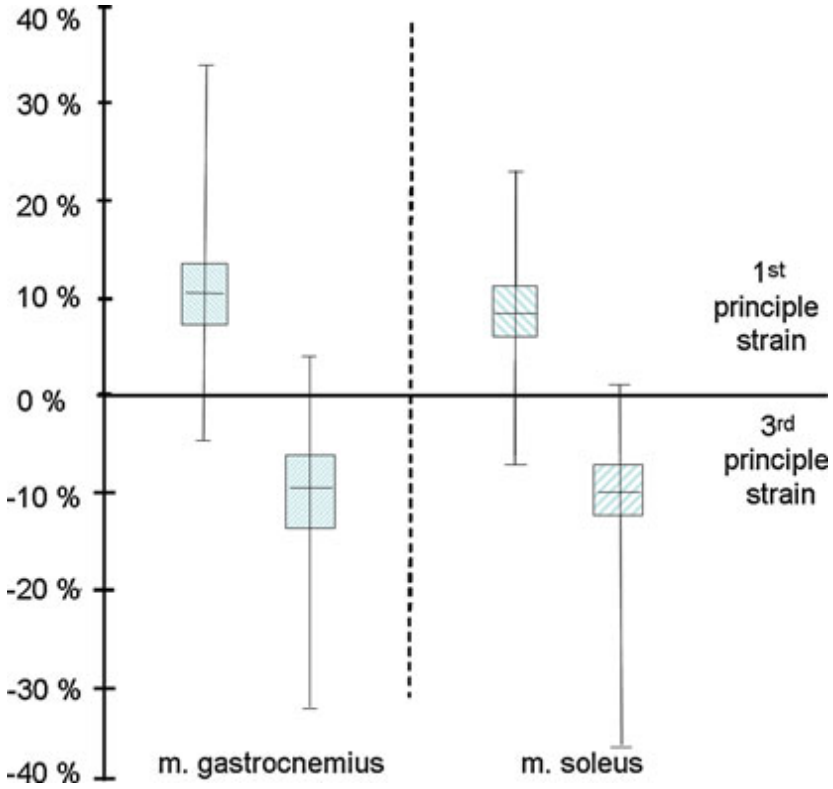

Figure 3.7 Effect of altered knee angle: local shortening and lengthening effects. The *horizontal line inside the box* represents the median strain value; the upper and lower edges of a box itself represent upper and lower quartiles (i.e., the 75th and 25th percentiles), respectively, and lines extending from the median represent range of values of the principle strain plotted. Data are analyzed across all subjects (n = 5).

This means that, also *in vivo*, synergistic muscle are not mechanically independent. This idea is compatible with many results of animal experiments (for reviews see [73, 74]), on the basis of which the ideas of epimuscular myofascial force transmission were developed over the last decade.

It should be noted that based on such animal experiments myofascial force transmission between antagonistic muscles is also predicted. Presently, further analysis of the image data set used in this study is progress to test that hypothesis. A preliminary analysis indicates that such a hypothesis is likely to be accepted [88].

The essence of the concept of myofascial force transmission is that force transmission of muscle is not limited to that between a specific muscle and its own tendon(s), but that simultaneously a fraction of the force generated (depending on con-

ditions, sometimes quite considerable) is transmitted "'"sideways" between muscles, either directly between adjacent muscle bellies (intermuscular transmission) via the shared epimysium between the muscles, or via extramuscular connective tissues linking synergistic muscles and between muscle and bone (extramuscular force transmission). In fact, such concepts involve the notion of continuity of tissues within a limb segment that certainly has been considered in history (for a short historical review see [74]). In addition to that it seems that one of the first to fully ascribe this notion of continuity of connective tissues was the Dutch anatomist Andreas Bonn, who in his doctoral dissertation [89] reproduced in [90], laid a solid base for such ideas of continuity of connective tissues, even though he did not focus specifically on muscular connections. Despite the early work, until recently the connective tissue matrix was either ignored or considered a benign scaffold keeping things together. Therefore, further going functional consequences were not considered. The resent work indicates that the concept of tissue continuity needs to be revived as it also leads to important functional effects, such as muscular interaction by myofascial force transmission, also occurring *in vivo* in human subjects.

3.4.1 The Concept of Continuity of Tissues Within Limbs

The anatomical substrate of the different types of myofascial force transmission can be described as follows: the sarcomeres within muscle fibers are connected to the intracellular cytoskeleton that is connected via subsarcolemmal actin filaments (differing from the sarcomeric ones) to trans-sarcolemmal molecules (integrins and/or sarcoglycans) that is connected to the endomysium, a connective tissue tube within each muscle fiber is located. The collection of endomysial tubes of a muscle fascicle form a continuous system that is surrounded by another connective tissue tube, the (primary) perimysium. Groups of small fascicles or bundles of muscle fibers are surrounded as well by epimysial tubes (secondary ones). In turn, the collection of perimysia constitutes a continuous system, sometimes called a stroma that is delimited by the epimysium. *in vivo* muscle is working within its natural context of connective tissues. For synergistic muscles, walls of epimysial tubes are shared, except for places where neurovascular

tracts pass between muscles. However, neurovascular tracts also connect muscles to each other as branches containing vessels and nerves pass into the muscle and are continuous with the tertiary perimysium that does not fully surrounds fascicles or groups of small fascicles. The neurovascular tracts are attached also to the periost surrounding the bones and to other nonmuscular elements of the connective tissues system, such as the interosseal membrane, the intermuscular septum which themselves are continuous with the general fascia of the limb. This describes the full continuity of the system. However, if myofascial force transmission will occur to an appreciable extent using a specific pathway, is not so much determined by the fact that it is connected, but rather the actual stiffness of the connections, which depends on the actual circumstances such muscle length (i.e. joint angle) and relative positions of muscles with respect to each other and to the non-muscular elements described above. Our present results are indicative that at least some of the pathways mentioned are stiff enough to create substantial local length changes within soleus muscle. The specific identification of such pathways should be pursued in future work.

3.4.2 Myofascial Force Transmission With Imposed Joint Position And Joint Movement

It should be noted that all previous physiological and surgical experiments proving epimuscular myofascial force transmission involved length changes imposed directly on the muscle (by moving the proximal or distal tendon) without simultaneous movement of the joint. It is very easy to show that the extramuscular neurovascular tracts (i.e. the collagen reinforcement of blood and lymph vessels and nerves) is exposed to considerable changes of length, position and tension (for an informal way of showing that see [73]). This means that *in vivo* myofascial force transmission could potentially quite different in effects or size if such joint movement were present as well.

Recently, Maas and Sandercock acted on such a potential limitation of previous work and performed an elegant experiment in the cat. Their experiment [91] involved features that resemble those also of our present study: Ankle angle was kept

constant, while the knee was moved and force exerted by soleus muscle was measured and net ankle joint moment was calculated on the basis of externally measured forces at the foot. With soleus muscle in its natural position, they did not find any sign of intermuscular interaction. However, if soleus was moved from its original length and position (corresponding to the imposed constant ankle angle), myofascial effects were apparent immediately. Based on these results, they generalized their findings by concluding that mechanical interaction between muscles does not occur under physiological circumstances *in vivo*. In reaction, Herbert and co-workers pointed out Maas and Sandercocks experiment was not really an *in vivo* experiment [92] indicating the need for such real *in vivo* work. It is clear that given our present results Maas and Sandercocks generalized conclusion is not tenable.

This is supported also by recent work [93] applying *in vivo* ultrasound imaging techniques on human triceps surae. Selective stimulation of medial gastrocnemius muscle, as well as passive knee extension yielded displacement of both medial gastrocnemius and soleus muscles.

Reasons for such contrasting results are not immediately apparent. It could be related to differences of species or to differences in dynamics: In the present experiment, we had to compare two static situations (due to long imaging times), while Maas and Sandercock imposed joint movement dynamically. Therefore, there is a need for direct experimental comparison of effects such static and dynamic conditions.

3.4.3 Further Limitations of Our Present Experiment

In addition to some limitations discussed above, we need to consider some others.

3.4.3.1 Strain in Muscle Fiber Direction. It should be kept in mind that the strains reported in the present work are local muscle strains, but expressed in terms of an outside coordinate system.

Particularly in human gastrocnemius and soleus muscles this is a real limitation, since both are very pennate (as is apparent also from the huge difference between fascicle length and muscle length). In both muscles, they have to span only the oblique distance between proximal and distal aponeurosis which is in the order of 5 and 3 cm, respectively. Gastrocnemius muscle has a unipennate architecture and soleus muscle a bipennate structure indicative of quite different muscle fiber directions at opposite sides of the distal aponeurosis. Myofascial force transmission takes place at the interface between the ends of the muscle fibers and extracellular collagen fibers inserted into the myotendinous junction that are collected to form the collagen bundles that run predominately in the longitudinal direction of the aponeurosis.

The physiologically important variable is of course local strain in the direction of muscle fibers, representing length changes of sarcomeres. In previous finite element modeling studies, due to epimuscular myofascial force transmission major strain heterogeneity in the local muscle fiber direction is a common feature [15, 18, 20, 94]. Our present results suggest that sizable strains in the local muscle fiber direction (but somewhat smaller than the peak strains reported presently) are expected also in human subjects *in vivo*. However, this needs to be confirmed. Fortunately, MRI imaging is also capable to provide techniques to estimate fiber directions locally within the muscle.

On the other hand, the present findings show local deformations involving lengthening and shortening occurring simultaneously at different locations within the same muscle and can differ from in size as well as direction from the global strains imposed on the muscle. Model studies also indicate that (e.g., for a muscle at high length), a presence within the same muscle fiber of not only lengthened sarcomeres, but also considerably shortened ones are to be expected (e.g. [88]). If sarcomere length heterogeneity to such a major extent occurs also *in vivo*, needs to be tested. To do that, work is in progress applying additional MRI methods to determine the direction of muscle fibers locally within the collected images and convert present strains results to local muscle fiber strain in fiber and cross-fiber directions.

3.4.3.2 Muscle Activity. Since it is difficult to combine electromyography with the high magnetic field within the bore of the MRI machine, we have had no rigid control of activity of target muscles. Measurements performed outside of the MRI machine indicate that the target muscles may not have been fully passive, but activities are expected to have relatively low (<0.5% MVC). Temporal variation of muscle activity is unlikely to have contributed to the results because of long imaging times. In addition, differences in muscle activity could not cause simultaneous occurring differences of first principle strain (indicative of lengthening) and third principle strains (indicative of shortening).

3.4.4 Consideration of Some Potential Clinical Implications of the Concept of Myofascial Force Transmission

The concepts of epimuscular myofascial force transmission should have major effects on our thinking of the physiology and pathology of muscular function, within such altered views also adaptation of clinical concepts are expected and are only just beginning to appear.

In surgery, it is important to realize that dissection necessary to gain entrance to a limb will lead to a generally higher compliance of the continuous fascial or connective tissues system, unless an extremely small window within the general fascia is used to gain access. This means that in most surgery, the properties of this system and thus also of muscles are changed before the surgeon may feel that the actual intervention has really started. It is likely that preventing or limiting such altered properties constitutes a considerable advantage of minimal invasive surgery.

Regarding *spastic paresis*, where relative positions of muscles under spastic neural control are altered with respect to non-spastic muscle, as well as nonmuscular structures because spastic muscle will have a tendency to be shorter than non-spastic muscles, the knowledge of epimuscular myofascial force transmission may provide a new way of thinking in trying to explain the nature of the relatively fixed preferential

positions of joints crossed (sometimes referred to as contracture). Recently, we have presented a hypothesis [73] involving interaction between antagonistic muscles due to epimuscular myofascial force transmission between non-spastic and spastic muscle. It is clear that that stiffness of elements of epi- and intramuscular myofascial links needs to be considered. Presently, our group has, evidence [95], article in preparation] that the tertiary epimysium is thickened (and presumably stiffer) in human spastic flexor carpi ulnaris muscle (FCU). This fits with earlier findings of our group [78] that after partial dissection (for the purpose of subsequent tendon transfer to an extensor insertion) the length force characteristics of FCU in human patients measured during the operation did not give any indication that could explain the preferential wrist position of these patients. This indicates that not the muscle characteristics per se are affected as secondary effects of the spastic neural control, but rather the mechanical interaction with its environment leading to different functionalities. Particularly for spastic human triceps muscle, one may expect such effects at much higher level due to its relatively high moment arm with respect to and talo-crural and subtalar joints and their effects on relative position of this muscle group.

Based on the hypothesis described, rather than performing tendon transfers, the surgeon may consider looking for ways to interrupt the mechanical interaction between antagonistic muscles. However, this is not expected to be easy, since it seems not likely that the mechanical role of the neurovascular tract can be interfered with, and if one could, to make this effect permanent (prevent regeneration of intermuscular mechanical linkages).

Our knowledge of myofascial force transmission make it intuitive why genetic deficiencies of proteins that are a part of the trans-sarcolemmal chain of molecules leads to serious disease (*muscular dystrophies*). However, much more work is needed to enhance our understanding of the mechanics of these phenomena. We have some animal experimental work in progress on this subject.

Another example is recent work on tenascin-X deficient serving as a model for *Ehlers-Danlos disease* and wild type mice [96]. For this disease, clinically, changes

in muscle function are not considered often, since standard histological tests applied do not indicate muscle pathology. Nevertheless, the interaction of muscles with much more compliant connective tissues within limb segments in such patients are likely to contribute to altered muscle characteristics with functional consequences. If coordination of muscular activity by the central nervous system is not arranged to deal with this altered condition optimally, it could well explain patients' complaint regarding fatigue.

It is clear that more *in vivo* MRI analysis in patients with one of several diseases is indicated. Methods similar to the ones described here may help to do that.

4. MRI ASSESSMENT OF MECHANICAL INTERACTIONS BETWEEN HUMAN LOWER LEG MUSCLES *in vivo*

4.1 Introduction

It is widely accepted that myotendinous junctions are main sites for transmission onto the bone of the forces generated by sarcomeres within muscle fibers [5]. However, in addition to myotendinous junctions, muscle fibers and intramuscular connective tissue stroma are connected along the full periphery of the muscle fibers: adjacent myofibrils are connected by the intracellular cytoskeleton and trans-sarcolemmal molecules connect the cytoskeleton to laminin which is connected to the basal lamina (for a review see [1]). The basal lamina in turn is connected to the endomysium. These structures have been shown to transmit muscle force [97, 98, 99, 100]: *intramuscular myofascial force transmission*. Within the context of its intact connective tissue surroundings (*in vivo* condition) collagenous linkages between epimysia of adjacent muscles provide direct, and structures such as collagen reinforced neurovascular tracts provide indirect *intermuscular connections*. In addition, compartmental boundaries (e.g. intermuscular septa, interosseal membranes, periost and compartmental fascia) are connected to neurovascular tracts. Such *extramuscular connections* bind muscular and nonmuscular tissues at several locations, in addition to the connections of tendons at origins or insertions.

Results of many animal experiments performed by our research groups (for a review see [74]) show that *epimuscular myofascial force transmission* (EMFT) occurring via this integral system of connections leads to characteristic effects on muscular mechanics including major proximo-distal force differences (e.g., [12], [20]) and varying muscle length-force characteristics as a function of mechanical conditions (e.g., [15],[17]). Moreover, using finite element modeling, EMFT has been shown to cause highly non-uniform muscle tissue deformation (e.g., [20],[17]).

Based on such findings, we hypothesized that global length changes imposed externally on the target muscle-tendon complex by joint movement will cause sizable and heterogeneous local strains within that muscle, as well as within muscles of the human lower leg that remain isometric. The goal of the present study was to develop a method that allows for performing large deformation analyses in human muscle tissue, *in vivo* and to test this hypothesis. In order to do that, magnetic resonance imaging (MRI) techniques were used.

4.2 Methods

4.2.1 Experimental Procedures

4.2.1.1 Subjects. Experimental procedures were in strict agreement with guidelines and regulations concerning human welfare and experimentation set forth by Turkish law, and approved by a Committee on Ethics of Human Experimentation at Istanbul University, Istanbul School of Medicine, Istanbul. Five healthy subjects (mean ± SD: age = 27 ± 3 years, height = 175 ± 7 cm and body mass = 73 ± 8 kg) volunteered for this study. In order to minimize anthropometric differences between subjects (Table 4.1), only males were recruited. After a full explanation of the purpose and methodology of the experiments, the subjects provided an informed consent.

Table 4.1
Anthropometric data

Subject	**Age**	**Height (cm)**	**Mass (kg)**	**Upper leg length (cm)**	**Lower leg length (cm)**
A	29	178	85	41	31
B	31	188	73	46	41
C	23	173	72	41	39
D	25	170	70	45	40
E	30	172	78	42	38

4.2.1.2 Experimental Protocol. Each subject was positioned prone within the MRI scanner. The left leg was brought to a reference position before the patient table (a motorized and computer-controlled slide) was moved into the MRI bore: (I) the ankle angle was fixed at 90° (Fig. 4.1) by using an MRI compatible ankle-foot orthosis (brace on the lower leg and the foot allowing fixation of the ankle angle). (II) To keep orientation of the lower leg constant, the position of the knee cap and the tip of the ankle-foot orthosis were marked on the patient table. (III) The knee angle in this position (*undeformed state*) was (mean ± SD) 173° ± 3°. Based on e.g., [101], knee joint angle was measured using a universal goniometer with its center positioned over the lateral epicondyle of the femur and its arms aligned with the femur and tibia. After moving the patient table into the bore, sets of 3D high-resolution MR images were acquired in the undeformed state. Subsequently, the patient table was moved out of the bore. The hip and knee joints were brought in flexion by repositioning the upper body using a MRI compatible chest support until the trunk approached the bore wall (diameter 60 cm). In this *deformed state*, the knee angle equaled 150° ± 6°. Care was taken to maintain the positions of the kneecap and the tip of the ankle-foot orthosis. Subsequently, the patient table was moved back into the bore automatically ensuring that it attains the identical position as during previous image acquisition. Subjects were asked to remain completely relaxed throughout the experiment.

4.2.1.3 Image Acquisition. 3D localizer imaging was performed to plan the subsequent imaging sequences. 3D turbo fast low-angle shot [Turbo Flash] based coronal MR image sets were collected using 3T MR scanner (Magnetom Trio; Siemens, Erlangen, Germany) with 6-channel surface cardiac array coil. The following parameters were used in the Flash sequence: TR = 2000 ms, TE = 3.94 ms, TI = 1100 ms, no fat suppression, flip angle = 12°, bandwidth = 130 Hz/pixel, number of averages = 1, field of view = 256x256 mm, slice thickness = 0.8 mm (distance factor = 50 %), image matrix size = 320x320x144, voxel size = 0.8x0.8x0.8 mm. Choices of high bandwidth (41600 Hz) and frequency encoding in proximo-distal direction [102] allowed minimizing potential chemical shift artifacts. Imaging time equaled 6 minutes and 50 seconds.

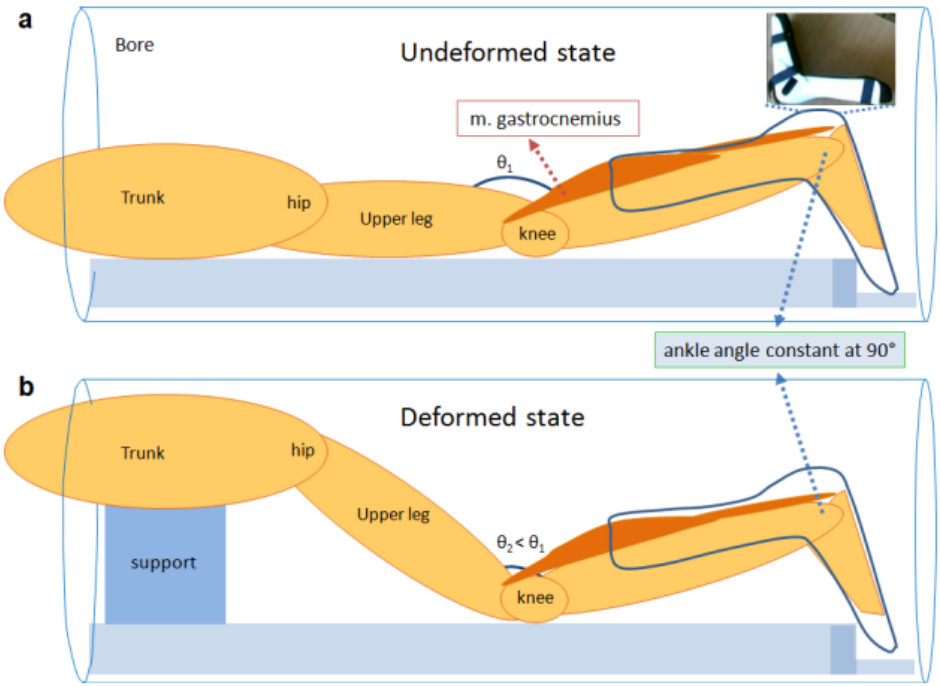

Figure 4.1 Schematic of the leg and trunk within the MRI instrument. (a) Undeformed state. The body is prone on a table (solid line) that is can be moved in and out of the bore of the MRI machine. MRI compatible ankle-foot orthosis (see inset for a picture) was used to fix the ankle angle at 90 °, in such a way to leave a small space between posterior side of the lower leg and the ankle-foot orthosis and also between anterior side of the lower leg and MR patient table to avoid exertion of other external forces. The ankle-foot orthosis was secured onto the patient table using support material. The tips of the toes were not allowed to contact the bore of the MRI machine in order to prevent the foot from being loaded mechanically. (b) The deformed state. The trunk of the subject is now supported and brought as close as possible to the bore wall. This creates movement in hip as well as knee joints, but leaves the lower leg in a similar position. In any case the ankle angle is unchanged.

4.2.1.4 EMG Assessment of Subject Relaxed State.

In order to confirm the subject's relaxed state during the experiments, an EMG test was performed (n = 1). Pre-amplified bi-polar surface EMG (Delsys, Trigno Wireless, Boston, MA, USA) was used. Electrodes were located over mid muscle belly of m. gastrocnemius and m. tibialis anterior. This showed that in the final isometric states, EMG activity was very low for both muscles: root mean square values of full wave rectified low pass filtered EMG data normalized for subject's EMG during maximal voluntary contraction (MVC) was less than 0.5 % of the respective MVC value.

4.2.2 Calculation of *in vivo* Strains and Volume Changes

A slice group consisting of 30 consecutive cross-sectional slices was selected manually for each subject (Fig. 4.2a): the most proximal slice location was at the proximal third of the length of imaged portion of the lower leg (corresponding to mid-m. gastrocnemius belly).

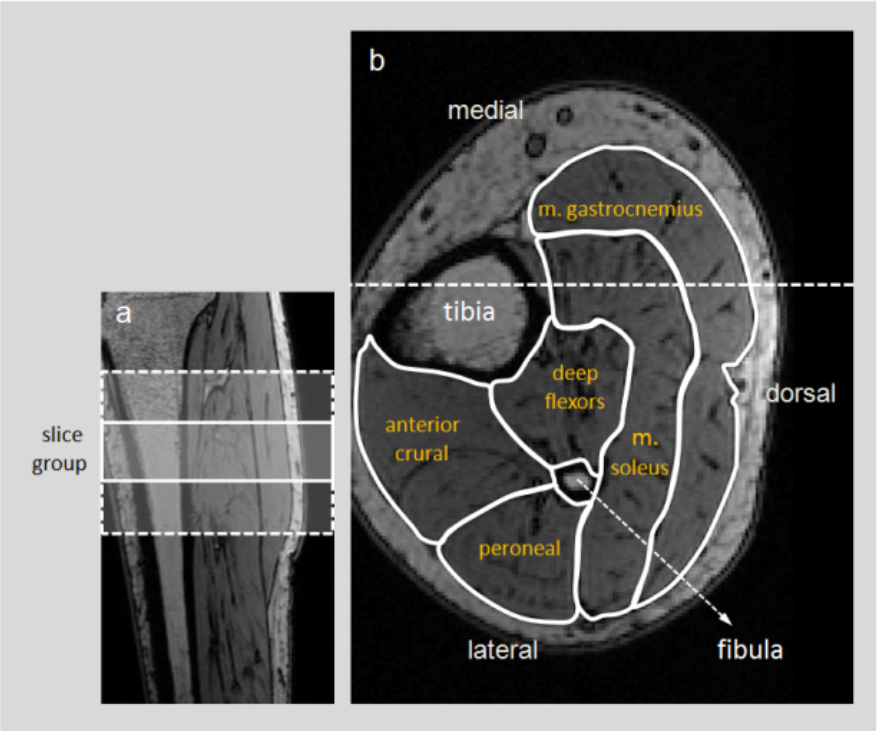

Figure 4.2 Examples of MR images of the lower leg. (a) Longitudinal image of the lower leg representing a sagittal slice illustrating the locations of the group of cross-sectional slices (white solid rectangle) to be analyzed for strains. For all subjects, the most proximal cross-sectional slice of the slice group was located at the upper third of the imaged portion of the lower leg, a level corresponding to the mid-belly of m. gastrocnemius. The white dashed rectangle encloses the group of cross-sectional slices on which the method was tested by imposing known deformations on m. gastrocnemius. Strains induced as a result of this test were analyzed only for the group of cross-sectional slices enclosed by white solid rectangle for which deformations were maximal. (b) An example of a cross-sectional image of the slice group with anatomical identification of muscles or muscle groups and bones (tibia and fibula). Five anatomical regions of interest were distinguished: m. gastrocnemius, m. soleus, deep flexor muscles, peroneal muscles and anterior crural muscles. The dashed horizontal line indicates the location of sagittal image shown in (a).

Within each slice analyzed, five anatomical regions representing m. gastrocnemius, m. soleus, deep flexor muscles, peroneal muscles and anterior crural muscles were distinguished manually by outlining their boundaries (Fig. 4.2b).

Deformations caused by knee joint angle changes i.e., *in vivo strains* and *volume changes* were calculated. In order to do that, MR images acquired in the deformed and undeformed states were aligned. Demons algorithm [41] i.e., a non-rigid and non-parametric image analysis technique was applied. Utilizing arrays of voxel grayscale values, this algorithm relies on (i) *gradients of images* and (ii) *differences between images* i.e., differences between voxel grayscale values of consecutive voxels within each image and corresponding voxels in deformed and undeformed images, respectively. Image differences calculated iteratively are used to characterize displacement values for each voxel. During each iteration, updated displacement fields are smoothed by a Gaussian kernel for regularization of local displacements and global motion. Finally, after a successful alignment of images obtained by minimizing image differences, information on real deformation is available for each cubic shape comprised of four adjacent image voxels.

Using displacement fields obtained, deformation gradient matrix F, characterizing voxel deformation, was calculated by using displacement gradient (∇u) in material coordinates:

$$F = \nabla u + I \tag{4.1}$$

Green-Lagrange strain tensor E was calculated for each voxel in order to assess deformations within the lower leg muscles present after changing the knee and hip angles:

$$E = \frac{1}{2}\left[F^T F - I\right] \tag{4.2}$$

For each anatomical region separately, the principal strains, were calculated (means $\pm$ SE reported). First (E_1) and third (E_3) principal strains are considered to represent maximal tissue lengthening and shortening respectively. Second principal strains (E_2), characterizing relatively smaller length changes, were not included in the analysis.

In addition, heterogeneity of deformation was analyzed within anatomical regions distinguished. Note however, that further analyses involving more specific tissue locations and particular strain directions (e.g. muscle fiber direction) are left for future work.

For each voxel with undeformed and deformed volume represented by a^3 and $(a+E_1)(a+E_2)(a+E_3)$ respectively, volume changes (ΔV) were calculated as:

$$\Delta V = (a+E_1)(a+E_2)(a+E_3) - a^3 \tag{4.3}$$

4.2.3 Calculation of Artifacts

The validity of Demons algorithm in quantifying tissue deformations was tested vigorously by artificially transforming image sets.

4.2.3.1 Effects of Rigid Body Motion: Subject-Repositioning Artifacts. Image sets of the undeformed state were transformed by a "synthetic rigid body motion" imposed on the data for each subject: (i) a 10° rotation within the cross-sectional plane (corresponding to an endorotation of knee as the knee flexed [87]), (ii) a 3° rotation in the coronal plane, (iii) a 3° rotation in the sagittal plane and (iv) a 4 mm translation in the axial direction.

Subsequently, image sets of the undeformed state and the transformed image set were compared and *apparent strains* were calculated. Theoretically, rigid body motion, as imposed in this validation test, should not cause any strains. Therefore, any strains calculated accordingly represent strain errors (type A) and are referred to as *"subject-repositioning artifacts"*.

4.2.3.2 Effects of Artificial Deformation: Algorithm Artifacts. A slice group consisting of 100 consecutive cross-sectional slices (the middle slice corresponds to the

mid-m. gastrocnemius belly) in the undeformed state was selected manually. The tissues other than m. gastrocnemius were left undeformed. Deformation of m. gastrocnemius was imposed according to an artificially generated 3-D deformation field, so that the center points of voxels were displaced by prescribed amounts. In this configuration, line segments joining neighboring voxel center points comprise a parallelepiped. Compared to its cubic form in the undeformed state, this transformation involves length changes of the sides (i.e., normal strains) and disrupted orthogonality (i.e., shear strains). Subsequently, the new voxel grayscale values that characterize the transformed set of images were calculated using interpolation.

Known imposed displacements (for the slice subgroup also considered in the analysis of the effects of knee angle changes, mean $\pm$ SD = 3.02 $\pm$ 0.78 mm, peak displacement = 5.75 mm) were generated using Mersenne Twister uniform pseudo-random number generator [103] and were smoothed. Imposed displacements were comparable in size to displacements induced by experimentally imposed knee angle changes (mean $\pm$ SD = 3.02 $\pm$ 1.29 mm values, peak displacement = 6.26 mm). In vertical direction, they were bound to a gradual decrease from the middle slice on. This was governed by a sinusoidal function (spatial period equals the summed thicknesses of 200 slices). Consequently, imposed displacements were zero for the most proximal and distal slices selected, and the highest within the central part. The tests remained confined to the slice group selected.

By comparison of such undeformed and artificially deformed sets of images, two strain fields were calculated for (i) the known imposed displacements and (ii) the transformed set of images. Note that the former yields exact strains imposed, whereas the latter (involving application of Demons algorithm) yields approximated strains.

Subsequently, type B strain errors were calculated as local differences between these strains. The imposed artificial deformation field sets a benchmark for effects of tissue movement occurring during the experiment. Therefore, type B strain errors are referred to as *"algorithm artifacts"*.

4.2.4 Distinguishing Physiological Deformations from Artifacts

4.2.4.1 Rationale. Changes in knee angle will change the length of m. gastrocnemius. Therefore, substantial local deformations are expected within this muscle. In contrast, muscles not crossing the knee remain isometric. Therefore, true nonzero local strains within these muscles are to be considered as physiological effects of knee (and hip) angle changes. For all muscles, physiological strains should be distinguished from artifacts. Such strain errors are compared to experimentally encountered strains in statistical analyses (see below).

Additionally, *volume errors* were calculated using type A and B strain error data. Statistical analyses were performed to distinguish physiological volume changes (e.g., due to blood expulsion from parts of the lower leg) from those due to artifacts.

Type B strain error data were used also to test if length changes of m. gastrocnemius create discontinuities of deformation at the boundary between this muscle and m. soleus remaining in the globally isometric condition.

4.2.4.2 Statistics. Principal strain distributions by definition deviate from normal distributions. Therefore, for each anatomical region separately, nonparametric Wilcoxon rank sum tests were performed to test for differences between (i) *in vivo* strains and strain errors, and (ii) *in vivo* volume changes and volume errors. The dominant error (either type A or type B) was used in the statistical analyses. The level of significance was chosen at $p<0.05$.

4.3 Results

4.3.1 Artifacts

4.3.1.1 Subject-Repositioning Artifacts. Mean strain errors for all anatomical regions (Table 4.2), as well as volume errors (Table 4.3) are very small.

Table 4.2
Strain errors and principal strains in the deformed state due to changing knee angle

Mean ± SE	m. gastrocnemius	m. soleus	deep flexors	peronei	anterior crural
Strain errors (type A) (synthetic rigid body motion) (n=5)					
Knee angle =173° ± 3°. Ankle angle = 90°					
Strain error	0.009	0.011	0.012	0.024	0.016
(lengthening)	± 0.001	± 0.002	± 0.002	± 0.004	± 0.002
Strain error	-0.009	-0.011	-0.011	-0.020	-0.013
(shortening)	± 0.001	± 0.002	± 0.002	± 0.003	± 0.001
Strain errors (type B) (synthetic known imposed deformation) (n=5)					
Knee angle =173° ± 3°. Ankle angle = 90°					
Strain error	-0.065	0.007	0.007	0.007	0.007
(lengthening)	± 0.037	± 0.001	± 0.001	± 0.001	± 0.001
Strain error	0.030	-0.006	-0.006	-0.006	-0.006
(shortening)	± 0.039	± 0.001	± 0.001	± 0.001	± 0.001
Local principal strains due to changing knee angle (n=5)					
Knee angle =150° ± 6°. Ankle angle = 90°					
First principal strain	0.103	0.085	0.054	0.080	0.102
(lengthening)	± 0.010*	± 0.010*	± 0.008*	± 0.013*	± 0.026*
Third principal strain	-0.097	-0.094	-0.110	-0.079	-0.102
(shortening)	± 0.010*	± 0.003*	± 0.004*	± 0.007*	± 0.021*

* indicates significant differences with the dominant strain error.

4.3.1.2 Algorithm Artifacts. Comparing known imposed deformations within m. gastrocnemius exclusively (Fig. 4.3) to those detected using Demons algorithm indicates the following: At the very boundary between m. gastrocnemius and m. soleus, strain errors are encountered (Fig. 4.3e) and may be high only very locally

(maximal error = 7.88 %). However, the size of such errors declines very rapidly (i.e. within a few voxels distance) to values approaching zero (Fig. 4.3 inset). For locations away from this interface, the analysis indicates the following:

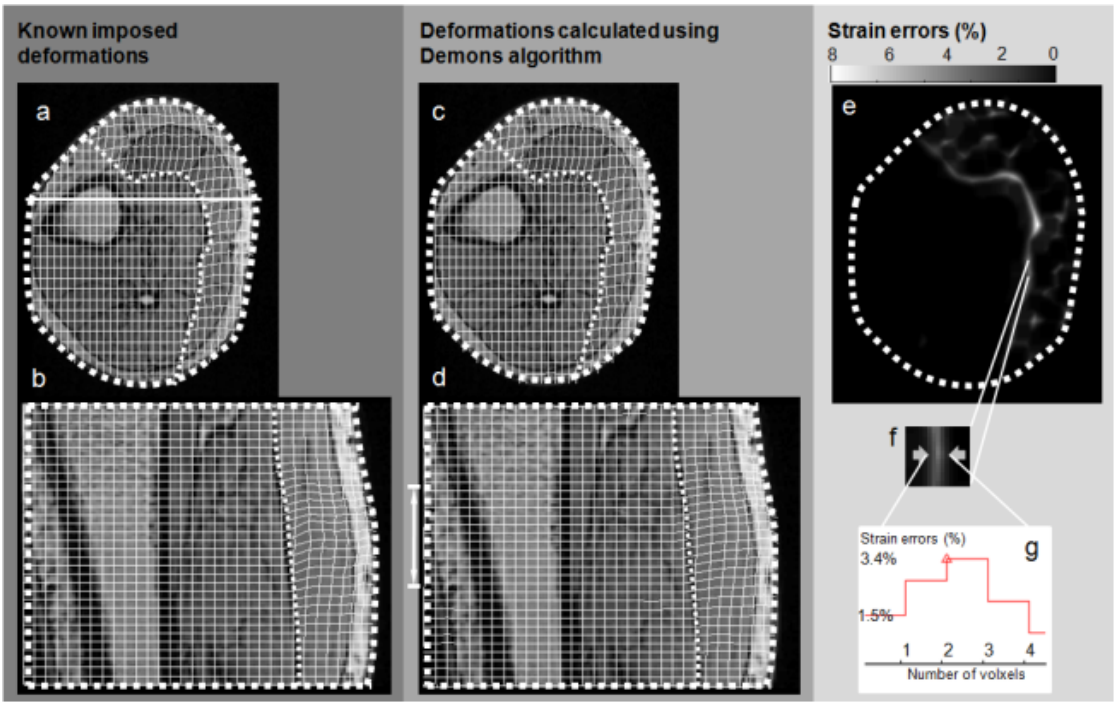

Figure 4.3 Typical example of a validity test: comparison of known imposed deformations and those calculated using Demons algorithm. (a) and (b) Known deformations imposed artificially as shown on cross-sectional and sagittal images, respectively. The white horizontal line in (a) denotes the location of sagittal images shown in (b) and (d). (c) and (d) Corresponding deformations detected using Demons algorithm by comparing original (undeformed) and artificially deformed images. Deformations were visualized on a grid at certain pixel intervals (7x11 pixels, for better visualization of the combined image and grid). Note that deformations are found exclusively within gastrocnemius muscle (i.e. the only location where they had been imposed). (e) Strain errors higher than actually imposed strains are mapped (scaled according to the color grayscale bar on the right). The errors occur particularly at the boundary of deformed and undeformed volumes. The white curve indicates the peak error (7.88 %) occurring at the boundary. For the enlarged part of this curve (f), the decrease in error as a function of distance in voxels is shown in graph (inset g). Note that within 3 voxels, the error decreased below the mean error in deformed volume. The thick white dashed lines (perimeter) delimit the regions of interest within the image and thin white dashed lines separate deformed m. gastrocnemius from the remaining volume. The vertical arrow between (b) and (d) indicates the location of the slice group for which deformations and strains were analyzed due to changing knee angle.

m. gastrocnemius. Mean error strain equaled -6.50 ± 3.70 % and 3.00 ± 3.90 %, for lengthening and shortening respectively (Table 4.2, middle part). This indicates that Demons algorithm tends to underestimate actual strains (peak lengthening and shortening calculated being 13.43 ±3.67 %, -13.21 ± 3.86 %, respectively, while actually imposed peak lengthening and shortening equaled 19.96 ± 5.78 %, -16.22 ± 4.12 %, respectively).

Other muscles and tissues Mean strain errors calculated (Table 4.2) were well below 1.00 %. Volume errors are negligible (Table 4.3).

Table 4.3
Volume errors and tissue volume changes in the deformed state due to changing knee angle

Mean ± SE	m. gastrocnemius	deep flexors	peronei	anterior crural
Volume errors (type A) (synthetic rigid body motion) (n=5)				
Knee angle =173 ° ± 3 °. Ankle angle = 90 °				
Volume error	0.0003	0.0016	0.0034	0.024
	± 0.0004	± 0.0005	± 0.0014	± 0.0019
Volume errors (type B) (synthetic known imposed deformation) (n=5)				
Knee angle =173 ° ± 3 °. Ankle angle = 90 °				
Volume error	-0.0002	0.0000	0.0000	0.0000
	± 0.0008	± 0.0001	± 0.0001	± 0.0001
Tissue volume changes due to changing knee angle (n=5)				
Knee angle =150 ° ± 6 °. Ankle angle = 90 °				
Tissue	-0.0038	-0.0722	0.0094	-0.0299
volume change	± 0.0202	± 0.0155*	± 0.0152	± 0.0150

* indicates significant differences with the dominant volume error.

4.3.1.3 *in vivo* Strains and Volume Changes. Fig. 4.4 shows a typical example of a comparison of grids mapped on the most proximal slice of a sample in the undeformed state (Fig. 4.4a) and in the deformed state (Fig. 4.4b). Hardly any deformations are calculated for bony tissues. Substantial tissue deformations are seen within both heads of m. gastrocnemius. However, despite an absence of any global length changes since they do not cross the knee joint, deformation is seen in m. soleus and synergistic deep flexor muscles also, as well as in antagonistic peroneal and anterior crural muscle groups.

Principal strains (mean ± SE) for each anatomical region are listed (Table 4.2). Significant differences between experimental mean principal strains and error strains indicate that deformation illustrated in Fig. 4.4 are common for all subjects and are therefore typical. Experimental tissue volume changes are significantly different from

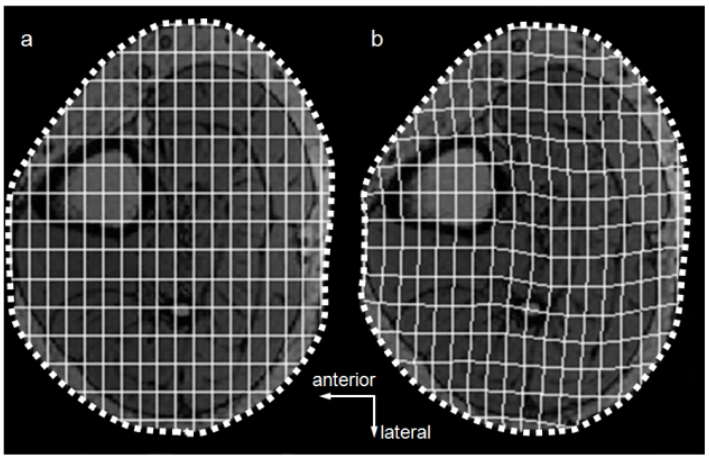

Figure 4.4 A typical example of deformations calculated as caused by changing joint angles. (a) A cross-sectional slice acquired in the undeformed state. A regular grid (made up of lines connecting voxel group centers) is imposed on the image at certain pixel intervals (7x11 pixels) for better visualization. (b) The corresponding slice acquired in the deformed state. Using Demons algorithm, displacement fields are calculated. Based on these displacement fields, the regular grid in (a) is deformed. Such deformed grid is imposed on this image.

volume errors (Table 4.3) only for deep flexor muscles.

Experimentally found results for local deformations are shown in Fig. 4.5. Inter-quartile range (IQR) values indicate heterogeneity of local deformations. Details of local deformation data are provided below:

m. gastrocnemius. Local deformations are substantial (peak lengthening = 34.2 % and shortening = 32.6 %) and heterogeneous across subjects (IQR values for E_1 = 0.060, and for E_3 = 0.073). Peak within subject IQR values equaled 0.091 (subject C) and 0.076 (subject E) for E_1 and E_3, respectively.

m. soleus. Effects of changing knee angle on synergistic soleus muscle have been published in detail [104] and are included in Table 4.2 for completeness only.

Deep flexor muscles. Peak local lengthening = 23.44 % and shortening = 27.35 % (i.e, approximately 68 % and 84 % of values calculated for m. gastrocnemius). IQR values are for E_1 = 0.055, and for E_3 = 0.071. Maximal within subject IQR values equaled 0.068 (subject C) and 0.130 (subject D) for E_1 and E_3, respectively.

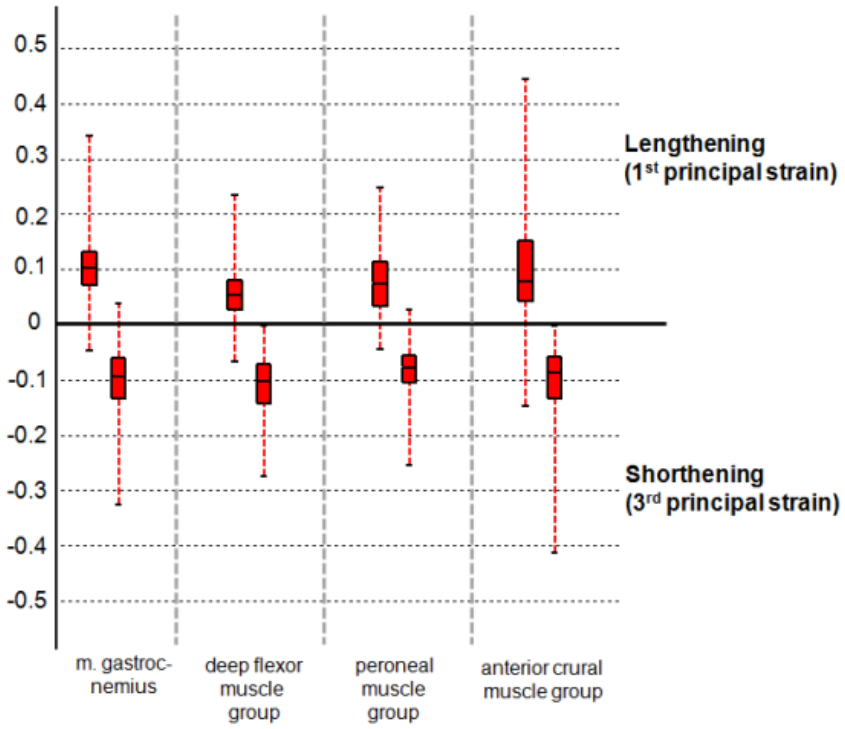

Figure 4.5 Effect of altered knee angle: Local lengthening and shortening effects (first and third principal strain). Box & whisker plots: the horizontal line inside each box represents the median strain value; the upper and lower edges of each box itself represent upper and lower quartiles respectively (i.e., the 75th and 25th percentiles), and lines extending from each end of the box (whiskers) indicate the peak values of the principal strains plotted. Inter-quartile ranges (IQR i.e., absolute value of the difference between upper and lower quartiles) were considered as a measure of strain heterogeneity within each anatomical region. Data were represented per anatomical region of interest (muscle or muscle group) and analyzed across all subjects.

Anterior crural muscles. Peak local lengthening = 44.5 % and shortening = 41.24 %. However, these extremely high values are found only for a minority of the voxels (0.35 % and 1.45 % respectively). For local lengthening and shortening, median strain values were approximately 77 % and 92 % of m. gastrocnemius values, respectively. IQR values are for $E_1 = 0.110$, and for $E_3 = 0.075$. Highest within subject IQR values equaled 0.196 and 0.111 (subject C) for E_1 and E_3, respectively.

Peroneal muscles. Peak local lengthening = 24.77 % and shortening = 25.54 % (approximately 72 % and 78 % of values calculated for m. gastrocnemius). IQR values are for $E_1 = 0.081$, and for $E_3 = 0.049$. Highest within subject IQR values equaled 0.095 (subject D) and 0.052 (subject A) for E_1 and E_3, respectively.

In summary, knee (and hip) angle changes cause substantial and heterogeneous local strains within synergistic, as well as antagonistic muscles of m. gastrocnemius within the lower leg. The results show that within each muscle, both local lengthening and local shortening may occur at different locations.

4.4 Discussion

4.4.1 Intensity Based Non-Rigid Registration as a Tool to Quantify Tissue Deformation

Our main goal was to quantify tissue deformations within a human lower leg, *in vivo*. Previously, real-time MRI techniques have been proposed and are validated for such purpose in cardiac and skeletal muscle: (I) MRI tagging technique validated on cardiac muscles [35] was used in hamstring muscles to evaluate their movement after anterior cruciate ligament reconstruction surgery [105]. (II) Phase contrast imaging was used successfully to show nonuniform strains on m. soleus aponeurosis-tendon complex [36, 37]. (III) Displacement encoding was used to quantify strains in biceps brachii and hamstring muscles [39].

Our present high contrast, high-resolution anatomical images collected contain detailed intensity changes adequate for quantifying voxel-related human muscle strains *in vivo*. Earlier, nonrigid registration techniques were applied mostly to quantify myocardial strain using Cine-MRI of beating hearts [106, 107].

Many improvements were proposed to enhance the accuracy and speed of registration [84, 85, 86]. Tests in subjects against tagged MRI technique showed that the results correlate well. These techniques were applied also to ultrasound images. It was shown that (i) strain values obtained were consistent with Doppler tissue velocity results and (ii) the method was capable of showing myocardial strain differences between healthy and pathological tissues [108, 109, 110].

Previously, success of applying registration algorithms has been tested indirectly. The results were compared with those obtained using other registration methods [111] or even different imaging methods [107]. In addition to a more direct method of testing in which a physical phantom is used [86, 112], a commonly used and reliable method is to use synthetic image sets with known deformations imposed on the test image itself [113, 114]. We applied the latter method in testing validity of present use of Demons algorithm.

The actual synthetic rigid body motion imposed represents a much larger scale motion than possible motion artifacts. Despite that fact, type A strain errors themselves are low (below 2.43 % lengthening and 1.96 % shortening, respectively) and so are their levels of heterogeneity (maximal IQR values equaled 0.013 and 0.014). Such small error levels indicate that the methods applied deal successfully with large rigid body motions that may occur due to experimental repositioning of the subject.

Imposing synthetic known image deformations allows further critical assessments: (1) for the selected volume deformed artificially, very similar displacements to those found in the experiments were imposed. For the deformed volume, this yielded strains of similar order of magnitude as those imposed by image deformation. However, they were somewhat underestimated. Therefore, strains calculated with experimental data will be conservative estimators of actual local deformations. (2) For the remaining volume, absolutely no deformation was imposed creating a challenging registration at the interface with the strained volume. Analysis of such conditions yields two important conclusions regarding Demons algorithms' smoothing effects: (i) No false deformations occur in undeformed tissue. (ii) However, sharp discontinuities in deformation may not be properly handled. Therefore, results for narrow regions forming boundaries between anatomical units need to be interpreted with extreme care. Nevertheless, this applies only to a very limited number of voxels (only approximately 5 % of the voxels studied are located at the intermuscular boundaries). It should also be noted that such discontinuities are not likely to occur during actual tissue movement.

We therefore conclude that Demons algorithm can successfully respond to pos-

sible rigid body motion caused by repositioning of the subject, and can reproduce a known deformation field fairly well. This confirms that it is a suitable method to analyze deformation of muscular tissues *in vivo*.

In previous use of similar image registration, volume changes of muscle (groups) were considered only as parameter to constrain deformations to a constant tissue volume [107, 84]. This stems from a general mechanical consideration that effects of muscle volume changes are trivial [115]. More recent reports show that single twitches of frog muscle causes only a marginal volume change (10-5 ml/g) [116] and for modeled myocardial tissue, volume change remains limited (to 3x10-2 ml/g) [117]. Volume changes calculated presently were marginal for all muscle groups. However, during joint movement, certain volume changes may be physiological, as altered intramuscular pressure may cause changes in arterial flow and venous expulsion [118, 119, 120]. Therefore, "muscle pumps" may cause blood expulsion from veins due to both muscle contraction, and passive length changes accompanying joint movement [121]. Present knee angle changes cause a drop in tissue volume specifically for deep flexor muscles. This suggests that length changes imposed on m. gastrocnemius cause considerable blood expulsion from the deep veins (vv. peroneal and posterior tibial). Therefore, additional to effects on muscle mechanics, quantification of local tissue volume changes may help improving our understanding of such hemodynamics in healthy subjects and in patients with venous dysfunction.

4.4.2 Effects of *in vivo* Myofascial Force Transmission in Human

In the absence of venodynamic effects, significant strain results should be ascribed to mechanical effects between muscles. Major effects of EMFT shown in animal experiments include: (I) Unequal proximal and distal muscle forces (proximo-distal force differences) [12, 13]. (II) Muscle length-force characteristics cannot be considered as unique properties of individual muscles. Key determinants of muscle length-force characteristics [15] (e.g. muscle optimum length and optimal force), as well as the shape of such characteristics [17] were shown to depend strongly on the myofascial

conditions in which the muscle functions. (III) Finite element modeling indicates that EMFT causes major sarcomere length heterogeneity [20, 15, 18] and myofascial loads acting locally on muscle fibers explain this effect in the model. It is also evident that muscle fibers and the extracellular matrix are connected along the muscle fiber [1, 4]. Therefore, forces exerted on sarcomeres by the extracellular matrix and by sarcomeres located in neighboring muscle fibers may cause differences in lengths of serially arranged sarcomeres. Intra- and epimuscular connective tissues are continuous. Therefore, also epimuscular myofascial loads may play a role (see for a specific assessment of the effects of epimuscular myofascial loads [122]). Relative position of muscle with respect to its neighboring structures is a key determinant of EMFT effects [18, 19].

In human, muscle force can usually not be measured directly. Therefore, quantifying e.g., proximo-distal force differences *in vivo* is not an easy task. However, our present approach does allow quantifying effects of epimuscular myofascial loads as tissue deformation. As m. gastrocnemius is a knee flexor, knee movement is to be expected to cause a global strain. However, how knee movement deforms this muscle locally is still interesting and ascribable to EMFT: variable magnitudes of local lengthening are shown to occur simultaneously with local shortening at other locations within the muscle. Muscle modeled at high lengths [15] yielded results in agreement with this: Due to EMFT, not only positive but also negative strains were found along the fiber direction. Accompanying length changes of human m. gastrocnemius, such effects occur also within m. soleus, confirming mechanical interaction between human synergistic muscles, *in vivo* [104].

Animal experiments have also shown interantagonistic EMFT (for a review see [74]): tibial muscle complex force decreases when adjacent peroneal complex is lengthened [123] and EMFT occurs also between more distant muscle compartments [7, 8], yielding a conclusion that EMFT has major effects within the entire lower leg of rodents [8]. Our recent [104] and present results indicate that EMFT has major *in vivo* effects throughout the entire human lower leg.

4.4.3 Limitations and Implications of the Present Study

Our present results were obtained after imposing joint angle changes externally. Theoretically, this would have been possible without muscular activity. However, EMG recordings performed outside the MRI machine indicates that some muscular excitation was present, but small. Nevertheless, we find not only negative strains (that could originate from shortening due to muscle activation), but also high positive strains. Joint movement was shown to cause no significant changes in muscle activity after manipulating ankle joint angle (from neutral to 65° dorsal flexion) [124]. Even for substantial muscular activity (up to 30 %MVC), knee movement imposed externally caused no significant changes in gastrocnemius EMG [125]. On the other hand, at neutral ankle position with the subjects trying to relax, standard deviations of gastrocnemius EMG indicate that across participants' variability of muscle activity is limited to approximately 1/4 of mean EMG values [124]. Therefore, some of the inter-subject variability shown presently may be caused by differences in muscle excitation; however, such effects are expected to be small. It should be noted that due to unavailability of MRI compatible EMG devices, EMG measurements were not made during our experiment.

Local principal strains shown should not be interpreted quantitatively as information regarding sarcomere lengths: (i) the resolution obtained allows the study of muscles or muscle groups instead of individual muscle fibers and sarcomeres. (ii) Length changes specifically along the muscle fiber directions are not estimated. Determining such directions is feasible using MRI diffusion tensor imaging (DTI). Diffusion of water molecules that are encoded within the MRI signal and their principal directions are determined [44, 42]. It has been shown in mouse muscle [126] and human cadavers [127] that such diffusion occurs in parallel to the muscle fiber. A preliminary analysis of our MRI data supports expectations of occurrence of sarcomere length heterogeneity based on our previous modeling work (e.g., [18, 122]): rotation of strain tensors for m. soleus to the muscle fiber direction for each voxel shows major peak lengthening and shortening (56 % and 40 %, respectively) [128]. Analyses of muscle fiber direction strain distributions within other synergistic and antagonistic muscles are indicated. DTI has been used also to show that passive length changes in lower leg

muscles, induced by altered ankle joint angle, affect diffusivity in muscle tissue [129], presumably due to changing muscle fiber dimensions. A role played by myofascial loads in these processes is quite conceivable and should be studied.

Mechanical interaction between the long flexor of the thumb and force exerted at other fingers [80] indicates *in vivo* EMFT in human subjects. However, passive extension of the big toe caused only marginal global displacement of triceps surae muscles [93]. This does not necessarily indicate limited force transmission between triceps surae muscles and the deeper-lying m. flexor hallucis longus, as local deformations were not studied. Huijing et al. [104] showed that global m. gastrocnemius strain ($<$1.5 %) due to imposed knee movement in human cadavers is an order of magnitude smaller than local strains found *in vivo* within that muscle. Recently, actuator independence of cat muscle was studied [91]. At constant ankle and hip joint angles, a robot manipulated knee joint angle, imposing changes of muscular relative positions of passive gastrocnemius and plantaris muscles with respect to partially activated m. soleus. No significant effects on m. soleus ankle moment were shown. Given our present results, the generalizing conclusion drawn that mechanical interaction between muscles does not occur under physiological circumstances *in vivo* is not tenable. Differences in species and actual mechanical conditions (e.g. static versus dynamic, or degree of muscle activation) are plausible sources of divergent results. However, our results suggest that even for conditions in which the net effect of EMFT on forces exerted at the tendon would be small, local heterogeneous effects of epimuscular loads may still be substantial. EMFT effects discussed may affect function substantially, as they refer to mechanical condition dependent contribution of muscles to joint moment and movement. In light of previous and present findings, we conclude that *in vivo*, muscles are, in principle, not independent mechanically due to effects of EMFT.

4.5 Conclusions

Global strains imposed on m. gastrocnemius after knee movement causes substantial and quite heterogeneous local strains to occur, not only within this muscle, but

also within synergistic, as well as antagonistic muscles kept at constant muscle-tendon complex length (global isometric condition). Moreover, variable magnitudes of local lengthening will occur simultaneously with local shortening at other locations. These findings confirm our hypothesis and show that EMFT is a relevant mechanism also *in vivo*.

5. ASSESSMENT OF MYOFASCIAL FORCE TRANSMISSION IN LOCAL FIBERS USING MRI *in vivo*

5.1 Introduction

Aside from myotendinous junctions, force generated by sarcomeres is transmitted along the full periphery of the muscle fibers onto intramuscular connective tissue [100, 2, 130, 131, 132, 97, 20]. The continuity of these connective tissues with perimysium, epimysium, neurovascular tracts, fascia, and compartmental boundaries allows the transmission of force to synergistic muscles as well as antagonistic muscles [9, 12, 11, 13]. The force transmission via this integral system of connections is referred to as epimuscular myofascial force transmission (EMFT) [74].

Previous animal experiments showed that EMFT varies muscle length-force characteristics [15, 17]. Moreover finite element modeling studies indicated that this is caused by changing the sarcomere length distribution arranged in series within muscle fibers [20, 17]. The effects of EMFT in human muscle *in vivo* have been shown recently by our research group using MRI [133]: Global length changes imposed externally on the target muscle-tendon complex by joint movement caused sizable and heterogeneous local principal strains within the target muscle, as well as within the remaining muscles of the human lower leg that were kept isometric. Based on these findings we hypothesized that in the same experimental conditions length changes will occur in local fiber directions. These length changes will be heterogeneous within individual fibers and the mean length changes of fibers will also be heterogeneous. Confirmation of this hypothesis would be an explicit indicator of *in vivo* occurrence of EMFT and its effects on sarcomere length changes that has not been demonstrated previously. Therefore, the aim of the present study was to test this hypothesis using magnetic resonance imaging (MRI) with diffusion tensor imaging (DTI) techniques.

5.2 Methods

5.2.1 Experimental Procedures

5.2.1.1 Subjects. Experimental procedures were in strict agreement with guidelines and regulations concerning human welfare and experimentation set forth by Turkish law, and approved by a Committee on Ethics of Human Experimentation at Istanbul University, Istanbul School of Medicine, Istanbul. Five healthy subjects (mean ± SD: age = 27 ± 3 years, height = 175 ± 7 cm and body mass = 73 ± 8 kg) volunteered for this study. In order to minimize anthropometric differences between subjects (Table 5.1), only males were recruited. After a full explanation of the purpose and methodology of the experiments, the subjects provided an informed consent.

Table 5.1
Anthropometric data

Subject	**Age**	**Height (cm)**	**Mass (kg)**	**Upper leg length (cm)**	**Lower leg length (cm)**
A	29	178	85	41	31
B	31	188	73	46	41
C	23	173	72	41	39
D	25	170	70	45	40
E	30	172	78	42	38

5.2.1.2 Experimental Protocol. Each subject was positioned prone within the MRI scanner. The left leg was brought to a reference position before the patient table (a motorized and computer-controlled slide) was moved into the MRI bore: (I) the ankle angle was fixed at 90° (Fig. 5.1) by using an MRI compatible ankle-foot orthosis (brace on the lower leg and the foot allowing fixation of the ankle angle). (II) To keep orientation of the lower leg constant, the position of the knee cap and the tip of the ankle-foot orthosis were marked on the patient table. (III) The knee angle in this position (*undeformed state*) was (mean ± SD) 173° ± 3°. Based on e.g., [101], knee joint angle was measured using a universal goniometer with its center positioned

over the lateral epicondyle of the femur and its arms aligned with the femur and tibia. After moving the patient table into the bore, sets of 3D high-resolution MR images were acquired in the undeformed state. Subsequently, the patient table was moved out of the bore. The hip and knee joints were brought in flexion by repositioning the upper body using a MRI compatible chest support until the trunk approached the bore wall (diameter 60 cm). In this *deformed state*, the knee angle equaled $150\,^{\circ} \pm 6\,^{\circ}$. Care was taken to maintain the positions of the kneecap and the tip of the ankle-foot orthosis. Subsequently, the patient table was moved back into the bore automatically ensuring that it attains the identical position as during previous image acquisition. Subjects were asked to remain completely relaxed throughout the experiment.

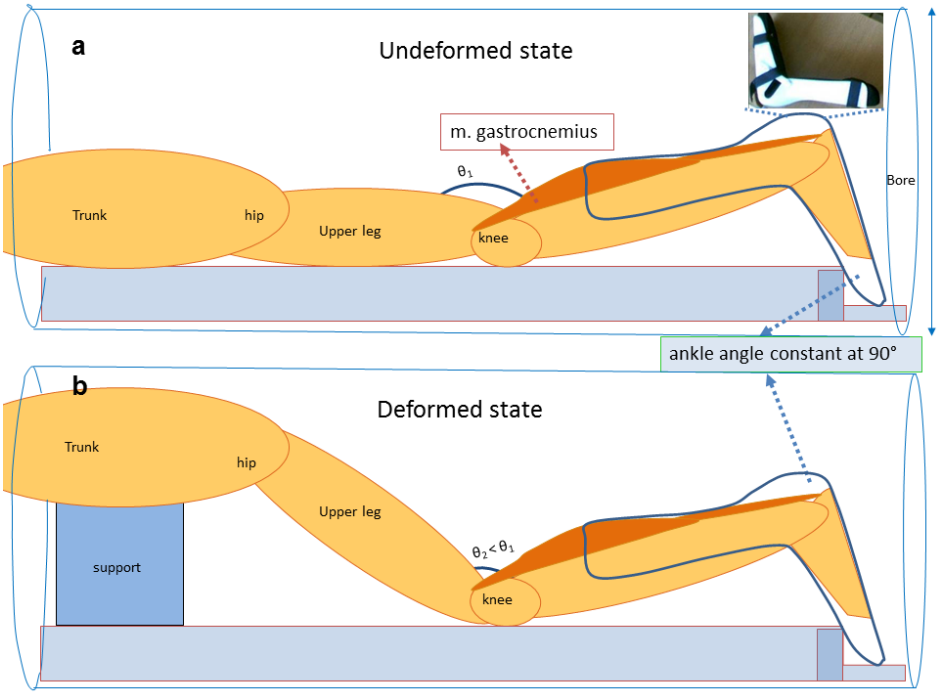

Figure 5.1 Schematic of the leg and trunk within the MRI instrument. (a) The undeformed state. The body is prone on a table (solid line) that is can be moved in and out of the bore of the MRI machine. MRI compatible ankle-foot orthosis (see inset for a picture) was used to fix the ankle angle at $90\,^{\circ}$, in such a way to leave a small space between posterior side of the lower leg and the ankle-foot orthosis and also between anterior side of the lower leg and MR table to avoid exertion of other external forces. The ankle-foot orthosis was secured in the MR table by support materials. The tips of the toes were not allowed to contact the MRI machine in order to prevent the foot from being loaded and any activation of muscles to compensate for that. (b) The deformed state. The trunk of the subject is now supported and brought as close as possible to the bore wall. This creates movement in hip as well as knee joints, but leaves the lower leg in a similar position. In any case the ankle angle is unchanged.

5.2.1.3 Image Acquisition. 3D localizer imaging was performed to plan the subsequent imaging sequences. 3D turbo fast low-angle shot [Turbo Flash] based coronal MR image sets were collected using 3T MR scanner (Magnetom Trio; Siemens, Erlangen, Germany) with 6-channel surface cardiac array coil. The following parameters were used in the Flash sequence: TR = 2000 ms, TE = 3.94 ms, TI = 1100 ms, no fat suppression, flip angle = 12 °, bandwidth = 130 Hz/pixel, number of averages = 1, field of view = 256x256 mm, slice thickness = 0.8 mm (distance factor = 50 %), image matrix size = 320x320x144, voxel size = 0.8x0.8x0.8 mm. Choices of high bandwidth (41600 Hz) and frequency encoding in proximo-distal direction [102] allowed minimizing potential chemical shift artifacts. Imaging time equaled 6 minutes and 50 seconds. Subsequently 2-D axial echo planar imaging (EPI) based diffusion weighted image sets are collected in 6 directions with these parameters: TR = 2500 ms, TE = 84 ms, flip angle = 90 °, bandwidth = 955 Hz per pixel, number of averages = 5, field of view = 140x224 mm, slice thickness = 8 mm, image matrix size = 160x256x20, voxel size = 0.875x0.875x8 mm, b = 500 s/mm^2. Note that subject position was fixed so that physical coordinates (provided by MRI scanner) of the corresponding voxels from these two different types of image sets would be the same in order to match them.

5.2.1.4 EMG Assessment of Subject Relaxed State. In order to confirm the subject's relaxed state during the experiments, an EMG test was performed (n = 1). Pre-amplified bi-polar surface EMG (Delsys, Trigno Wireless, Boston, MA, USA) was used. Electrodes were located over mid muscle belly of m. gastrocnemius and m. tibialis anterior. This showed that in the final isometric states, EMG activity was very low for both muscles: root mean square values of full wave rectified low pass filtered EMG data normalized for subject's EMG during maximal voluntary contraction (MVC) was less than 0.5 % of the respective MVC value.

5.2.2 Calculation of *in vivo* Strains

A slice group consisting of 30 consecutive cross-sectional slices was selected manually for each subject (Fig. 5.2a): the most proximal slice location was at the proximal third of the length of imaged portion of the lower leg (corresponding to mid-m. gastrocnemius belly).

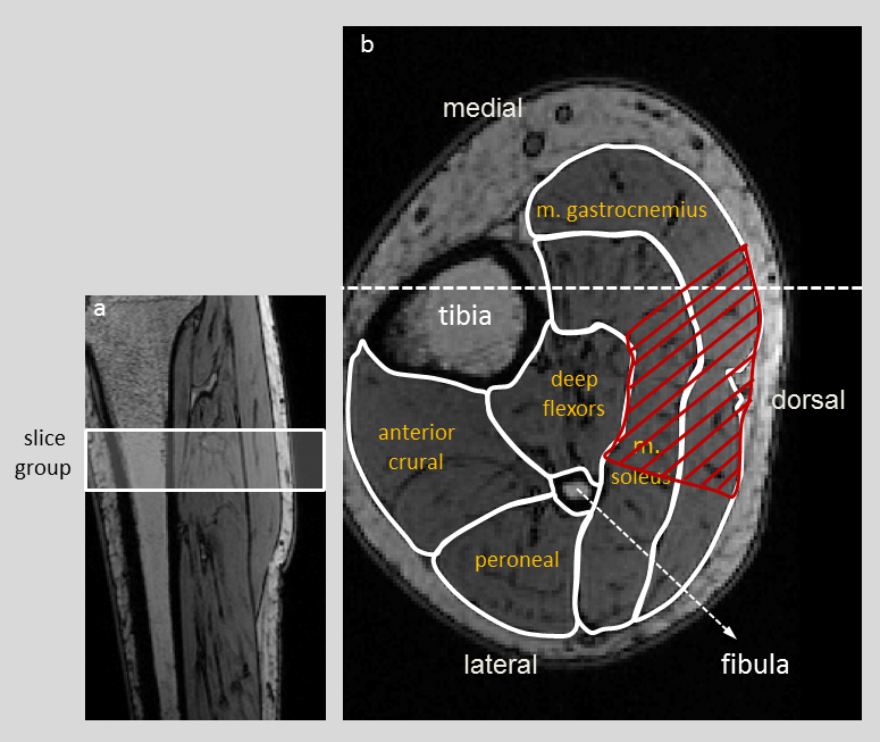

Figure 5.2 Examples of MR images of the lower leg. (a) Longitudinal anatomic image of the lower leg representing a sagittal slice illustrating the locations of the group of cross-sectional slices to be analyzed for strains. For all subjects, the most proximal axial slice of the slice group was located at the upper third of the imaged portion of the lower leg, a level corresponding to the mid-belly of m. gastrocnemius. (b) An example of a cross-sectional anatomic image of the slice group with anatomical identification of muscles or muscle groups and bones (tibia and fibula). Five anatomical regions of interest were distinguished: m. gastrocnemius, m. soleus, deep flexor muscles, peroneal muscles and anterior crural muscles. The dashed horizontal line indicates the location of sagittal image shown in (a).

Within each slice analyzed, five anatomical regions representing m. gastrocnemius, m. soleus, deep flexor muscles, peroneal muscles and anterior crural muscles were distinguished manually by outlining their boundaries (Fig. 5.2b).

Deformations caused by knee joint angle changes i.e., *in vivo strains* were calculated. In order to do that, MR images acquired in the deformed and undeformed

states were aligned. Demons algorithm [41] i.e., a non-rigid and non-parametric image registration technique was applied. Utilizing arrays of voxel grayscale values, this algorithm relies on (i) *gradients of images* and (ii) *differences between images* i.e., differences between voxel grayscale values of consecutive voxels within each image and corresponding voxels in deformed and undeformed images, respectively. Image differences calculated iteratively are used to characterize displacement values for each voxel. During each iteration, updated displacement fields are smoothed by a Gaussian kernel for regularization of local displacements and global motion. Finally, after a successful alignment of images obtained by minimizing image differences, information on real deformation is available for each cubic shape comprised of four adjacent image voxels. See Appendix A for detailed descriptions of the steps of Demons algorithm.

Using displacement fields obtained, deformation gradient matrix F, characterizing voxel deformation, was calculated by using displacement gradient (∇u) in material coordinates:

$$F = \nabla u + I \tag{5.1}$$

Green-Lagrange strain tensor E was calculated for each voxel in order to assess deformations within the lower leg muscles present after changing the knee and hip angles:

$$E = \frac{1}{2}\left[F^T F - I\right] \tag{5.2}$$

5.2.3 Calculation of Diffusion Tensors

In order to obtain local muscle fiber direction per voxel diffusion tensor (DT) was calculated from diffusion weighted image set. The noise in images may cause negative semi-definite tensors which is physically meaningless. Therefore nonlinear computation algorithm (3dDWItoDT) included in AFNI (well-known software package for analysis and visualization of functional MRI neuroimages) [134] was used which constraints

diffusion tensors to be positive semi-definite matrices.

5.2.4 Matching Corresponding Voxels

The anatomic and diffusion weighted image sets were taken in different planes (coronal and axial, respectively) and had different voxel sizes. Therefore voxels of these different types of image sets had to be matched using their common physical reference coordinates provided by MRI scanner: two global transformation matrices were calculated between (i) diffusion weighted image coordinate system and physical coordinate system of MRI scanner (Fig. 5.3a) and (ii) physical coordinate system and anatomic image coordinate system (Fig. 5.3b). These transformation matrices were multiplied so that one transformation matrix was attained in order to (i) rotate diffusion tensors into anatomic image coordinate system and (ii) subsequently match corresponding voxels within different types of image sets by nearest neighborhood interpolation.

5.2.5 Calculation of Strains in Local Muscle Fiber Directions

After rotating and mapping diffusion tensors to anatomic image coordinate system, 3 principal diffusion values ($\lambda_1 > \lambda_2 > \lambda_3$) and their corresponding orthogonal directions were calculated from diffusion tensors to find local muscle fiber based coordinate system per voxel: The axis in the direction of maximal principal diffusion corresponded to local muscle fiber direction. The strain tensors were then rotated to local muscle fiber based coordinate system (Fig. 5.3c):

$$E_r = RER^T \tag{5.3}$$

where, R was the rotation matrix described by local fiber based coordinate system and E_r was the rotated strain tensor. Normal strain in local fiber direction corresponded to length changes in fiber direction.

For each anatomical region separately, the strains in local fiber directions were

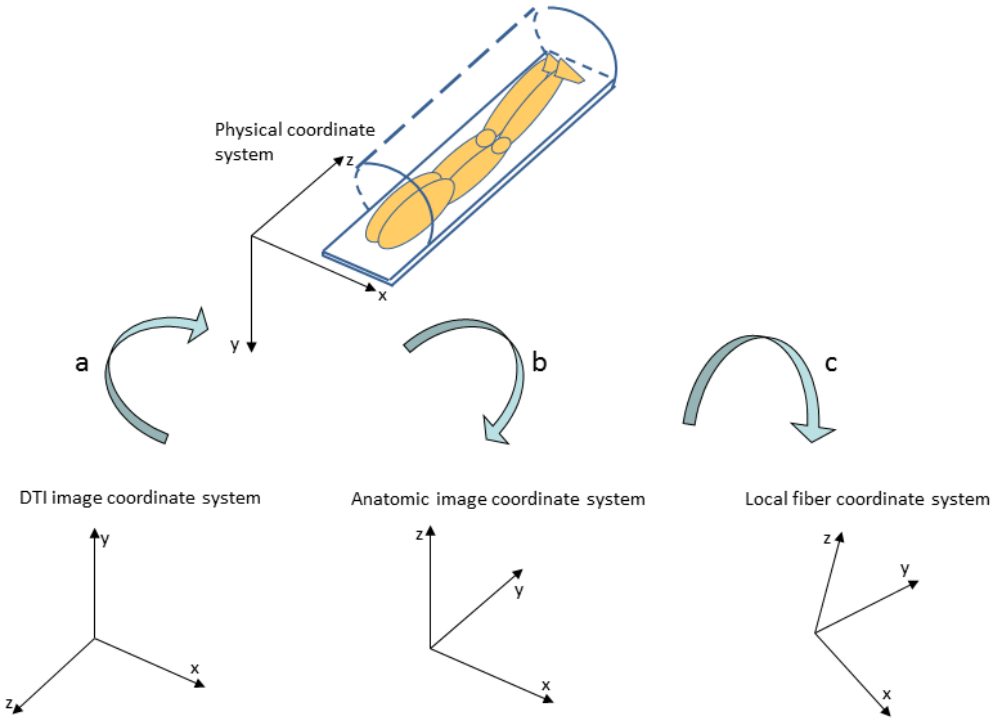

Figure 5.3 Schematic of the coordinate transformations. Coordinate transformation is performed (a) from DT image coordinate system to physical coordinate system, then (b) from physical coordinate system to anatomic image coordinate system to match voxels. (c) Each strain tensor is rotated to local fiber coordinate system using a local rotation vector derived from diffusion tensor in order to calculate local fiber direction strains.

calculated and mean ± SE values were reported separately. In addition, heterogeneity of deformation was analyzed within anatomical regions distinguished.

5.2.6 Initial Tests of the Limitation of the Registration Algorithm

The validity of Demons algorithm in quantifying tissue deformations was shown after performing vigorous testing [133]. Presently, image sets of the undeformed state were transformed by a "synthetic rigid body motion" imposed on the data for each subject: (i) a 10° rotation within the cross-sectional plane (corresponding to an endorotation of knee as the knee flexed [87]), (ii) a 3° rotation in the coronal plane, (iii) a 3° rotation in the sagittal plane and (iv) a 4 mm translation in the axial direction.

Subsequently, image sets of the undeformed state and the transformed image set were compared and apparent strains were calculated. Theoretically, rigid body motion, as imposed in this validation test, should not cause any strains. Therefore, any strains calculated accordingly represent artifacts, which may arise from the algorithm e.g., when there is subject motion or due to subject-repositioning between conditions tested.

5.2.7 Distinguishing *in vivo* Deformations from Artifacts Statistically

Principal strain distributions by definition deviate from normal distributions. Therefore, for each anatomical region separately, nonparametric Wilcoxon rank sum tests were performed to test for differences between *in vivo* strains and strain artifacts. The level of significance was chosen at $p < 0.05$.

5.2.8 Calculation of Fractional Anisotropy (FA) and Fiber Tracking

Fractional anisotropy (FA) was calculated from diffusion values ($\lambda_1 > \lambda_2 > \lambda_3$) and their means ($\bar{\lambda}$) for each voxel:

$$FA = \sqrt{\frac{3 \times \left(\left(\lambda_1 - \bar{\lambda}\right)^2 + \left(\lambda_2 - \bar{\lambda}\right)^2 + \left(\lambda_3 - \bar{\lambda}\right)^2\right)}{2 \times (\lambda_1^2 + \lambda_2^2 + \lambda_3^2)}} \tag{5.4}$$

Possible effects of changing knee angle on longitudinal diffusivity (i.e. largest principal diffusion value: λ_1), transversal diffusivity (i.e. average of λ_2 and λ_3) and FA were assessed for each anatomical region.

Fiber tracking was based on a line propagation algorithm by which lines were propagated according to the local fiber direction at each voxel in a selected region of interest [135]. The paths of fiber bundles were constructed until stop criterion (i.e. low FA or large deviation of orientation) was reached. Small region of interest (shaded

area in Fig. 5.2b) within middle part of m. gastrocnemius and m. soleus was selected for better visualization of fiber strain distribution on fiber bundles. Subsequently, fiber tracking (n=1) was performed to assess (i) the heterogeneity of local fiber direction strains along fiber bundles (referred to as serial distribution) and (ii) the heterogeneity of mean fiber direction strains among fiber bundles (referred to as parallel distribution).

5.3 Results

5.3.1 Initial Tests of the Registration Algorithm

Mean strain artifacts for all anatomical regions (Table 5.2) are very small. This shows that the errors caused by subject motion or subject-repositioning do not effect the quantified deformations of muscle groups. These baseline strains are similar for all muscle groups.

Table 5.2
Baseline strains and tissue strains in local fiber directions in the deformed state

Mean ± SE	m. gastrocnemius	m. soleus	deep flexors	peronei	anterior crural
Local baseline strains (synthetic rigid body motion) (n=5)					
Knee angle =173 ° ± 3 °. Ankle angle = 90 °					
Positive strains	0.004	0.004	0.004	0.003	0.003
(lengthening)	± 0.001	± 0.001	± 0.001	± 0.001	± 0.001
Negative strains	-0.004	-0.004	-0.003	-0.004	-0.003
(shortening)	± 0.001	± 0.001	± 0.001	± 0.002	± 0.000
Local tissue strains in the deformed state (n=5)					
Knee angle =150 ° ± 6 °. Ankle angle = 90 °					
Positive strains	0.048	0.036	0.028	0.031	0.047
(lengthening)	± 0.004*	± 0.003*	± 0.002*	± 0.004*	± 0.010*
Negative strains	-0.048	-0.040	-0.045	-0.031	-0.053
(shortening)	± 0.002*	± 0.002*	± 0.004*	± 0.003*	± 0.013*

* indicates significant differences with the strain error.

Using AFNI's nonlinear algorithm (3dDWItoDT) only 0.2 % of DTs remained

negative semi-definite. Note that those tensors belonged to skin and bones which do not exist within anatomical regions (i.e. muscle groups) focused.

5.3.2 *in vivo* Strains

Mean tissue strains (lengthening and shortening values separately) were significantly higher than strain artifacts (Table 5.2). Experimentally found results for local deformations in fiber directions are shown in Fig. 5.4. Inter-quartile range (IQR) values indicate heterogeneity of local deformations. Details of local deformation data are provided below:

5.3.2.1 m. gastrocnemius. Local deformations are substantial (peak lengthening = 33.10 % and shortening = 27.31 %) and heterogeneous across subjects (IQR value = 0.082). Maximal within subject IQR value equaled 0.086 (subject C).

5.3.2.2 m. soleus. Peak local lengthening = 20.77 % and shortening 22.98 % (i.e. approximately 63 % and 84 % of the values calculated for m. gastrocnemius). IQR value is 0.067. Maximal within subject IQR value equaled 0.069 (subject E).

5.3.2.3 Deep flexor muscles. Peak local lengthening = 19.71 % and shortening = 26.97 % (i.e. approximately 60 % and 99 % of the values calculated for m. gastrocnemius). IQR value is 0.060. Maximal within subject IQR value equaled 0.070 (subject E).

5.3.2.4 Anterior crural muscles. Peak local lengthening = 38.78 % and shortening = 36.40 %. However, these extremely high values are found only for a minority of the voxels (0.02 % and 0.31 %, respectively). For local lengthening and shortening,

median strain values were approximately 74 % and 97 % of m. gastrocnemius values, respectively. IQR value is 0.068. Highest within subject IQR value equaled 0.080 (subject B).

5.3.2.5 Peroneal muscles. Peak local lengthening = 22.05 % and shortening = 22.39 % (approximately 67 % and 82 % of values calculated for m. gastrocnemius, respectively). IQR value is 0.048. Highest within subject IQR value equaled 0.059 (subject E).

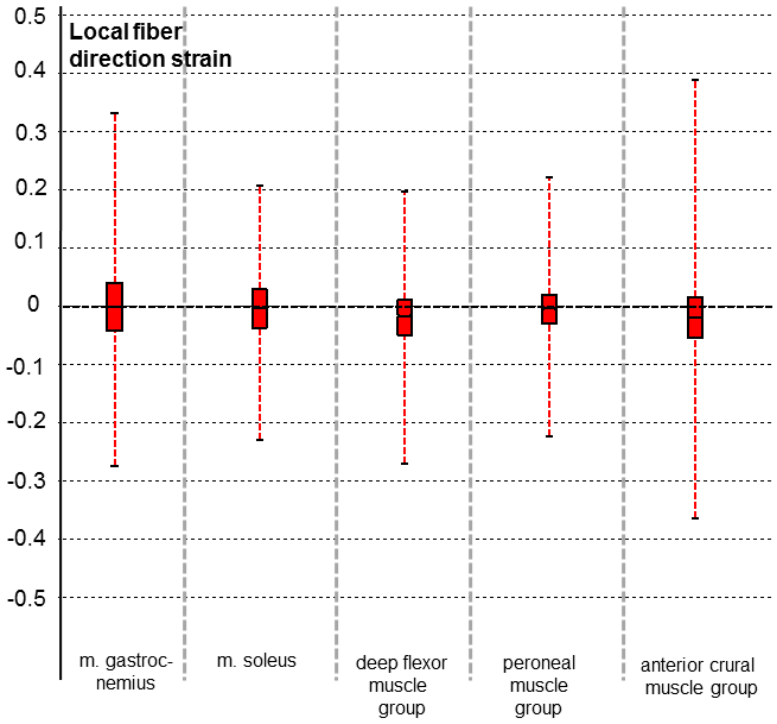

Figure 5.4 Effect of altered knee angle: Local lengthening and shortening effects (local fiber direction strain). Box & whisker plots: the horizontal line inside the box represents the median strain value; the upper and lower edges of a box itself represent upper and lower quartiles respectively (i.e., the 75th and 25th percentiles), and lines extending from each end of the box (whiskers) indicate the peak values of the strains plotted. Inter-quartile ranges (IQR i.e., absolute value of the difference between upper and lower quartiles) were considered as a measure of strain heterogeneity within each anatomical region. Data were represented per anatomical region of interest (muscle or muscle group) and analyzed across all subjects.

5.3.2.6 Diffusivity and FA. Longitudinal diffusivity (λ_1) and FA values for each anatomical region are listed in Table 5.3. Change in FA, longitudinal and transversal diffusivities caused by knee movement were not significant ($p<0.05$) for all muscle

groups. In all muscle groups negligible fiber direction strains have been found within voxels whose longitudinal (Fig. 5.5) and transversal (Fig. 5.6) diffusivities are very small or very high. In contrary, fiber direction strains in voxels whose longitudinal diffusivity is around median can reach peak values. In all muscle groups negligible fiber direction strains have been found within voxels whose fractional anisotropy values are very high (Fig. 5.7).

Table 5.3
Longitudinal diffusivity and FA values

Mean ± SE	m. gastrocnemius	m. soleus	deep flexors	peronei	anterior crural
In the undeformed state (n=5)					
Knee angle =173 ° ± 3 °. Ankle angle = 90 °					
$\lambda_1(\times 10^{-3} mm^2 s^{-1})$	1.98	2.14	1.88	1.86	1.66
	± 0.08	± 0.06	± 0.01	± 0.01	± 0.07
FA	0.34	0.36	0.35	0.39	0.35
	± 0.02	± 0.03	± 0.02	± 0.01	± 0.02
In the deformed state (n=5)					
Knee angle =150 ° ± 6 °. Ankle angle = 90 °					
$\lambda_1(\times 10^{-3} mm^2 s^{-1})$	1.86	2.10	2.10	1.82	1.72
	± 0.04	± 0.05	± 0.10	± 0.07	± 0.07
FA	0.33	0.39	0.36	0.38	0.33
	± 0.02	± 0.02	± 0.02	± 0.01	± 0.01

5.3.2.7 Serial local fiber direction strain distribution. Heterogeneity in serial local fiber direction strains was highly pronounced (Fig. 5.8a): For m. gastrocnemius IQR values of serial fiber direction strains ranged from 0.001 to 0.224. Even m. soleus was kept isometric; IQR values of serial fiber direction strains (ranged from 0.000 to 0.161) were substantial. These ranges and histograms (Fig. 5.8b for m. gastrocnemius and Fig. 5.8c for m. soleus, respectively) show that IQR values themselves were quite heterogeneous. This indicates heterogeneity in both serial and parallel distributions of fiber direction strains.

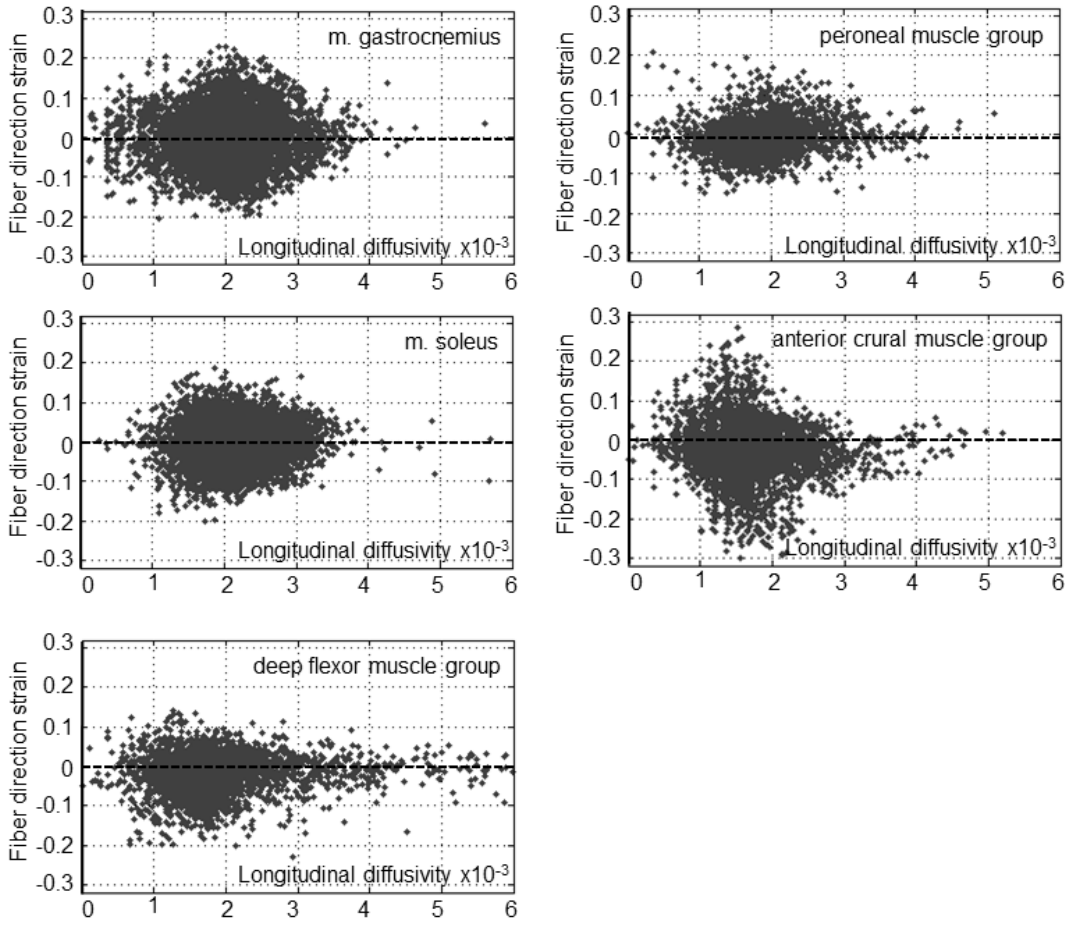

Figure 5.5 Relation longitudinal between diffusivity (x$10^{-3}mm^2s^{-1}$) and local fiber direction strain. For each anatomical region of interest (muscle or muscle group) each scatter plot shows the relation between the longitudinal diffusivity and fiber direction strain across all subjects.

5.3.2.8 Parallel local fiber direction strain distribution. Heterogeneity in parallel local fiber direction strains was highly pronounced: IQR value of mean length changes of fiber bundles were 0.039 for both m. gastrocnemius and m. soleus in selected region of interest.

It is concluded that (I) knee (and hip) angle changes cause substantial local fiber direction strains within synergistic, as well as antagonistic muscles of m. gastrocnemius within the lower leg even if the length of muscle-tendon complexes are kept isometric, (II) the patterns of strains are not simple ones: (a) it differs per muscle or muscle group and (b) at different locations even within one muscle sizable local lengthening occurred simultaneously with local shortening, and (III) knee movement causes heterogeneous

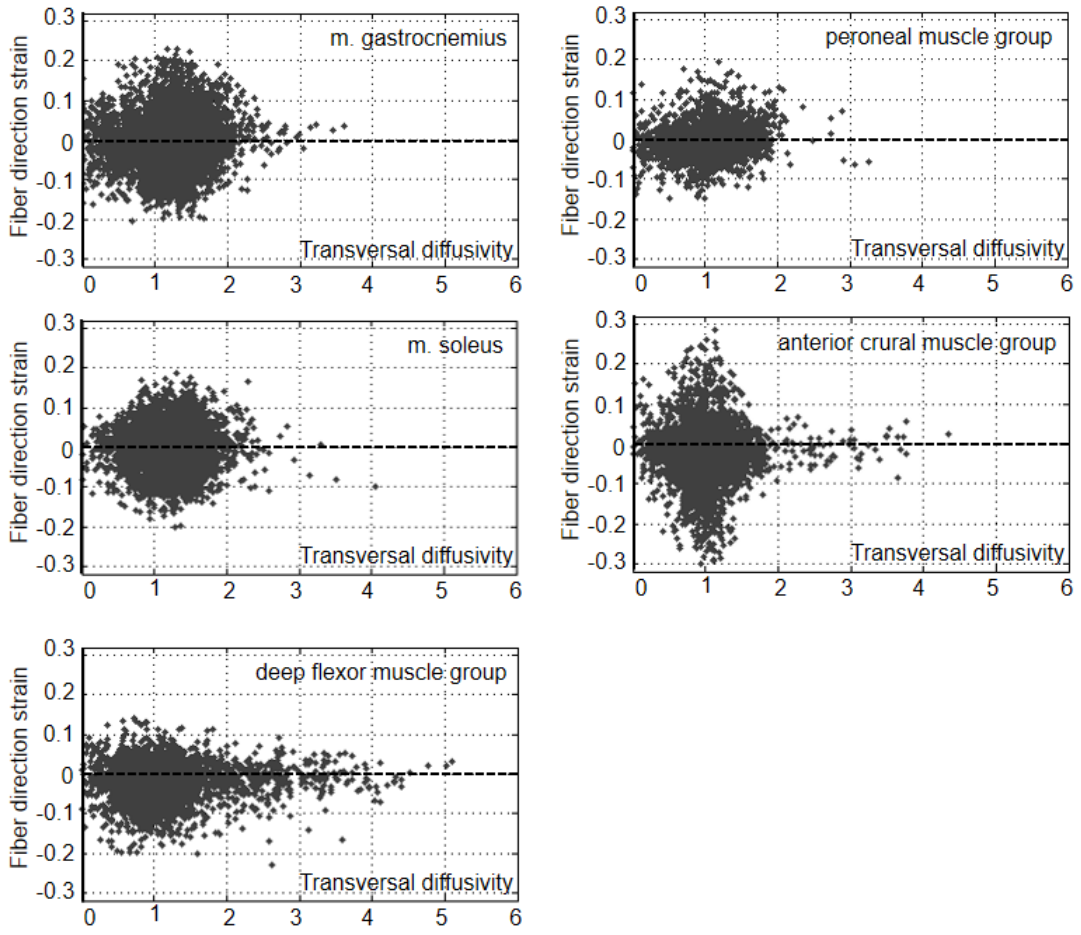

Figure 5.6 Relation between transversal diffusivity (x$10^{-3}mm^2s^{-1}$) and local fiber direction strain. For each anatomical region of interest (muscle or muscle group) each scatter plot shows the relation between the transversal diffusivity and fiber direction strain across all subjects.

length changes not only along fibers (serial distribution of strains) but also among fibers (parallel distribution of strains).

5.4 Discussion

5.4.1 Combination of Intensity Based Non-rigid Registration and Diffusion Tensor Imaging as a Tool to Quantify Fiber Direction Strain

In this study, *in vivo* quantification of local fiber direction strains within human lower leg was explored as changing knee (and hip) angles. Previously only local

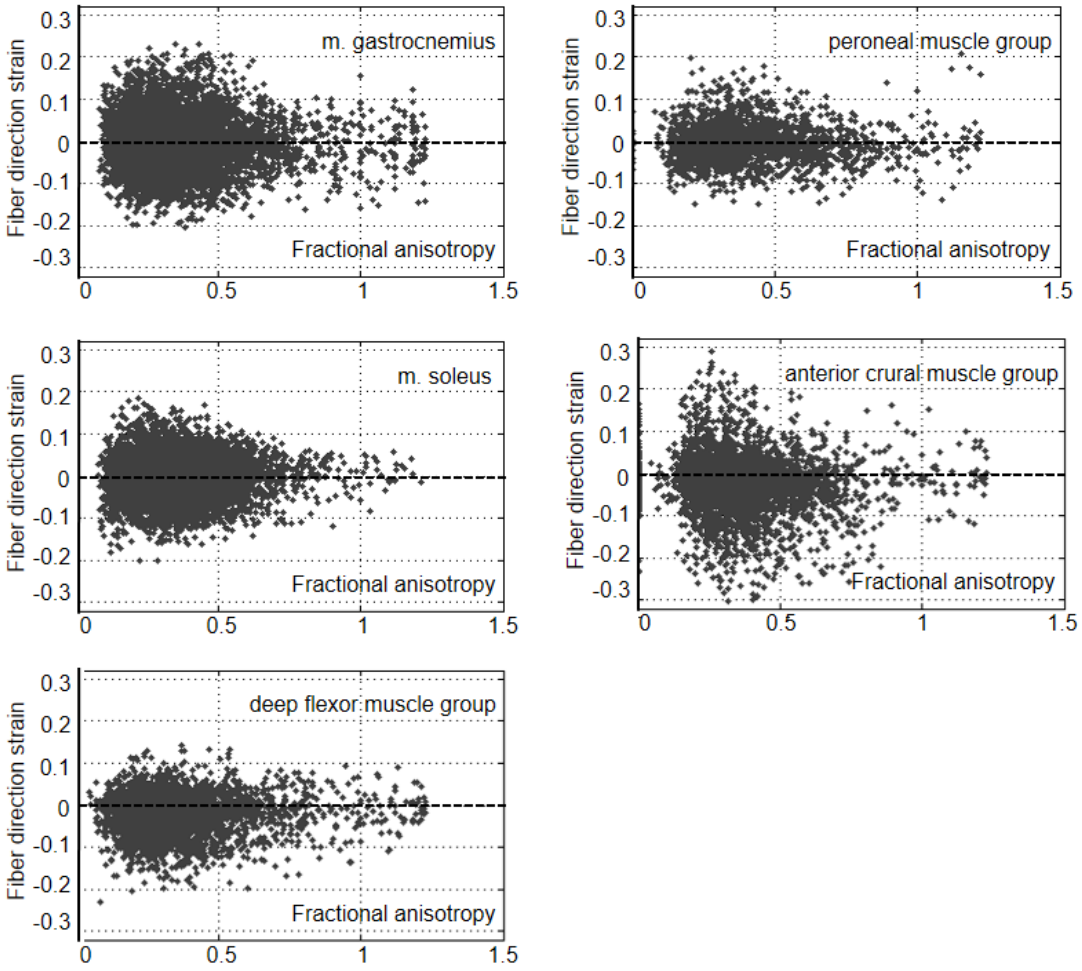

Figure 5.7 Relation between fractional anisotropy (x$10^{-3} mm^2 s^{-1}$) and local fiber direction strain. For each anatomical region of interest (muscle or muscle group) each scatter plot shows the relation between the fractional anisotropy and fiber direction strain across all subjects.

principal strains (i.e. peak lengthening and shortening) were calculated in order to assess the effects of changing knee angle on local tissue deformations without giving any information about local fiber direction strains [133]. Englund et al. [136] calculated linear strains in six directions from spatially tagged images during submaximal (50 %) isometric contraction of the tibialis anterior muscle and combined them within 3x3 strain tensors. Additionally, they acquired diffusion weighted images and calculated diffusion tensors in order to compare local peak lengthening and shortening (i.e. positive and negative principal strains) and local fiber directions. Again local fiber direction strains were not calculated in this study. On the other hand, their technique has advantage in quantifying strains caused by active isometric muscle motion. However, to avoid fatigue, imaging time is reduced: (i) spatial tagging MRI was chosen rather

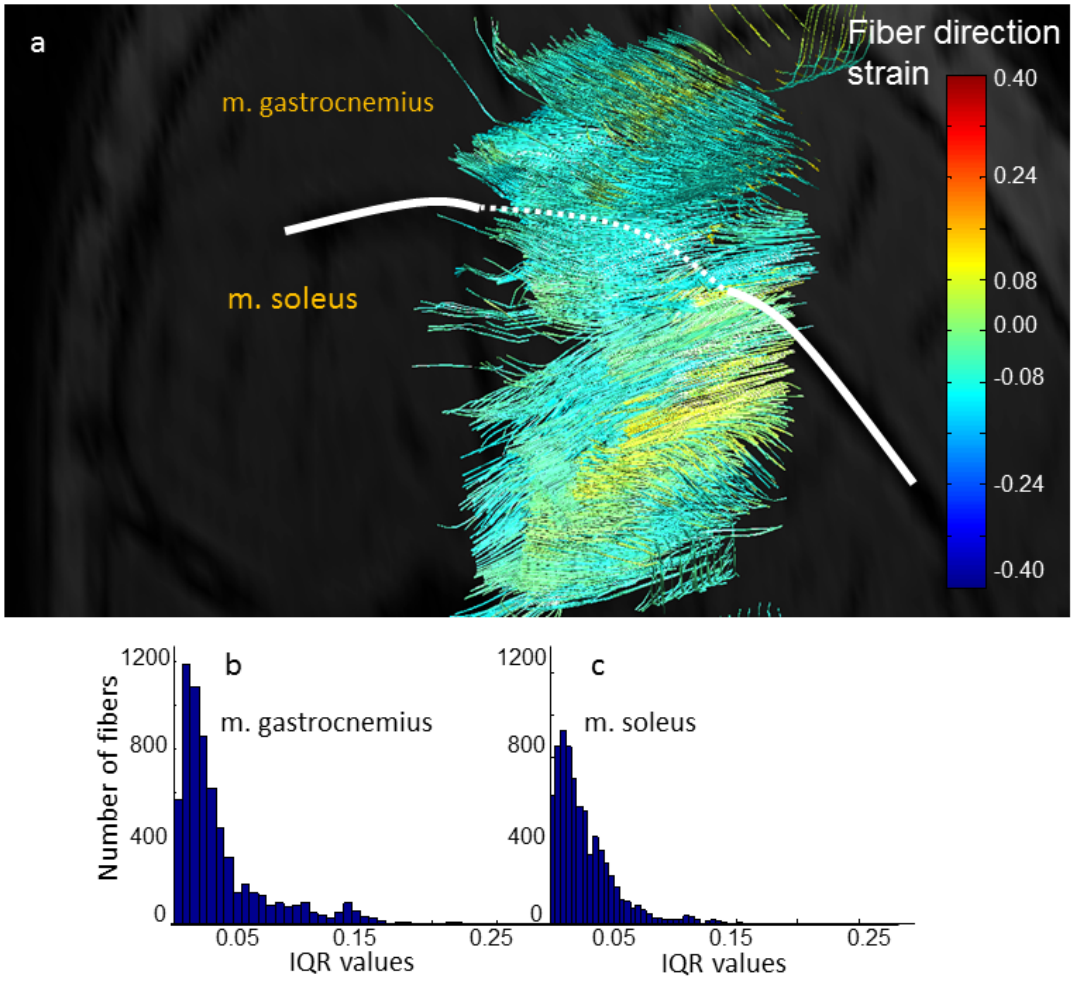

Figure 5.8 Example of fiber tracking. (a) Selected region of interest located within lateral gastrocnemius and soleus is delimited by red line. (b) White line separates the fiber bundles of m. gastrocnemius and m. soleus tracked within selected region of interest. Colors on fiber bundles represent local fiber direction strains. (c) Histogram of IQR values of m. gastrocnemius fiber bundles. (d) Histogram of IQR values of m. soleus fiber bundles.

than phase-contrast MRI, (ii) it was applied to small regions of interest on superficial and deeper tibialis anterior muscle, (iii) its resolution (slice thickness and tag intervals equaled 7.1 mm) was selected quite low compared to the resolution (0.8x0.8x0.8 mm voxel size) in the present study to reduce imaging time. Note that in the present study, (i) the muscle motion is passive causing less fatigue, (ii) local fiber direction strains are calculated not only within tibialis anterior but also its synergistic and antagonist muscles.

5.4.2 Relation between Diffusivity, Fractional Anisotropy and Local Fiber Direction Strain

The effect of passive knee and ankle angle changes on diffusion parameters (apparent diffusion coefficients and FA) was found pronounced in human tibialis anterior [137, 129] and calf muscles [138], respectively. We found no significant change in FA, longitudinal and transversal diffusivity related to knee angle change. Note that in previous studies joint movements were major functions of the focused muscles as opposed to the present experimental scenario: Knee angle change is the secondary function of m. gastrocnemius.

The scatter data across all subjects showed that sizable local fiber direction strains occur around median longitudinal (Fig. 5.5) and median transversal diffusivity (Fig. 5.6) for each muscle groups. It can be explained that median value corresponds to the resting length of fibers and therefore those fibers are capable of pronounced lengthening or shortening. Voxels with small diffusivity values have small fiber direction strains: the fibers are already shortened, thus they are less available to change their length. Voxels with large diffusivity and FA (Fig. 5.7) values have small fiber direction strains: the fibers are lengthened already, thus changing knee angle has little or no effect in their length.

5.4.3 Effects of *in vivo* Myofascial Force Transmission in Human

Previous animal experiments and finite element modeling showed that EMFT causes: (I) Unequal proximal and distal muscle forces [12, 13], (II) Muscle length-force characteristics depends also on the myofascial conditions [17, 122], (III) Local myofascial loads cause major sarcomere length heterogeneity [20, 15, 122, 18]. It was shown that EMFT is capable of causing these effects within the entire lower leg of the rat [8]. Our recent study supports this finding in human lower leg muscle *in vivo* by quantifying deformations caused by passive knee angle change [133]. In similar experimental conditions, the present study benefits from DTI in order to quantify

deformations in local fiber directions. Despite local fiber direction strains do not refer directly to sarcomere length changes and therefore sarcomere length heterogeneity, it points out that EMFT causes major local fiber length changes within the entire human lower leg *in vivo*. The size of these effects differs among subjects as emphasized previously for both passive [133] and active motion [136].

5.4.4 Heterogeneities in Local Fiber Direction Strains

Using finite element modeling it was shown previously that continuity of intramuscular connective tissues to inter- and extramuscular connective tissues causes heterogeneity in the length of sarcomeres in series within the same individual muscle fiber [20, 15]. This changes the length between active slack and optimum lengths, eventually alters muscle force production characteristics. This heterogeneity increases the mean sarcomere length of each fiber which causes heterogeneity in parallel distribution of length of sarcomeres. Heterogeneities in both serial [139] and parallel distributions [140] were shown to lead improved range of muscle length. Present findings are consistent with the results of previous finite element modeling studies and indicate the effects of EMFT on length heterogeneity of fibers in series and parallel. To our knowledge this is the first study that showed the effects of EMFT on fiber length distributions in human muscles *in vivo*.

5.4.5 Limitations and Implications

Pilot EMG study performed outside the MRI scanner indicates that muscular activity is small during passive joint angle change. Even that activity causes negative strains in local fiber direction; positive strains cannot be explained by muscle excitation. Knee movement was shown to cause no significant changes in gastrocnemius EMG even for sizable muscular activity of 30 % MVC [125]. Note that muscular activity may have small effects on intersubject variability: Standard deviations of gastrocnemius EMG indicate that subjects' variability of muscle activity is limited to 1/4 of mean

EMG values at neutral ankle position with the subjects trying to relax [124]. EMG measurements were not made at the time of our experiment due to unavailability of MRI compatible EMG devices.

New MRI techniques have been focused in recent years. (I) Real-time DTI is aimed to estimate diffusion parameters during the repetition time of the sequence [141, 142]. This new method is promising for its potential application in clinic. (II) Strain encoding imaging (SENC) is performed by encoding a pattern similar to tagging into the tissue. The intensity in SENC images depend on local strains in a specific direction [40]. (III) Magnetic resonance elastography (MRE) benefits from the propagation of shear waves into the tissue and images the mechanical properties of soft tissues [143, 144, 145]. Using these three techniques one can measure not only local strains and fiber directions locally, but also local stiffness in order to show the effects of EMFT more precisely. Using these techniques it is also possible to relate the nonmuscular connective tissues and their local effects directly.

In a recent study, at fixed ankle and hip joint angles, using a robot, relative positions of passive gastrocnemius and plantaris muscles were changed with respect to partially activated m. soleus [91]. As a result, ankle moment of m. soleus was not significantly changed. Nevertheless Huijing et al. showed that global m. gastrocnemius strain ($<$1.5 %) is much smaller than local strains found *in vivo* (10.3 $\pm$ 1.0 % and -9.7 $\pm$ 1.0 % for lengthening and shortening, respectively) within the same muscle [104]. The projection of such local strains on local fiber direction strains is given in the present study as 4.8 $\pm$ 0.4 and -4.8 $\pm$ 0.2 %. Thus, even the net effect of EMFT on distal end of the muscle would be small, epimuscular loads may still be pronounced locally. Such heterogeneous effects may change the mechanical conditions of muscles and affect the force production capability.

5.5 Conclusion

Global strains imposed by passive knee movement causes substantial and quite heterogeneous local fiber direction strains to occur, not only within m. gastrocnemius, but also within its synergistic, as well as antagonistic muscles kept at constant muscle-tendon complex length (global isometric condition). Moreover, variable magnitudes of local lengthening will occur simultaneously with local shortening at other locations and even within the same fiber. These findings confirm our hypothesis and show that EMFT is a relevant mechanism also *in vivo*. In light of previous and present findings, we could now more firmly postulate that *in vivo*, muscles are, in principle, not independent mechanically due to effects of EMFT.

6. MRI ASSESSMENT OF EXTERNAL MECHANICAL LOADING ON HUMAN LOWER LEG MUSCLES *in vivo*

6.1 Introduction

Fascia has an important role in posture and movement. This dense irregular connective tissue surrounds all muscles and organs, forms a continuous structure passing through tissues and connects them [146]. Moreover it helps to transmit forces among muscles referred to as epimuscular myofascial force transmission (EMFT) [74].

Several forms of manual therapy techniques have been achieved including classical massage, friction massage, acupressure, trigger point therapy and ischemic compression as well as instrument-assisted soft tissue mobilization techniques (e.g. Graston Technique [69]. They mostly focus on fascia to change its stiffness and arrangement. Previous studies point that after therapy proliferation and activation of fibroblast increases in a way to reproduce extracellular matrix including collagen, elastin, cytokines, and growth factors [147]. It is stated that excessive external mechanical load (e.g. caused by an injury) has pro-inflammatory effect on fascia whereas reasonable size of external load has anti-inflammatory effect [148]. Therefore, the level of external mechanical loading and its duration has key importance which manual therapists need to take into account. However, local effects of external mechanical load were not assessed *in vivo* and no scientific basis has been established towards the effects of manual therapy on tissue deformations.

The purpose of the present work is to examine the local deformations within tissues caused by external mechanical loading simulating ischemic compression in order to relate the deformations with the mechanical load applied. It is hypothesized that external mechanical loading on human lower leg muscles causes sizable and heterogeneous deformations.

In the present study, it is aimed to show the effects of external mechanical loading simulating ischemic compression on human lower leg muscles, *in vivo* using magnetic resonance imaging (MRI) techniques.

6.2 Methods

6.2.1 Experimental Procedures

6.2.1.1 Subjects. Experimental procedures were in strict agreement with guidelines and regulations concerning human welfare and experimentation set forth by Turkish law, and approved by a Committee on Ethics of Human Experimentation at Istanbul University, Istanbul School of Medicine, Istanbul. Five healthy subjects (mean ± SD: age = 27 ± 3 years, height = 175 ± 7 cm and body mass = 73 ± 8 kg) volunteered for this study. In order to minimize anthropometric differences between subjects (Table 6.1), only males were recruited. After a full explanation of the purpose and methodology of the experiments, the subjects provided an informed consent.

Table 6.1
Anthropometric data

Subject	**Age**	**Height (cm)**	**Mass (kg)**	**Upper leg length (cm)**	**Lower leg length (cm)**
A	29	178	85	41	31
B	31	188	73	46	41
C	23	173	72	41	39
D	25	170	70	45	40
E	30	172	78	42	38

6.2.1.2 Experimental Protocol. Each subject was positioned prone within the MRI scanner. The left leg was brought to a reference position before the patient table (a motorized and computer-controlled slide) was moved into the MRI bore: (I) the ankle angle was fixed at 90° (Fig. 6.1) by using an MRI compatible ankle-foot orthosis

(brace on the lower leg and the foot allowing fixation of the ankle angle). (II) To keep orientation of the lower leg constant, the position of the knee cap and the tip of the ankle-foot orthosis were marked on the patient table. (III) The knee angle in this position (*undeformed state*) was (mean ± SD) 173 ° ± 3 °. Based on e.g., [101], knee joint angle was measured using a universal goniometer with its center positioned over the lateral epicondyle of the femur and its arms aligned with the femur and tibia. After moving the patient table into the bore, sets of 3D high-resolution MR images were acquired in the undeformed state. Subsequently, the patient table was moved out of the bore and conditions representative of mechanical loading were created: a rigid cylindrical indenter (diameter=2.5 cm) was pressed against the posterior lower leg by fixing the indenter between the posterior lower leg and ankle-foot orthosis (mean ± SD indentation=6.52 ± 1.24 mm). This causes application of forces normal to m. gastrocnemius, which loads predominantly the muscle's lateral head (Fig. 6.2a). Care was taken to maintain the positions of the knee cap and the tip of the ankle-foot orthosis. Subsequently, the patient table was moved back into the bore automatically ensuring that it attains the identical position as during image acquisition. Second MR image set was collected in this deformed state. Subjects were asked to remain completely relaxed throughout the experiment.

6.2.1.3 Image Acquisition. 3D localizer imaging was performed to plan the subsequent imaging sequences. 3D turbo fast low-angle shot [Turbo Flash] based coronal MR image sets were collected using 3T MR scanner (Magnetom Trio; Siemens, Erlangen, Germany) with 6-channel surface cardiac array coil. The following parameters were used in the Flash sequence: TR = 2000 ms, TE = 3.94 ms, TI = 1100 ms, no fat suppression, flip angle = 12 °, bandwidth = 130 Hz/pixel, number of averages = 1, field of view = 256x256 mm, slice thickness = 0.8 mm (distance factor = 50 %), image matrix size = 320x320x144, voxel size = 0.8x0.8x0.8 mm. Choices of high bandwidth (41600 Hz) and frequency encoding in proximo-distal direction [102] allowed minimizing potential chemical shift artifacts. Imaging time equaled 6 minutes and 50 seconds.

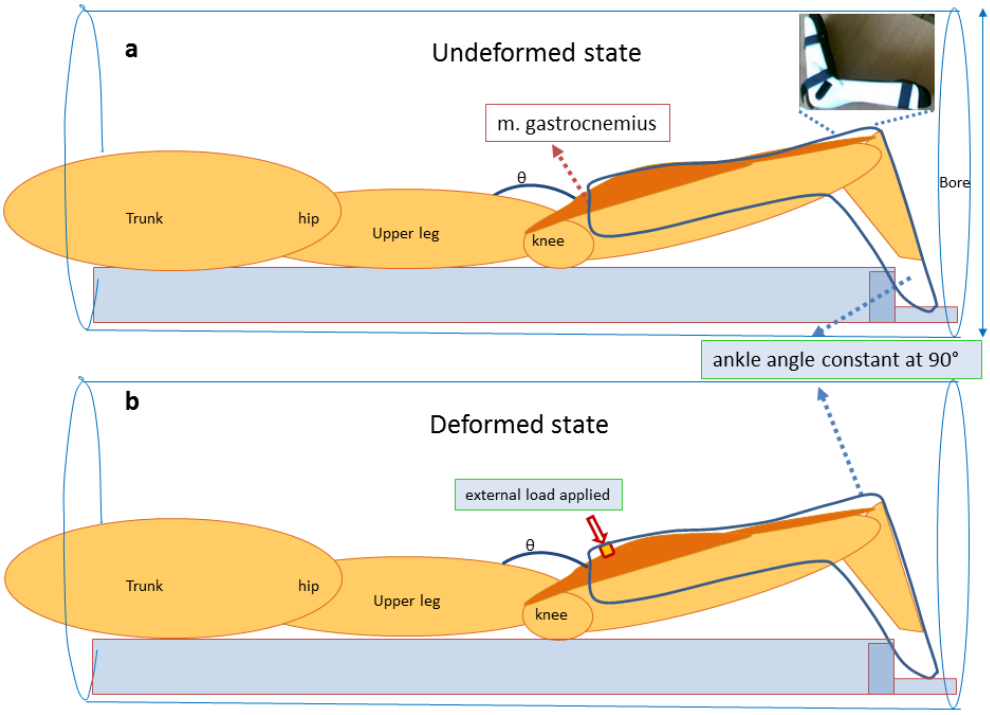

Figure 6.1 Schematic of the leg and trunk within the MRI instrument. (a) Undeformed state. The body is prone on a table (solid line) that is can be moved in and out of the bore of the MRI machine. MRI compatible ankle-foot orthosis (see inset for a picture) was used to fix the ankle angle at 90 °, in such a way to leave a small space between posterior side of the lower leg and the ankle-foot orthosis and also between anterior side of the lower leg and MR patient table to avoid exertion of other external forces. The ankle-foot orthosis was secured onto the patient table using support material. The tips of the toes were not allowed to contact the bore of the MRI machine in order to prevent the foot from being loaded mechanically. (b) The deformed state. A rigid cylindrical indenter (diameter = 2.5 cm) was pressed against the posterior lower leg as the whole body was kept in the same position as in undeformed state.

6.2.1.4 EMG Assessment of Subject Relaxed State. In order to confirm the subject's relaxed state during the experiments, an EMG test was performed (n = 1). Pre-amplified bi-polar surface EMG (Delsys, Trigno Wireless, Boston, MA, USA) was used. Electrodes were located over mid muscle belly of m. gastrocnemius and m. tibialis anterior. This showed that in the final isometric states, EMG activity was very low for both muscles: root mean square values of full wave rectified low pass filtered EMG data normalized for subject's EMG during maximal voluntary contraction (MVC) was less than 0.5 % of the respective MVC value.

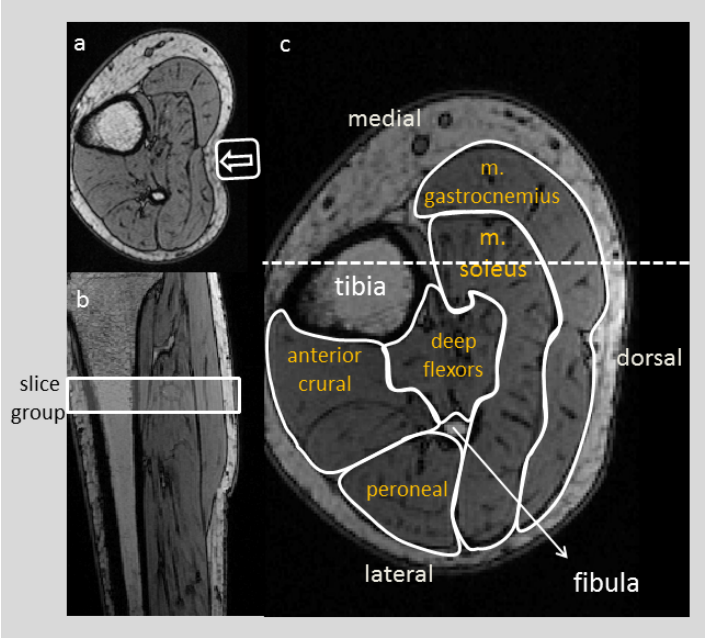

Figure 6.2 Examples of MR images of the lower leg. (a) Mechanical loading. The lower leg was loaded by pressing a cylindrical indenter (a box containing arrow in the image) against the posterior leg. The cross-sectional image shows deformed contours of the calf region, but also deformation of other regions can be seen. (b) Longitudinal image of the lower leg representing a sagittal slice illustrating the locations of the group of cross-sectional slices (white solid rectangle) to be analyzed for strains. For all subjects, the most proximal cross-sectional slice of the slice group was located at the upper third of the imaged portion of the lower leg, a level corresponding to the mid-belly of m. gastrocnemius. (c) An example of a cross-sectional image of the slice group with anatomical identification of muscles or muscle groups and bones (tibia and fibula). Five anatomical regions of interest were distinguished: m. gastrocnemius, m. soleus, deep flexor muscles, peroneal muscles and anterior crural muscles. The dashed horizontal line indicates the location of sagittal image shown in (b).

6.2.2 Calculation of *in vivo* Strains and Volume Changes

A slice group consisting of 30 consecutive cross-sectional slices embracing the region pressed by the indenter was selected manually for each subject (Fig. 6.2b): the most proximal slice location was at the proximal third of the length of imaged portion of the lower leg (corresponding to mid-m. gastrocnemius belly).

Within each slice analyzed, five anatomical regions representing m. gastrocnemius, m. soleus, deep flexor muscles, peroneal muscles and anterior crural muscles were distinguished manually by outlining their boundaries (Fig. 6.2c).

Deformations caused by mechanical loading i.e., *in vivo* strains and *volume*

changes were calculated. In order to do that, MR images acquired in the deformed and undeformed states were aligned. Demons algorithm [41] i.e., a nonrigid and non-parametric image analysis technique was applied. Utilizing arrays of voxel grayscale values, this algorithm relies on (i) *gradients of images* and (ii) *differences between images* i.e., i.e., differences between voxel grayscale values of consecutive voxels within each image and corresponding voxels in deformed and undeformed images, respectively. Image differences calculated iteratively are used to characterize displacement values for each voxel. During each iteration, updated displacement fields are smoothed by a Gaussian kernel for regularization of local displacements and global motion. Finally, after a successful alignment of images obtained by minimizing image differences, information on real deformation is available for each cubic shape comprised of four adjacent image voxels.

Using displacement fields obtained, deformation gradient matrix F, characterizing voxel deformation, was calculated by using displacement gradient (∇u) in material coordinates:

$$F = \nabla u + I \tag{6.1}$$

Green-Lagrange strain tensor E was calculated for each voxel in order to assess deformations within the lower leg muscles present after changing the knee and hip angles:

$$E = \frac{1}{2}\left[F^T F - I\right] \tag{6.2}$$

For each anatomical region separately, the principal strains (means ± SE) and their orientations (i.e. angle between principal direction and the direction of mechanical loading in anterior-posterior direction normal to m. gastrocnemius) were calculated. First (E_1) and third (E_3) principal strains are considered to represent maximal tissue lengthening and shortening respectively. Second principal strains (E_2), characterizing relatively smaller length changes, were not included in the analysis. Only the orienta-

tion of maximal tissue lengthening is included in the analysis.

In addition, heterogeneity of deformation was analyzed within anatomical regions distinguished.

For each voxel with undeformed and deformed volume represented by a^3 and $(a+E_1)(a+E_2)(a+E_3)$ respectively, volume changes (ΔV) were calculated as:

$$\Delta V = (a+E_1)(a+E_2)(a+E_3) - a^3 \tag{6.3}$$

The method was tested previously in section 5.2.6 against subject motion or subject-repositioning.

6.2.3 Distinguishing *in vivo* Deformations from Artifacts Statistically

Principal strain distributions by definition deviate from normal distributions. Therefore, for each anatomical region separately, nonparametric Wilcoxon rank sum tests were performed to test for differences between (i) *in vivo* strains and strain artifacts, and (ii) magnitude of *in vivo* volume changes and volume artifacts. The level of significance was chosen at $p < 0.05$.

6.3 Results

6.3.1 *in vivo* Strains and Volume Changes

After application of external load, mean peak tissue strains were significantly higher than strain artifacts (Table 6.2). Experimental tissue volume changes were significantly different from volume artifacts (Table 6.3).

Table 6.2
Strain errors and principal strains in the deformed state due to mechanical loading

Mean ± SE	m. gastrocnemius	m. soleus	deep flexors	peronei	anterior crural
Strain errors (type A) (synthetic rigid body motion) (n=5)					
Strain error	0.009	0.011	0.012	0.024	0.016
(lengthening)	± 0.001	± 0.002	± 0.002	± 0.004	± 0.002
Strain error	-0.009	-0.011	-0.011	-0.020	-0.013
(shortening)	± 0.001	± 0.002	± 0.002	± 0.003	± 0.001
Local principal strains due to mechanical loading (n=5)					
First principal	0.220	0.143	0.081	0.040	0.050
strain (lengthening)	± 0.049*	± 0.032*	± 0.026*	± 0.020*	± 0.017*
Third principal	-0.114	-0.124	-0.105	-0.116	-0.105
strain (shortening)	± 0.015*	± 0.038*	± 0.046*	± 0.044*	± 0.039*

* indicates significant differences with the strain error.

Fig. 6.3 shows a typical example of a comparison of grids mapped on the most proximal slice of a sample in the undeformed state (left top) and in the deformed state (right top) for subject A. Hardly any deformations are calculated for bony tissues. Substantial tissue deformations are seen within both heads of m. gastrocnemius. However, despite an absence of any global length changes since they do not cross the knee joint, deformation is seen in m. soleus and synergistic deep flexor muscles also, as well as in antagonistic peroneal and anterior crural muscle groups.

Principal strains (mean ± SE) for each anatomical region are listed (Table 6.2). Significant differences between experimental mean principal strains and error strains indicate that deformation illustrated in Fig. 6.3 are common for all subjects and are therefore typical. Experimental tissue volume changes are significantly different from volume errors (Table 6.3) for all muscles.

Experimentally found results for local deformations are shown in Fig. 6.4. Interquartile range (IQR) values indicate heterogeneity of local deformations. Details of local deformation data are provided below:

Table 6.3
Volume errors and tissue volume changes in the deformed state due to mechanical loading

Mean ± SE	m. gastrocnemius	m. soleus	deep flexors	peronei	anterior crural
Volume errors (type A) (synthetic rigid body motion) (n=5)					
Volume error	0.0003	0.0006	0.0016	0.0034	0.0020
	± 0.0004	± 0.0005	± 0.0005	± 0.0014	± 0.0019
Tissue volume changes due to mechanical loading (n=5)					
Tissue	0.0853	0.0088	-0.0360	-0.0915	-0.0622
volume change	± 0.0576*	± 0.0722*	± 0.0576*	± 0.0437*	± 0.0430*

* indicates significant differences with the volume error.

6.3.1.1 m. gastrocnemius. Local deformations are substantial (peak lengthening = 181.50 % and shortening = 33.20 %) and heterogeneous across subjects (IQR values for $E_1 = 0.230$, and for $E_3 = 0.084$). Maximal within subject IQR values equaled 0.376 (subject C) and 0.118 (subject E) for E_1 and E_3, respectively.

6.3.1.2 m. soleus. Peak local lengthening = 185.27 % and shortening = 31.62 % (i.e, approximately 102 % and 95 % of values calculated for m. gastrocnemius). IQR values are for $E_1 = 0.115$, and for $E_3 = 0.064$. Maximal within subject IQR values equaled 0.152 (subject C) and 0.081 (subject C) for E_1 and E_3, respectively.

6.3.1.3 Deep flexor muscles. Peak local lengthening = 25.67 % and shortening = 33.72 % (i.e, approximately 14 % and 102 % of values calculated for m. gastrocnemius). IQR values are for $E_1 = 0.044$, and for $E_3 = 0.032$. Maximal within subject IQR values equaled 0.066 (subject A) and 0.041 (subject A) for E_1 and E_3, respectively.

6.3.1.4 Anterior crural muscles. Peak local lengthening = 18.73 % and shortening = 37.13 % (i.e, approximately 10 % and 112 % of values calculated for m. gastrocnemius). IQR values are for $E_1 = 0.027$, and for $E_3 = 0.071$. Maximal within subject IQR values equaled 0.042 (subject A) and 0.183 (subject E) for E_1 and E_3,

respectively.

6.3.1.5 Peroneal muscles. Peak local lengthening = 15.45 % and shortening = 34.40 % (i.e, approximately 9 % and 104 % of values calculated for m. gastrocnemius). IQR values are for $E_1 = 0.023$, and for $E_3 = 0.074$. Maximal within subject IQR values equaled 0.037 (subject A) and 0.171 (subject D) for E_1 and E_3, respectively.

6.3.1.6 Strain-direction relation. For each subject separately, Fig. 6.5 and Fig. 6.6 show the relation between the size and orientation of lengthening and shortening, respectively along the direction of mechanical loading (big scatter plots) regardless of the muscle groups: High lengthening mostly occurs in small deviations from direction of loading whereas smaller lengthening can occur in any direction. This relation can be highly pronounced for subjects A, C, and E. Among subjects, the relation between the size of shortening and direction varies more: For subjects A, B, and E high shortening mostly occur in small deviations from direction of loading whereas for subject C there is no clear relation and for subject D the relation is opposite. Small shortening can occur in any direction.

6.3.1.7 Strain-distance relation. Distance was measured per voxel in muscles as the radial distance between it and the closest voxel to the indentation in m. gastrocnemius. Voxels in tibia, fibula, and the skin are not included in these plots. The lengthening values spread radially through calf muscles and even into deep flexors (see insets in Fig. 6.5). Highest lengthening occurred in parts of calf muscles which are closely in the neighborhood of the indenter. Local lengthening decreases gradually as the distance to the indenter increases. This relation can be highly pronounced for subjects A, C, and E. However, this relation is less clear for shortening (see insets in Fig. 6.6): Shortening values spread radially as in lengthening for subjects A, B, and D whereas for subject C the relation is opposite. There is no clear relation for subject E.

In summary, mechanical loading will cause substantial local strains within (i) gastrocnemius immediately within the treatment vicinity, (ii) synergistic, (iii) as well as antagonistic muscles of gastrocnemius within the lower leg. Note that local lengthening effects of such loading are profound in the directly targeted m. gastrocnemius and drop at least by half at more distant locations, but remain sizable nevertheless. In contrast, the reduction in the local shortening effect remains rather limited at larger distances throughout the lower leg cross-section. Mechanical loading causes highly heterogeneous length changes for the tissues closely in the neighborhood of the indenter but length changes are less heterogeneous for the tissues more distant to the location of the indenter. The inter-subject variability in local lengthening indicates that for different subjects similar mechanical load causes different size of deformations.

6.4 Discussion

6.4.1 Intensity Based Non-Rigid Registration as a Tool to Quantify Tissue Deformation Caused by Mechanical Loading

Our main goal was to quantify tissue deformations within human lower leg, *in vivo* caused by mechanical loading. This loading simulates the ischemic compression type manual therapy technique. Such techniques focus on changing the mechanical properties of connective tissues -mainly fascia- by simply stretching or compression. Previously the effects of such manual therapies have been investigated clinically by palpation and statistical analyses of the patient responses [149, 150, 151]. Additionally mathematical analyses were performed to quantify the effects of manual therapy: (I) Viscoelastic behavior of stretched human fascia during the therapy was studied to predict the stress for certain deformation [152]. (II) Three-dimensional mathematical model was developed in order to relate applied mechanical forces and deformation of fasciae during manual therapy [153]. (III) Mathematical analysis was performed in order to determine the mechanical load over a specific duration to produce a determined amount of stretch in biceps muscles during manual therapy [154]. (IV) Animal experiments were performed in order to show the effects of cross-fiber massage on knee

ligament healing [155]. These clinical studies and mathematical models are useful in order to show the effects of manual therapies clinically and theoretically. However they are unable to provide *in vivo* data to show the effects of manual therapies. Ceelen et al. [152] used MR Tagging *in vivo* to validate a finite element model in order to predict strains causing pressure ulcer. They applied mechanical loading using an indenter as in the present study, however performed the analysis only on 2D images and the strain resolution was lower than the present study because of high tagging grid line spacing (3.3 mm). By analyzing high resolution 3D MR images, our method was used successfully in previous studies to assess the effects of epimuscular myofascial force transmission between m. gastrocnemius and (i) synergistic m. soleus [104] and (ii) synergistic deep flexors and antagonistic peroneal and anterior crural muscles [133]. We therefore conclude that present method provides more detailed data compared to other methods in order to show the effects of manual therapy techniques.

Note also that present approach allows quantification of volume changes in muscle groups. Volume changes calculated presently were marginal for all muscle groups. However, during mechanical loading, certain notable volume changes that may occur within parts of the limb are physiological, as altered intramuscular pressure may cause changes in arterial flow and venous expulsion [118, 119, 120]. Our present results show that, after mechanical loading, effects were sizable, causing an increase in volumes of m. gastrocnemius and its synergistic m. soleus, and a drop in volumes of deep flexors and antagonistic peroneal and anterior crural muscles. This suggests that mechanical loading imposed on m. gastrocnemius causes considerable blood expulsion from the deep veins (peroneal vein, anterior tibial vein and posterior tibial vein). Therefore, additional to effects on muscle mechanics, quantification of local tissue volume changes may help improving our understanding of such hemodynamics in healthy subjects and in patients with venous dysfunction.

6.4.2 Effects of Manual Therapy in Cellular Level

Since the proliferation and activation of fibroblast is the key to healing process in connective tissues [147]; studies have been made in order to explore the effect of mechanical loading on fibroblast proliferation [156, 157]. Repetitive strain injuries resulting from exercise or manual labor and myofascial release were modeled *in vitro* by cultured human fibroblasts [158]. The morphological alterations in post repetitive strain were indicated in this model study. Additionally, it was shown that these injuries were reversed when myofascial release were applied. Wang et al. [159] showed that cyclic mechanical stretching of tendon fibroblasts increases the production of prostaglandin E2 and cyclooxygenase. It is hypothesized that repetitive low magnitude of stretching has anti-inflammatory effect whereas large one has pro-inflammatory effect [148].

It is necessary to know the relation between the size of mechanical loading and its effects in order to enhance the results of manual therapy. The stress-strain curve of connective tissues is divided into regions in order to indicate this relation [160]: In *toe* region, despite strains are low, very little stress produces relatively large deformations as the crimping is taken out of the fibrils. In *linear* region as the stress increases there is no crimping left. Elastic deformation occurs within physiological limits. At the end of this region, tissue cannot tolerate the stress anymore and microfailure starts internally: In this *primary failure* region, individual collagen fibers and fiber bundles are broken permanently (plastic deformation). It is followed by a cycle of tissue inflammation, repair, and remodeling which is the desired outcome of manual therapies in order to produce permanent elongation. If the load is increased further, all fibers are broken in *complete failure* region. Note that applying the load causing only microfailure depends on the expertise of the examiners. Therefore, quantification of the relation between the load and the deformation is needed. Kureshi et al. [161] measured the intervals of toe, linear and primary failure regions (13.28 %, 51.43 %, and 61.97 %, respectively) of stress-strain curves from longitudinal and transverse samples of transversalis fascia. This study can be used to match these regions and tissue parts, locally.

The present approach does allow quantifying the effects of mechanical loading

simulating ischemic compression on tissues: Mechanical loading on m. gastrocnemius causes high strains not only within m. gastrocnemius but also its synergistic m. soleus. This deformation gradually decreases through deep flexors, peroneal muscles and anterior crural muscles. The direction of maximal lengthening values may depend on the orientation of the fibers in muscular and nonmuscular tissues. Toyoda et al. [162] and Buckley et al. [163] demonstrated that cells align to the direction of the tensile load by reconstructing their cytoskeleton.

6.4.3 Effects of *in vivo* Myofascial Force Transmission in Human

In previous animal experiments [100, 15], finite element models [98] and *in vivo* human experiments [133] it is showed that epimuscular myofascial force transmission (EMFT) occurs between synergistic as well as antagonistic muscles through perimysium and epimysium, neurovascular tracts, compartmental boundaries and fascia [74, 97]. These nonmuscular tissues create continues connections among muscles which allow EMFT. In the present study, deformations spreading through synergistic and antagonistics of target muscle (m. gastrocnemius) show that EMFT not only occurs during regular human movement but also when manual therapy is applied externally. It is also shown using finite element modeling that EMFT causes highly nonuniform muscle tissue deformation [133, 20, 17]. This explains one of the present findings: the heterogeneity of strains within muscles.

6.4.4 Limitations and Implications of the Present Study

The present method is useful to predict damage as performing ischemic compression. It can be extended to assess the effects of other manual therapy methods. However local strains should not be interpreted quantitatively as information regarding individual muscle and connective tissue fibers lengths. The resolution obtained allows the study of muscles or muscle groups instead of individual muscle and connective tissue fibers.

The present method can only quantify the deformations within the tissues. For each patient, knowing local mechanical properties of tissues would be beneficial in order to predict the deformations before and hence to decide the magnitude of the applied load. Magnetic resonance elastography (MRE) [143, 144] does allow the calculation of local values of shear modulus within human muscles [145]. Recently MRE studies are focused on quantifying the mechanical properties of myofascial taut bands in order to assess the changes resulting from manual therapies [164, 165].

In the present study ischemic compression is simulated on healthy subjects. This type of compression is mostly used on treatment of trigger points. As the projected pain caused by trigger points within gastrocnemius is localized on it as opposed to other muscles (e.g. neck muscles) [166], the present study can be extended to clinical practice to study the relation between pain and mechanical response. In such further study, pain assessment should be done before application by an algometer or a visual analog scale. Those trigger points in calf muscles have clinical importance since (I) they may mimic Achilles tendonitis [167], (II) they are possible contributors to calf cramps [166, 168, 169, 170], (III) Plantar fasciitis (also known as Plantar heel pain) is mostly related to trigger points in the calf muscles and foot musculature [171, 172].

6.5 Conclusions

External mechanical load to simulate ischemic compression imposed on m. gastrocnemius causes sizable and quite heterogeneous local strains to occur, not only within this muscle, but also within synergistic, as well as antagonistic muscles kept at constant muscle-tendon complex length (global isometric condition). Moreover, similar mechanical load can affect the subjects differently.

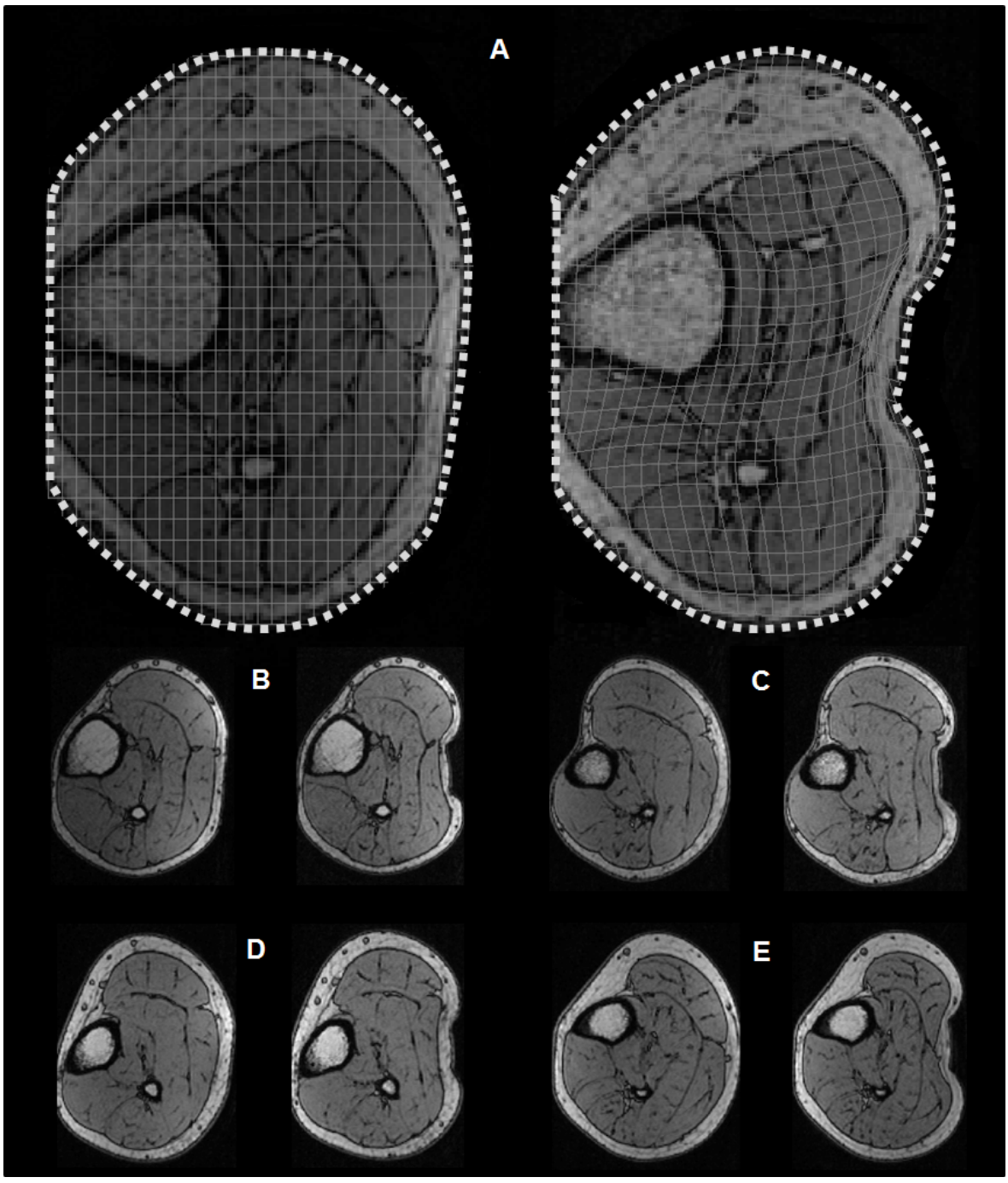

Figure 6.3 A typical example of deformations calculated as caused by mechanical loading. Subject A: A cross-sectional slice acquired in the undeformed state. A regular grid (made up of lines connecting voxel group centers) was imposed on the image at certain pixel intervals (4x6 pixels) for better visualization (top left). The corresponding slice acquired in the deformed state. Using Demons algorithm, displacement fields were calculated. Based on these displacement fields, the regular grid was deformed and imposed on this image (top right). For other subjects (B-E), sample slices at the same proximo-distal level of the center of the indenter were shown without indentation (left) and with indentation (right).

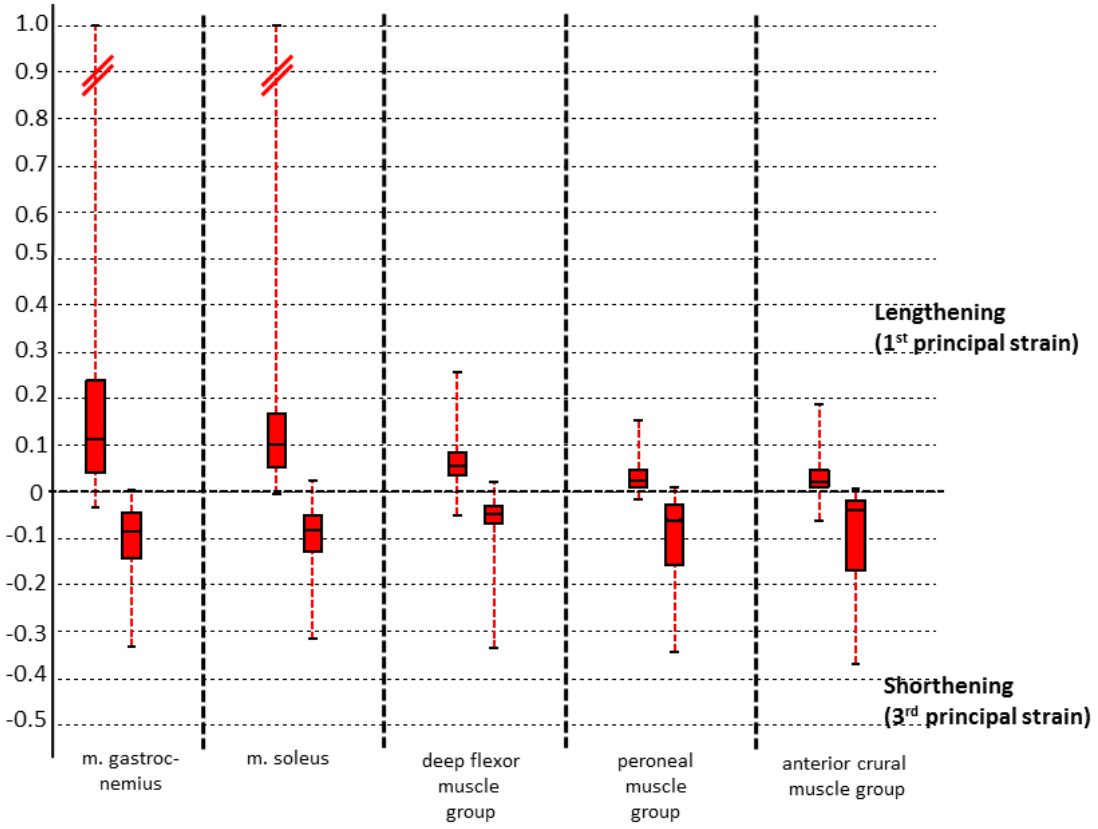

Figure 6.4 Effect of mechanical loading: Local lengthening and shortening effects (first and third principal strain). Box & whisker plots: the horizontal line inside each box represents the median strain value; the upper and lower edges of each box itself represent upper and lower quartiles respectively (i.e., the 75th and 25th percentiles), and lines extending from each end of the box (whiskers) indicate the peak values of the principal strains plotted. Inter-quartile ranges (IQR i.e., absolute value of the difference between upper and lower quartiles) were considered as a measure of strain heterogeneity within each anatomical region. Data were represented per anatomical region of interest (muscle or muscle group) and analyzed across all subjects.

See Fig. C.11 in Appendix C for detailed 3D reconstructions of MRI images showing the deformations in connective tissues within the lower leg.

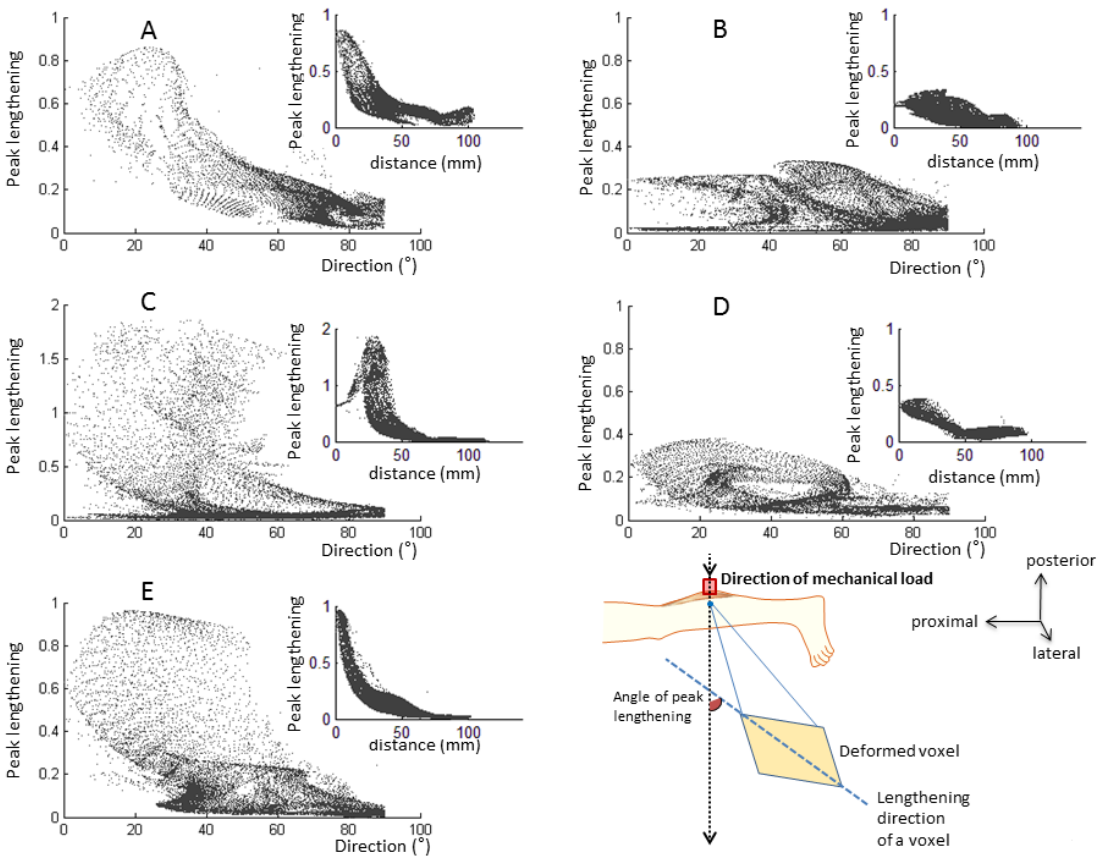

Figure 6.5 Relation between local lengthening, its direction and location. For each subject (A-E), regardless of the muscle groups each graph shows the relations (i) between the size and orientation of lengthening along the direction of mechanical loading (big scatter plot) and (ii) between the size and the distance to the indentation (small scatter plot inset). The angle between peak lengthening and indentation direction is denoted (bottom right).

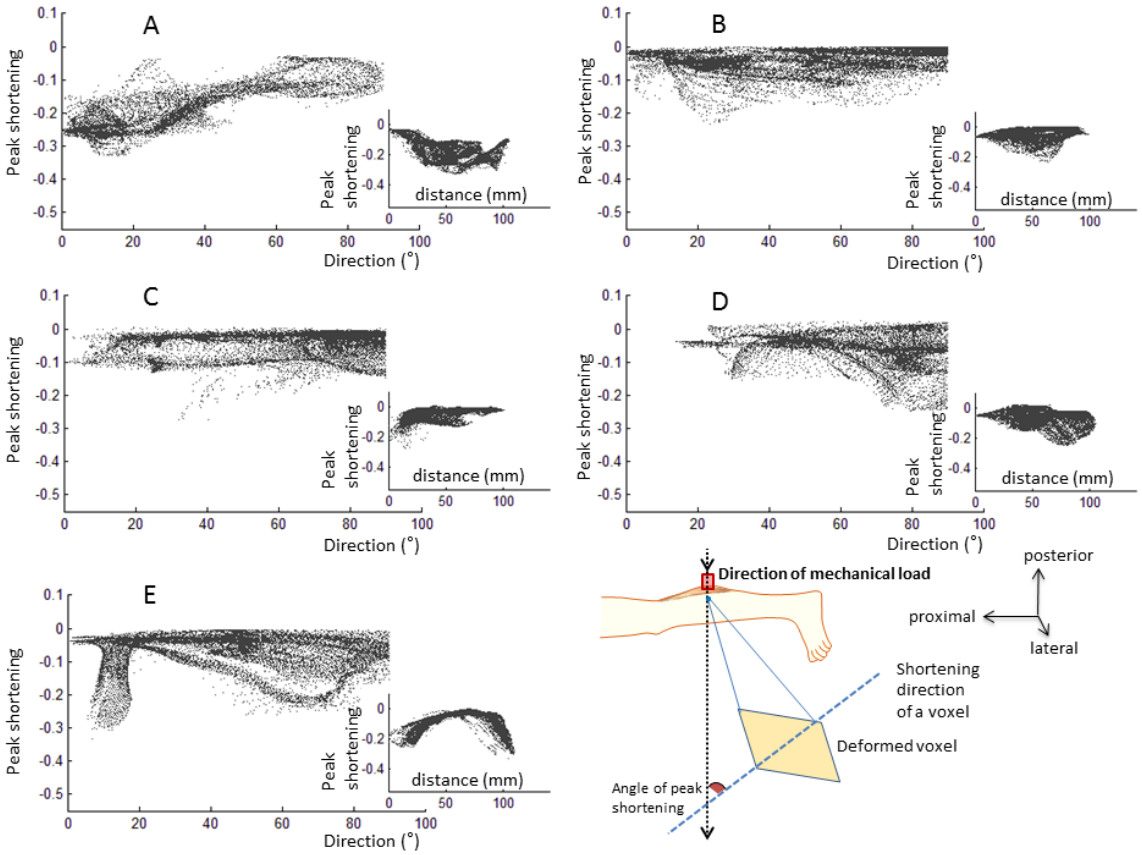

Figure 6.6 Relation between local shortening, its direction and location. For each subject (A-E), regardless of the muscle groups each graph shows the relations (i) between the size and orientation of shortening along the direction of mechanical loading (big scatter plot) and (ii) between the size and the distance to the indentation (small scatter plot inset). The angle between peak shortening and indentation direction are denoted (bottom right).

7. GENERAL DISCUSSION

7.1 Goals and Methods

7.1.1 Magnetic Resonance Imaging and Demons Registration

For centuries *in vitro* studies have been the only way to understand how human body is structured and how it works. Recently it has become possible to create finite element models for this purpose. These models are great tools to extrapolate the results to the conditions which cannot be created *in vitro*. However, the only way to validate these extrapolated results is to use *in vivo* measurement techniques. Another necessity to *in vivo* techniques is about the reliability of measurements. In biomechanics, *in vivo* intervention for measurements (e.g. putting sensors) affects neurovascular connections and muscular activity which may change the results. Studying *in vivo* noninvasively should be our main goal and it reduces the side effects of measurements significantly.

Developments in computing technologies and computers have been facilitated the practical usage of advanced image processing algorithms on data obtained from computerized tomography (CT) and nuclear magnetic resonance. These two *in vivo* techniques could provide detailed volumetric images. In addition, specific MRI techniques has been developed in such a manner that they can be used to quantify stiffness and deformations within soft tissues directly: (i) magnetic resonance elastography (MRE) [143, 144], (ii) tagged magnetic resonance imaging (TMRI) [35], (iii) phase contrast MRI (PCMRI) [36, 37], (iv) pulse field gradient based MRI methods (HARP and DENSE) [39, 38], and (v) strain encoding imaging (SENC) [40]. Moreover, diffusion tensor imaging (DTI) techniques of MRI provide information on tissue structure based on contrast caused by motion of water molecules [43].

7.1.2 Goals of the Study

In this dissertation study high resolution anatomic MR image sets acquired in two different postures and were used in non-rigid non parametric Demons registration algorithm in order to quantify local deformations within muscular tissues. Strain tensors representing deformations were rotated to local fiber directions using diffusion tensors in order to calculate lengthening and shortening in local fiber directions. This combined technique was used to assess (i) the effects of hip and knee angle change on m. gastrocnemius and other synergistic and antagonistic muscles kept isometric within human lower leg and (ii) the effects of external mechanical loading representing ischemic compression technique. Findings were utilized the effects of epimuscular myofascial force transmission (EMFT) in human muscle *in vivo* which were not shown previously in the literature.

7.2 Relevance of the Study

7.2.1 Experimental Conditions

To assess EMFT the length of a muscle should be changed passively whereas other muscles within the same limb are kept isometric. For this reason and because of its simple anatomic structure, lower leg was chosen as our initial target. Narrow bore of MRI scanner limits the movement as lower leg was fixed; only small change in knee angle was possible. Therefore the effects of EMFT were not quantified for full range of motion of m. gastrocnemius. If forearm muscles had been studied, subject positioning would have been easier and more comfortable. In such experiment, elbow and wrist could be fixed so that wrist flexors remain isometric whereas the lengths of digit flexors could be changed in full range by clenching. Note however that forearm muscles have more complex anatomy as compared with lower leg. Moreover given the same image resolution since they are small in size; the proportion of the number of voxels within muscle boundaries to the whole number of voxels within muscle would be

higher than those of lower leg muscles. Therefore smoothing effect of Demons algorithm may dominate and reduces the accuracy of calculations.

7.2.2 Demons Algorithm

As other non-rigid registration techniques Demons algorithm relies on a deformation model utilizing image intensity and contrast. Because of this, if imaged tissues do not have sufficient detail (e.g. as in skin or general fascia) displacements of voxels, hence deformations could not be calculated. Note however details on image can be increased by selecting small field of view and small voxels as acquiring MR image sets but this reduces SNR.

In addition Gaussian smoothing as one of the main steps for regularization of displacements reduces the effective image resolution of displacement data. We believe its effect on adjacent voxels is reduced significantly within a few voxels at the muscle boundaries and muscle volumes are large in human lower leg, so our technique provides adequate resolution and minimal muscle smearing due to algorithm itself.

If periodic motion is provided passively or actively by subject, dynamic MRI techniques (e.g. TMRI, SENC) can be used in future studies. Doing so, strain or deformations are encoded directly on tissues by changing their magnetization properties. Compared to the present method these more direct methods are more convenient to assess small tissues (e.g. fascia, tendons or small muscles as those of forearm) as they do not rely on plain image intensities or smoothing.

The synthetic tests (in chapters 4, 5, 6) are only given that the employed Demons algorithm based registration method could be utilized effectively for these muscle MR datasets (i.e. there are adequate structure and contrast within muscle).

Since the focus of our research team in the future is most likely rely on direct MRI measurement techniques we did not explore fully the limitations and artifacts

of Demons algorithm beyond what was basically requested by the reviewers in these corresponding publications.

If Demons algorithm is utilized further in future studies, detailed synthetic motion performance analysis need to be repeated more exclusively including Monte Carlo tests with various noise levels, and multiple repositionings of the same subject.

7.2.3 Quantifying Mechanical Properties of Tissues Using MRE

Neither present method nor dynamic MRI techniques can provide tissue stress or stiffness. MRE which relies on imaging the propagation of external shear waves is used recently to quantify tissue stiffness [143, 144]. In further studies a combined methodology could be employed to get all three relevant parameter sets: (i) tissue stiffness, (ii) deformations, and (iii) local fiber directions using MRE, one of dynamic MRI techniques, and DTI, respectively. This could be more beneficial to relate the transmitted force and its effects on muscle fibers locally and more directly.

7.2.4 MRI Compatible EMG

In this dissertation, MRI compatible EMG device was not available to us when acquiring most of our imaging data. A pilot EMG study outside of MRI scanner was performed to assess the muscular activity status. Using an MRI compatible EMG device could give more accurate and real-time information about the underlying muscular activity.

7.3 Implications of EMFT

This is the first study that shows the effects of EMFT in human lower leg *in vivo* using peak length changes (principal strains) and length changes in local fiber

directions. The results indicate that muscles are not fully isolated functioning units. It changes the sarcomere length heterogeneity of other muscles within the same limb and hence changes the force-length characteristics.

7.3.1 Proximo-distal Force Difference

In this dissertation the proximo-distal force difference was not shown. In further studies, in addition to single proximal ROI studied, second ROI can be selected in distal in order to assess the effects of proximo-distal force differences by comparing the deformations between two ROIs. For this purpose instead of two ROIs muscle deformations on tendons may give more accurate results. SENC could be more appropriate to quantify strain in tendons rather than the present method since tendons do not have enough details on MR image.

7.3.2 Implications of EMFT in Other Limbs

The effects of EMFT may differ in other skeletal muscles of human body. Forearm muscles are good candidates for further experiments because the similar experimental scenario can be applied as stated in section 7.2.1. These muscles are smaller than those in lower leg and they have more complex inter- and extramuscular connections. Therefore EMFT is expected to be more pronounced. Demands on imaging resolution and challenges due to low SNR should be investigated in detail.

7.3.3 Implications of EMFT in Muscle Treatments

The effects of EMFT may differ in unhealthy subjects: (I) It was shown that EMFT affect the abnormality in spastic muscle mechanics *in vitro* [25, 27]. In order to get local effects of EMFT on spastic muscles can be assessed *in vivo* using the present method. (II) Similarly the effects of BTX-A administration on both injected

spastic muscle and noninjected adjacent muscles were shown *in vitro* [28]. Note that it was shown that BTX-A injection affects EMFT mechanism, as well. In addition to local deformation analysis using the present method, the measurement of diffusion and fractional anisotropy using DTI before and after the injection may indicate how and where these effects become pronounced. (III) The outcome of tendon transfer surgeries was studied *in vivo* using Cine-PC MRI [21, 22]. However these studies should be assessed within the perspective of EMFT.

7.4 Implications in Manual Therapies

In our preliminary manual therapy study (chapter 6) experimental procedure may not ideally reflect the manual therapies applied by physiotherapists. In accordance with clinical procedures a few points should be taken into consideration in further studies: (I) The format of the application of external loading (e.g. size, duration, period) should be redesigned. (II) Back and neck parts of human body should be studied as well since these parts are the main focus of manual therapy. (III) Experiments should be made on unhealthy subjects as well as healthy subjects since the effects of manual therapy may differ. (IV) Manual therapies mainly focus on connective tissues rather than muscles. Therefore imaging method should be retuned to get more detailed data from connective tissues. (V) The present method can be used to assess not only the effects of external mechanical loading but also those of other manual therapies. Such as in kinesiotaping once elastic therapeutic tape (i.e. elastic cotton strip with an acrylic adhesive referred also as kinesio tape) is applied it creates a pulling force on the skin. It is claimed that the application of kinesio tape aligns the fascia, facilitates joint motion, and increase blood flow and circulation of lymphatic fluids by lifting the skin and increasing the space below [173]. Note that these effects are still unclear and they should be assessed *in vivo* in further studies: (I) Alignment of fascia and changes in the space below the skin can be quantified by the analysis of local deformations using MRI *in vivo*. (II) The perfusion (i.e. increase in blood flow) can be analyzed using MR perfusion imaging *in vivo*.

APPENDIX A. DEFORMATION ANALYSIS AND STRAIN CALCULATION

In this appendix the steps of Demons algorithm are described. Demons algorithm relies on gradients of images and differences between images that are used in Demons equation (A.1) to get displacement vectors per pixel or voxel. For simplicity, the steps of deformation analysis is shown for 2D images. There is only two images: image1 and image 2 (Fig. A.1).

A.1 Difference Image

Each square represents a pixel and has value between 0 and 255 (i.e., grayscale) in image 1 and image 2 (Fig. A.1). 0 and 255 refer to black and white, respectively. Any value in this range is a tone of gray. The difference image is the difference of each corresponding pixel values in image 1 and image 2. (e.g., the value of the pixel "a" in difference image = the value of "a" in image 1 - the value of "a" in image 2 = 180-110 = 70, the value of the pixel "e" in difference image = the value of "e" in image 1 - the value of "e" in image 2= 130-105 = 25, etc.). These values are normalized in the figure of "difference image" to show the differences in values.

Note the dissimilarity in calculation of gradient images and difference image: (i) gradients of an image are calculated by the differences of the neighboring pixels within an image whereas, (ii) the difference image is calculated by the difference in corresponding pixels in image 1 and image 2.

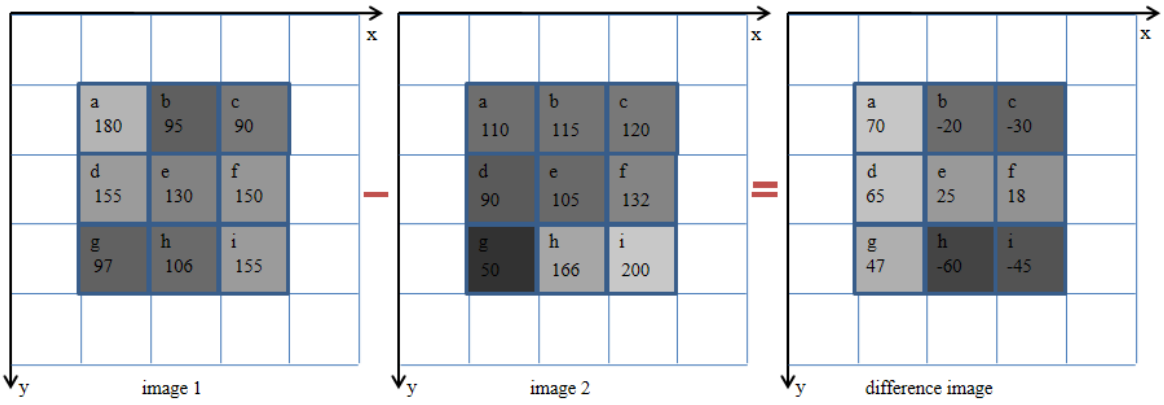

Figure A.1 Difference Image. Each corresponding pixels in image 1 and image 2 are subtracted.

A.2 Gradients of Image

Gradients of image 1 are shown in Fig. A.2. The difference between neighboring pixel values in x-direction is calculated to obtain the gradient of the image in x-direction. (e.g., the gradient value of the pixel "a" = the value of "b" - the value of "a" = 95-180 = -85, the gradient value of the pixel "d" = the value of "e" - the value of "d" = 130-155 = -25, etc.). The difference between neighboring pixel values in y-direction is calculated to get gradient of the image in y-direction (e.g., the gradient value of the pixel "a" = the value of "d" - the value of "a" = 155-180 = -25, the gradient value of the pixel "b" = the value of "e" - the value of "b" = 130-95 = 35, etc.). Gradients of image 2 are calculated, as well.

A.3 Demons Algorithm Formulation

The formulation of the Demon's algorithm is below. Note that the gradients and difference image are used to calculate displacement (u) of each pixel at each iteration. "u" can be considered also as a measure of dissimilarities between image 1 and image 2. In each iteration, it is tried to decrease the dissimilarity and "total displacement of each pixel" is updated by "u".

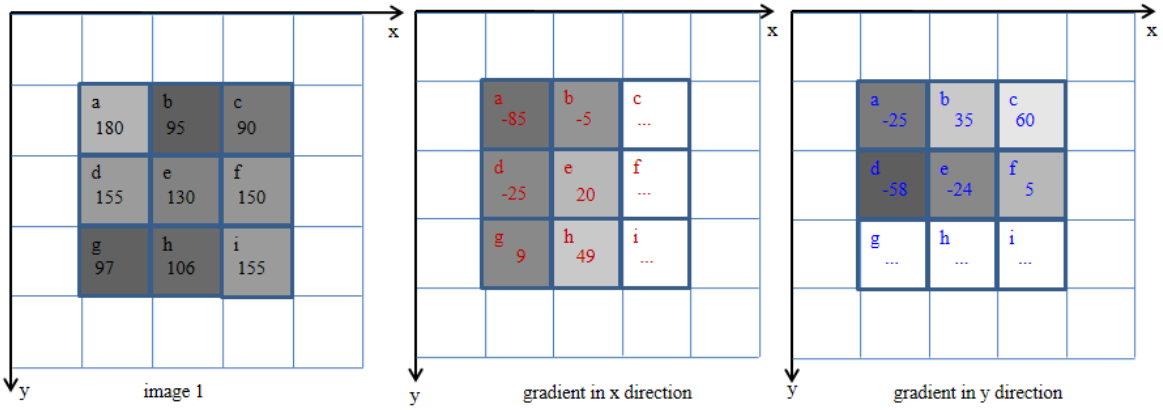

Figure A.2 Gradients of Image. For image 1 neighboring pixel values are subtracted in x- and y-directions to obtain the gradient images in x- and y- directions, respectively.

Keep in mind that after each iteration, image 1 is constructed again according to the displacement values and then new "u" is calculated accordingly. After the total difference between images becomes smaller than a threshold value prescribed, the algorithm stops, and the last updated value of total displacement gives us the displacement value of each pixel.

$$\vec{u} = (m - s) \times \left(\frac{\vec{\nabla} s}{\left|\vec{\nabla} s\right|^2 + \alpha^2 (m - s)^2} + \frac{\vec{\nabla} m}{\left|\vec{\nabla} m\right|^2 + \alpha^2 (s - m)^2} \right) \tag{A.1}$$

For each pixel:

- u: displacement vector containing displacements in x- and y- direction
- m: value of the pixel in image 1
- s: value of the pixel in image 2
- ∇s: gradient value of the pixel in image 2
- ∇m: gradient value of the pixel in image 1

- α: positive weighting factor to avoid instabilities in the algorithm for small image gradient values

For pixel "a": (m-s) = 70, ∇sx=5, ∇sy=-10, ∇mx=-15, ∇my=-5. If we take α=1, then displacement in x- direction will be -0.40 and displacement in y- direction will be -0.71 for the first iteration.

A.4 Regularization of Displacement Values

Fig A.3. denotes how displacement values are smoothed (i.e. regularized). The displacement values (u) in y direction for a small part (5x5 pixel) of the image is shown in the figure (left). Displacement fields are regularized in each iteration (i) to handle large motions well and (ii) to decrease oscillations in local displacement values to make sure that displacements are consistent with viscoelastic behavior of the tissues (i.e. to preserve the geometric continuity of the tissues).

Weights of the Gaussian kernel (size=5, standard deviation=2) are calculated (middle) for smoothing by the formula:

$$G(x,y) = \frac{1}{2\pi\sigma^2} e^{-} \frac{x^2+y^2}{2\sigma^2} \tag{A.2}$$

Resulting smoothed displacement field for all pixels in y direction by Gaussian kernel is shown in the figure (right). The color values are normalized in the figures to show the differences in values. The calculations for smoothed value of pixel "a":

- The original value of the displacement of pixel "a" = 0.111.
- In 5x5 window (i.e. the light green rectangle), whole pixels will be used:
- Smoothed value of "a" = -0.156x0.023 - 0.091x0.034 + ... + 0.068x0.023 = 0.025.

Note that when calculating smoothed value of another pixel (Say, "b"), Gaussian weights will be same for the same Gaussian kernel, but the pixels used will be within the dark green rectangle (not the light one).

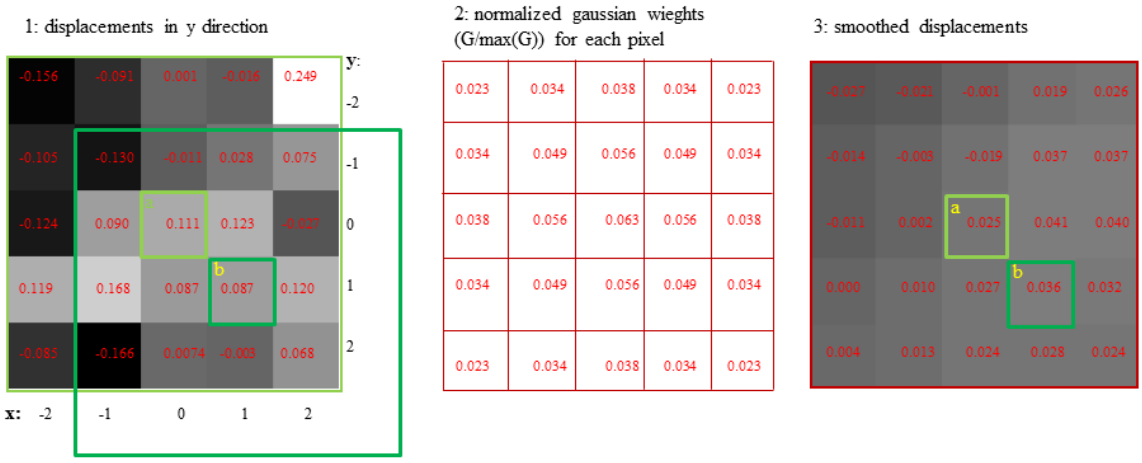

Figure A.3 Regularization of Displacement Values

Regularized displacement values are shown in Fig. A.4. The displacement values (u) for a small part (5x5 pixel) of the image is shown in the figure.

- (1) raw displacement field in x direction
- (2) smoothed displacement field in x direction
- (3) raw displacement field in y direction
- (4) smoothed displacement field in y direction

These values are normalized in the figures to show the differences in values. Pixel values show how Gaussian smoothing (size=60, standard deviation=10) regularizes the displacements at each iteration.

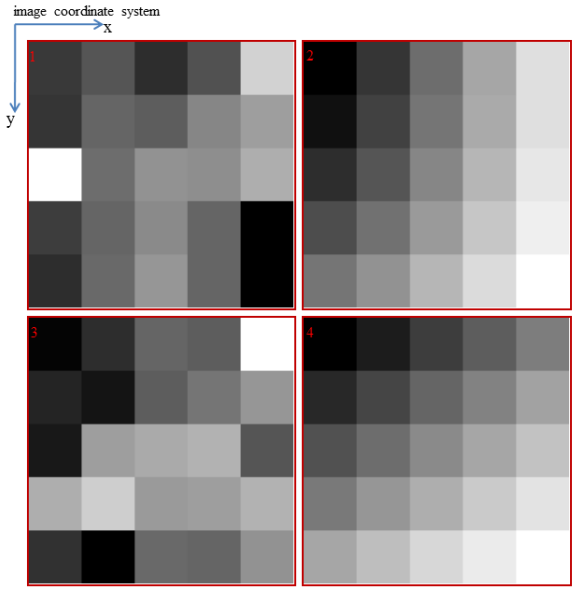

Figure A.4 Regularization of Displacement Values

A.5 Obtaining the Deformation Gradient Matrix

Example of the calculation of one strain value between neighboring pixels is given in Fig. A.5. Consider that the red circles (A,B,C,D) are centers of the 4 neighboring pixels and the big blue circle is the center of the square (ABCD) in image 1 (left). In image 2 (right), the square (ABCD) is deformed according to the displacements of the four points (i.e. A,B,C,D). Note that these displacement values were those calculated by Demons algorithm.

1.2 and 0.5 are the new lengths in x and y axes, respectively. 0.3 and 0.4 are the shear values. Using these four values we can set "deformation gradient matrix":

$$f = \begin{bmatrix} 1.2 & 0.4 \\ 0.3 & 0.5 \end{bmatrix}$$

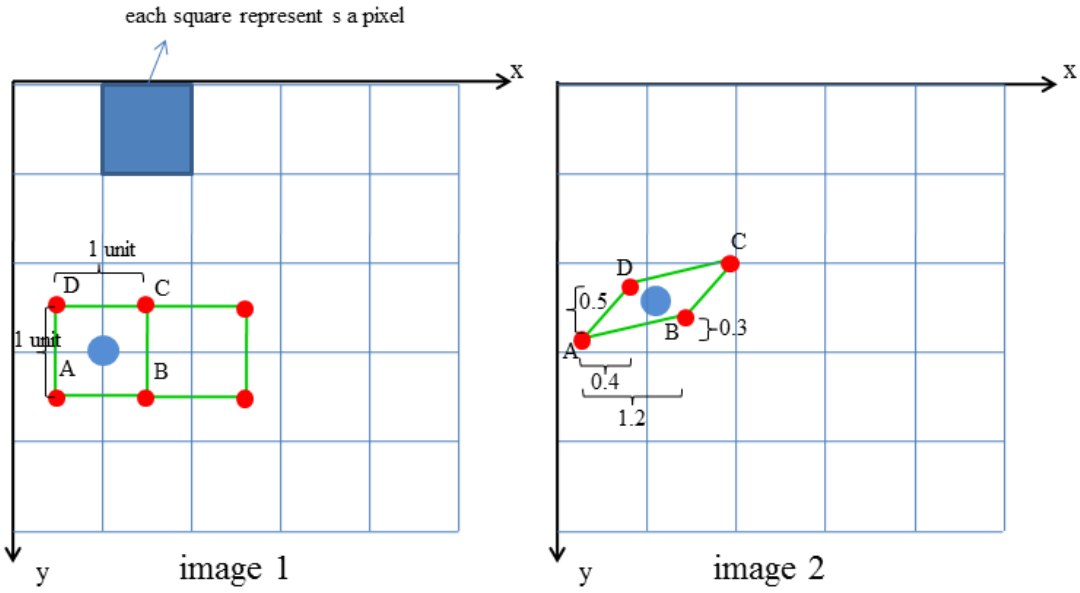

Figure A.5 Obtaining the Deformation Gradient Matrix

A.6 Calculation of the Strain Tensor

The relation between deformation gradient matrix (f) and the strain matrix (e) is described with this equation:

$$e = \frac{1}{2}\left(f^T f - I\right) \tag{A.3}$$

I is identity matrix:

$$I = \begin{bmatrix} 1 & 0 \\ 0 & 1 \end{bmatrix} \tag{A.4}$$

Using this formula, strain matrix is calculated:

$$e = \begin{bmatrix} 0.27 & 0.32 \\ 0.32 & -0.30 \end{bmatrix}$$

The diagonal elements (i.e. 0.27 and -0.30) are normal strains and 0.28 is the shear strain. If we calculate the diagonal matrix (d) of the eigenvalues of the strain matrix, the shear elements vanish and the remaining principal strains give the maximum lengthening and shortening, respectively: 0.41 and -0.44.

$$d = \begin{bmatrix} -0.44 & 0.00 \\ 0.00 & 0.41 \end{bmatrix}$$

These maximum lengthening and shortening are represented by purple dashed lines perpendicular to each other (Fig. A.6).

Note that the strain between neighboring pixels are calculated. Both image 1 and image 2 have 256 pixel width and 256 pixel height. Thus, we have 255x255 strain values. In our actual 3D case, we calculate the strains between neighboring voxels.

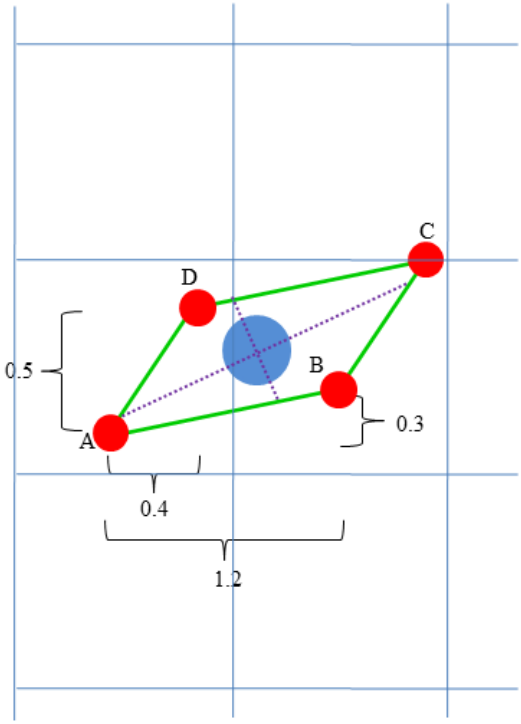

Figure A.6 Calculation of the Strain Tensor

A.7 Volume Change

V_0 = Initial volume = a^3

V = Final volume = $a^3(\epsilon_{11}+1)(\epsilon_{22}+1)(\epsilon_{33}+1)$

Shear does not affect the volume. ΔV = Volume change = $V - V_0 = \epsilon_{11} + \epsilon_{22} + \epsilon_{33} + \epsilon_{11}\epsilon_{22} + \epsilon_{11}\epsilon_{33} + \epsilon_{22}\epsilon_{33} + \epsilon_{11}\epsilon_{22}\epsilon_{33})$

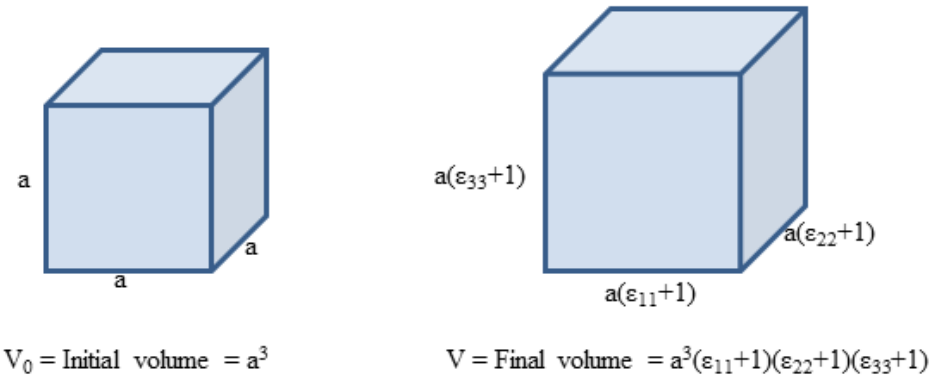

Figure A.7 Calculation of the Volume Change

APPENDIX B. ROTATION OF STRAIN INTO LOCAL FIBER DIRECTIONS

Anatomical Turbo Flash and DTI sequences are acquired consecutively in both undeformed and deformed states with the help of the same localizer. Therefore their dicom images have the same coordinate system. Their acquisition times are short and the leg is fixed carefully.

A dicom file contains a header part which provides various parameters about the image and the acquisition. Some of these parameters help to relate 2D dicom image coordinates with 3D patient coordinates (i.e. physical coordinate system). The origin of the patient coordinates is arbitrary but fixed.

B.1 Dicom Parameters

Fig. B.1 denotes the meaning of dicom parameters used. These parameters are:

- IPP: ImagePositionPatient; patient coordinates of the first pixel in mm
- IOP: ImageOrientationPatient; consisting of two direction cosines indicating orientation of image plane with respect to patient coordinate
- PS: PixelSpacing; height and width of the pixels in mm
- ST: SliceThickness

B.2 Transformation between image and patient coordinates

These parameters are related to voxel orientation and location with respect to patient coordinates as shown in Fig. B.2.

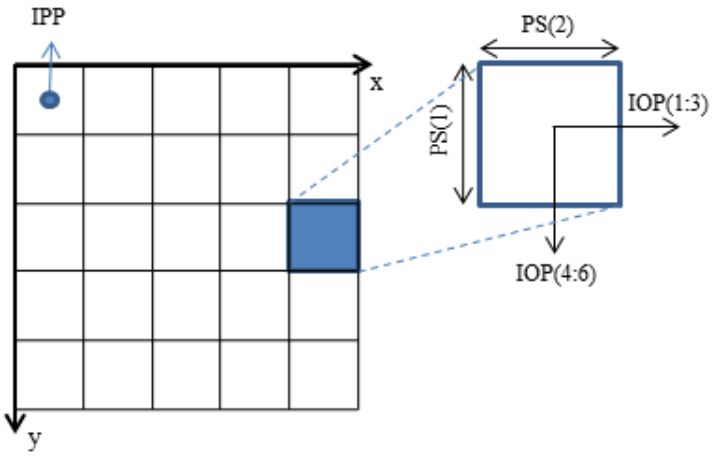

Figure B.1 Dicom Parameters

L: Left

P: Posterior

H:Head (Superior)

R: Patient coordinates of any pixel.

R = IPP + 4 x IOP(1:3) x PS(2) + 2 x IOP(4:6) x PS(1)

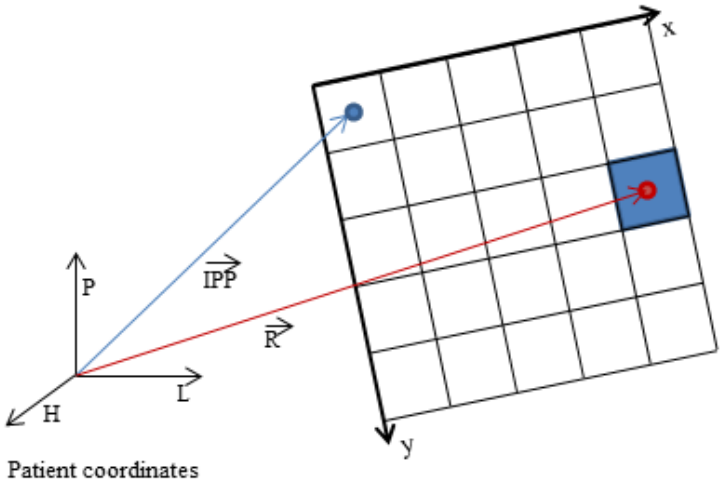

Figure B.2 Transformation between image and patient coordinates

In order to calculate the transformation matrix between image and patient coordinates, translation matrix of the first voxel (T_{IPP}) related to IPP, rotation matrix

(R) related to IOP, scaling matrix (S) related to PS and ST, and shifting matrix (T_0) to make top left voxel center at (0,0,0) are calculated.

B.2.1 Translation Matrix T_{IPP}

$$T_{IPP} = \begin{bmatrix} 1 & 0 & 0 & ipp_1 \\ 0 & 1 & 0 & ipp_2 \\ 0 & 0 & 1 & ipp_3 \\ 0 & 0 & 0 & 1 \end{bmatrix} \tag{B.1}$$

where ipp_1, ipp_2, and ipp_3 are the elements of IPP array.

B.2.2 Rotation Matrix (R)

Slice direction cosine ($\hat{s}$) is the cross-product of row ($\hat{r}$) and col ($\hat{c}$) direction cosines that are obtained from IOP.

$$\hat{r} = IOP(1:3) \tag{B.2}$$

$$\hat{c} = IOP(4:6) \tag{B.3}$$

$$\hat{s} = \hat{r} \times \hat{c} \tag{B.4}$$

$$R = \begin{bmatrix} r_1 & c_1 & s_1 & 0 \\ r_2 & c_2 & s_2 & 0 \\ r_3 & c_3 & s_3 & 0 \\ 0 & 0 & 0 & 1 \end{bmatrix} \tag{B.5}$$

where r_1, r_2, and r_3 are the elements of $\hat{r}$, c_1, c_2, and c_3 are the elements of $\hat{(}c)$, and s_1, s_2, and s_3 are the elements of $\hat{(}s)$.

B.2.3 Scaling Matrix (S)

$$S = \begin{bmatrix} ps_2 & 0 & 0 & 0 \\ 0 & ps_1 & 0 & 0 \\ 0 & 0 & st & 0 \\ 0 & 0 & 0 & 1 \end{bmatrix} \tag{B.6}$$

where ps_1 and ps_2 are the elements of PS, and st equals to ST.

B.2.4 Shifting matrix (T_0)

$$T_0 = \begin{bmatrix} 1 & 0 & 0 & 0 \\ 0 & 1 & 0 & 0 \\ 0 & 0 & 1 & 0 \\ 0 & 0 & 0 & 1 \end{bmatrix} \tag{B.7}$$

Shifting matrix is to make top left voxel center at (0,0,0).

B.2.5 Transformation matrix (M)

$$M = T_{IPP} \times R \times S \times T_0 \tag{B.8}$$

Image points $((x_1, y_1, z_1), (x_1, y_1, z_1), ...)$ are mapped to patient points $((l_1, p_1, h_1), (l_1, p_1, h_1), ...)$ using M.

$$\begin{bmatrix} l_1 & l_2 & ... \\ p_1 & p_2 & ... \\ h_1 & h_2 & ... \\ 1 & 1 & ... \end{bmatrix} = M \begin{bmatrix} x_1 & x_2 & ... \\ y_1 & y_2 & ... \\ z_1 & z_2 & ... \\ 1 & 1 & ... \end{bmatrix} \tag{B.9}$$

Transformation matrix from TurboFlash to DTI image coordinate system is the product of transformation matrices from (i) TurboFlash image coordinates to patient coordinates and (ii) patient coordinates to DTI coordinates.

$$M = M_{DTI}^{-1} M_{TF} \tag{B.10}$$

where M_DTI and M_TF are transformation matrices from DTI and TurboFlash image coordinate systems, respectively to common patient coordinate system.

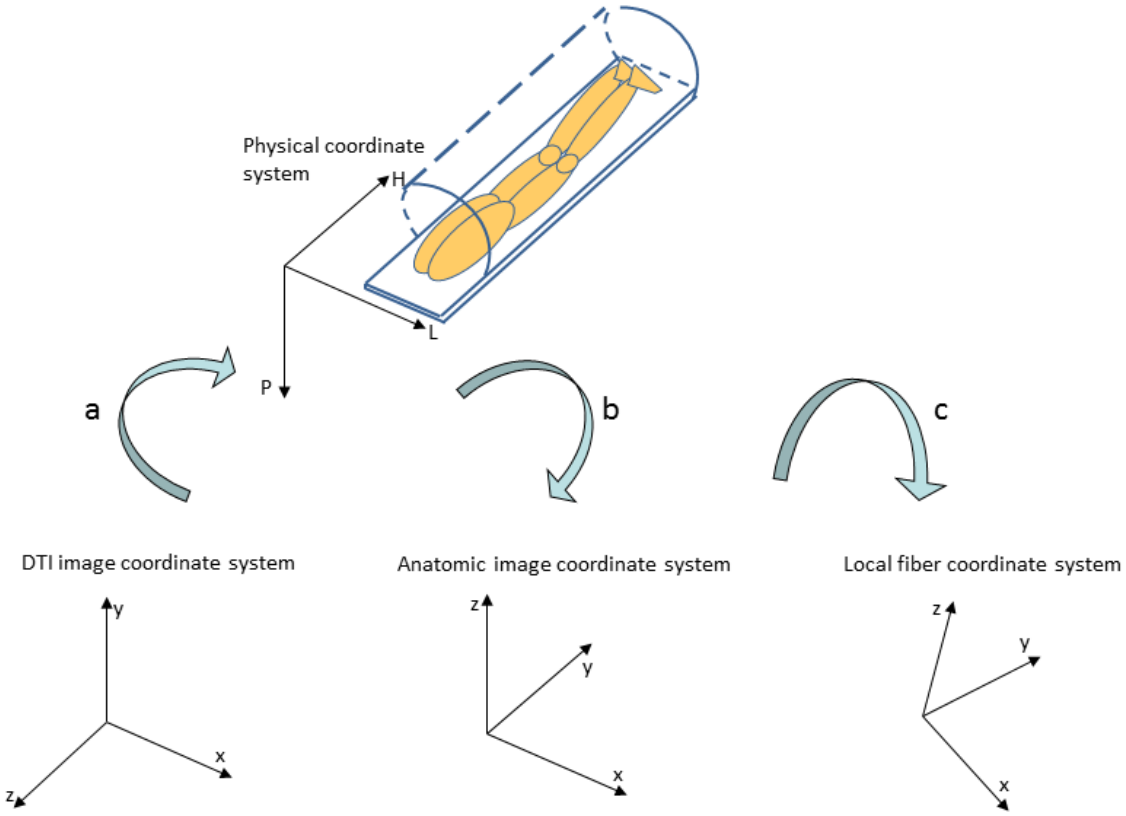

Figure B.3 Transformation between TurboFlash and DTI image coordinates

APPENDIX C. 3D RECONSTRUCTIONS OF MYOFASCIAL PATHWAYS AND MUSCLES

3D reconstructions were generated from 3D high resolution MR images using semi-automatic 3D analysis software Amira (FEI Visualization Sciences Group, Bordeaux, France). Myofascial pathways (e.g. neurovascular tracts, crural fascia, transverse intermuscular septum etc.) as well as muscular compartments and bones (tibia and fibula) were identified.

In figures 6-10 connective tissues were shown in different views.

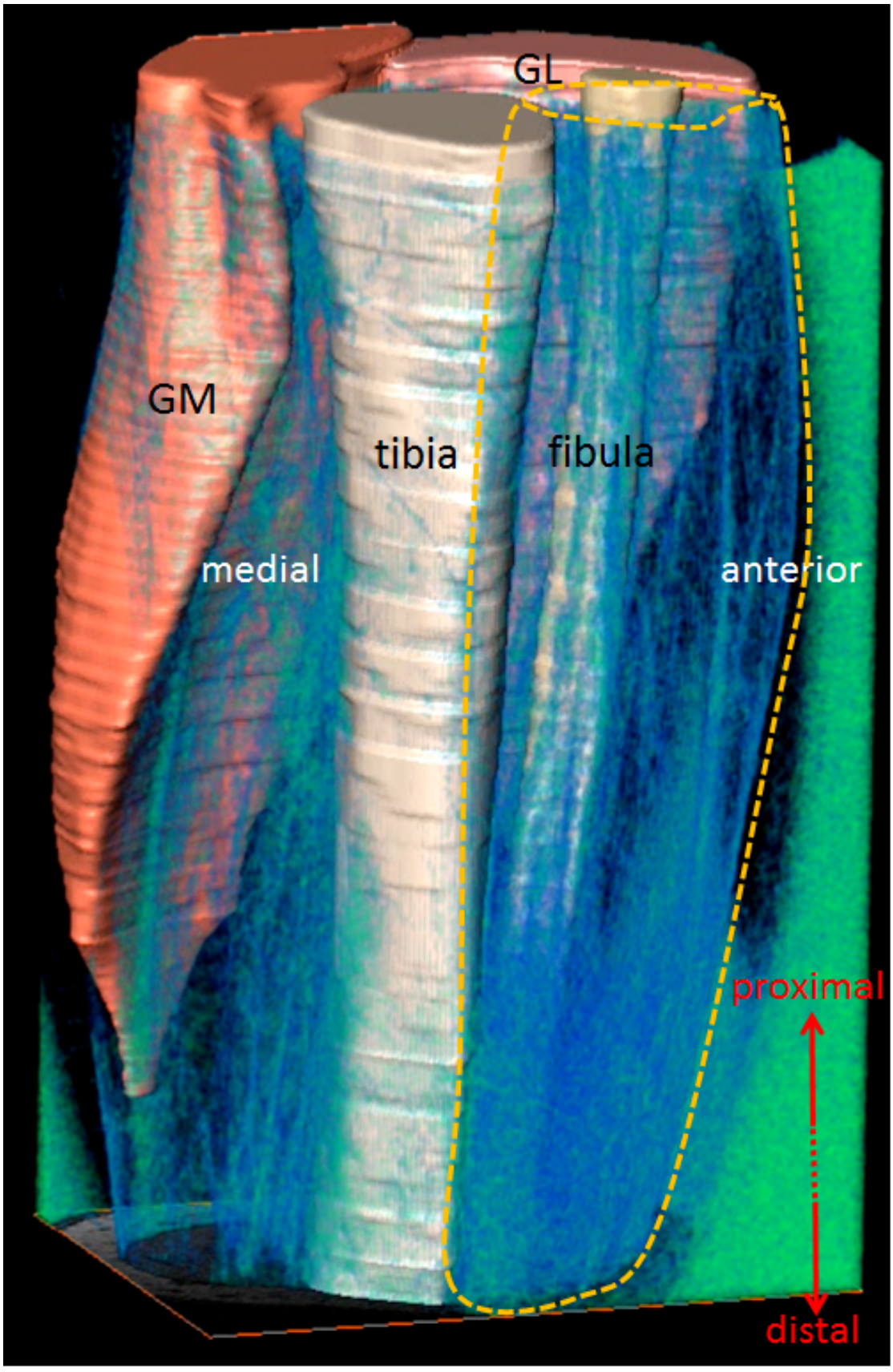

Figure C.1 Reconstruction of bones, m. gastrocnemius, and connective tissues in anterior crural compartment. Tibia, fibula, medial gastrocnemius, and lateral gastrocnemius were shown. Blue fibers penetrating through anterior crural compartment were delimited by orange lines. These fibers indicate crural fascia, epimysium of muscles, intramuscular connective tissue, and neurovascular tracts branching through.

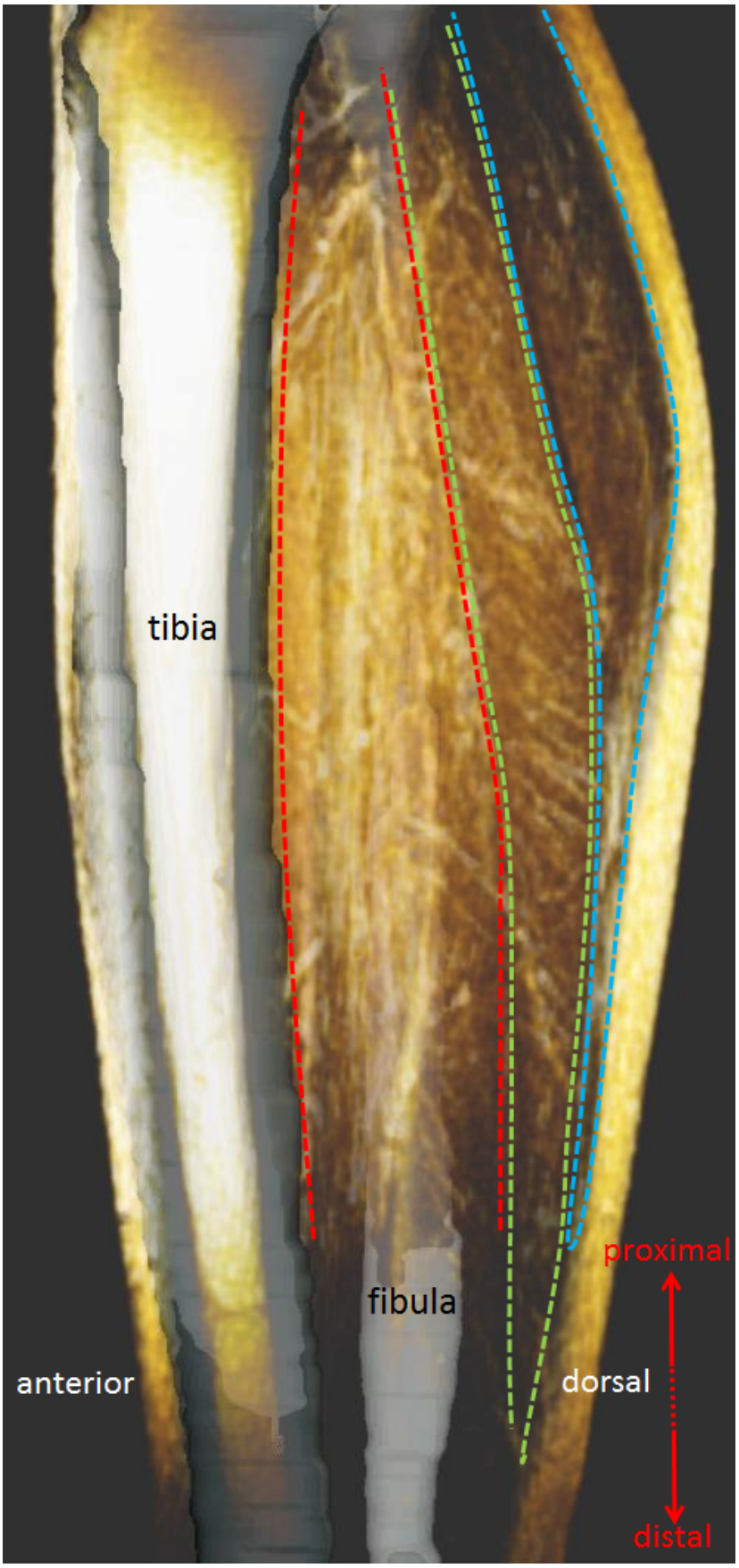

Figure C.2 Sagittal view of bones and connective tissues. Deep flexor muscles in deep posterior compartment, m. soleus, and m. gastrocnemius were delimited by red, green, and blue lines, respectively. Continuous 3D structures formed by neurovascular tracts and other intra-, inter-, and extramuscular connective tissues were denoted with yellow fibers.

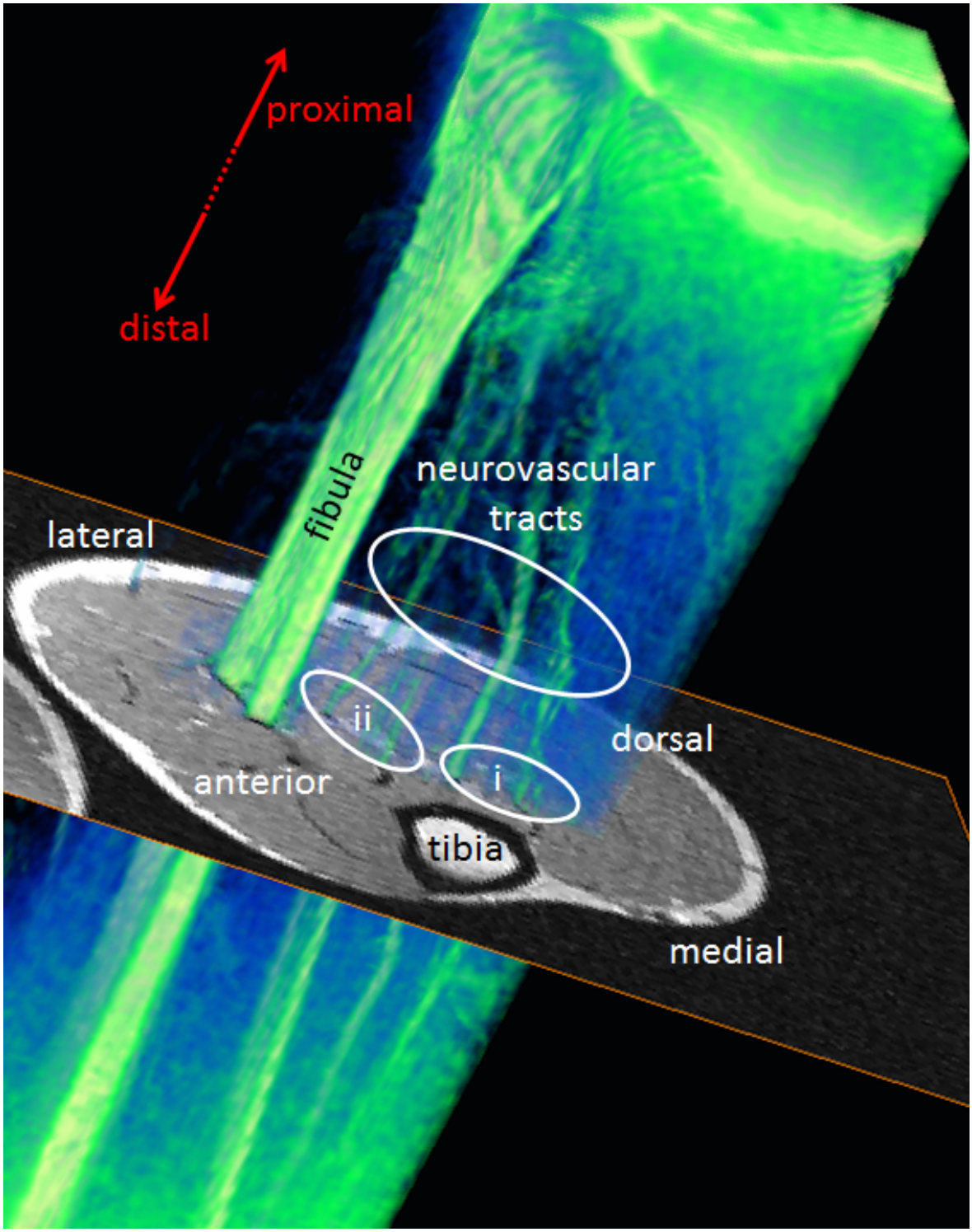

Figure C.3 Reconstruction of fibula and neurovascular tracts in deep posterior compartment through all slices. These neurovascular tracts include (i) posterior tibial artery, vein, and tibial nerve, and (ii) peroneal artery and vein.

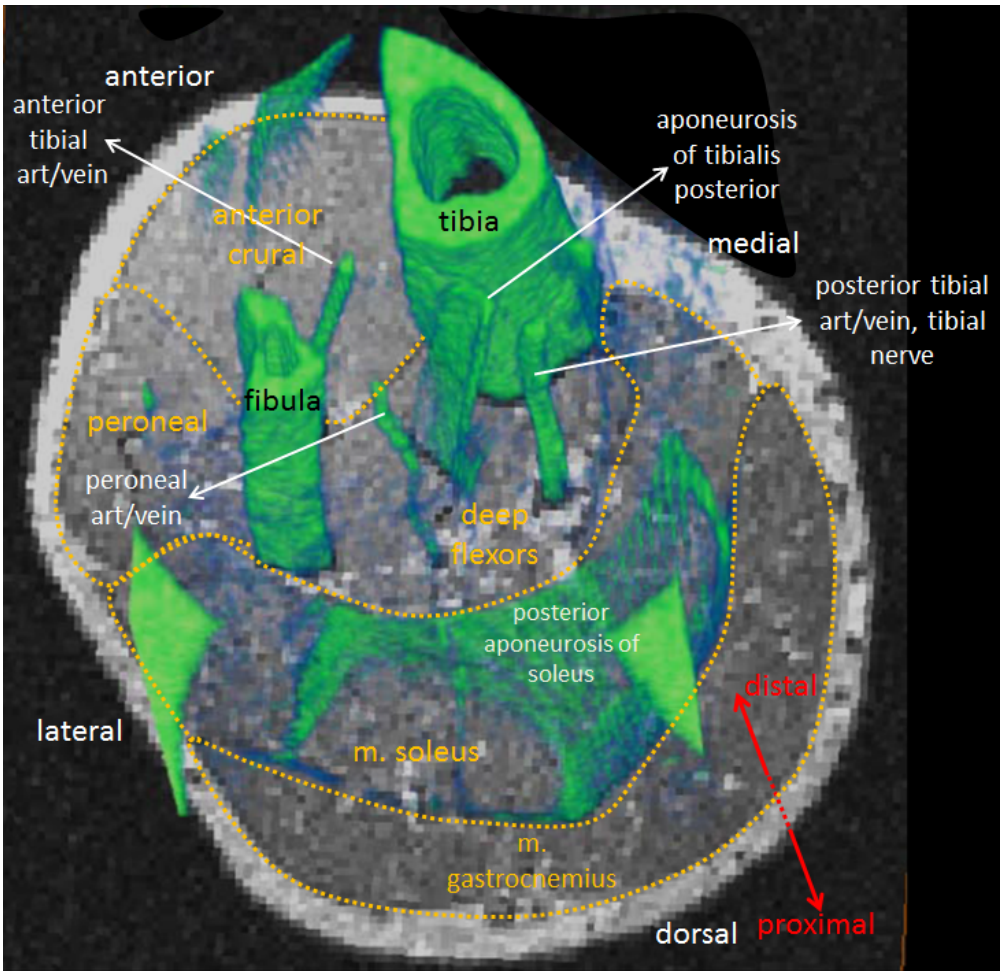

Figure C.4 Detailed identification of compartmental boundaries and neurovascular tracts. Orange lines delimit compartmental boundaries. White arrows denote neurovascular tracts including: (i) anterior tibial artery and vein, (ii) posterior tibial artery, vein, and nerve, (iii) peroneal artery and vein. Aponeurosis of tibialis posterior and posterior aponeurosis of m. soleus was shown.

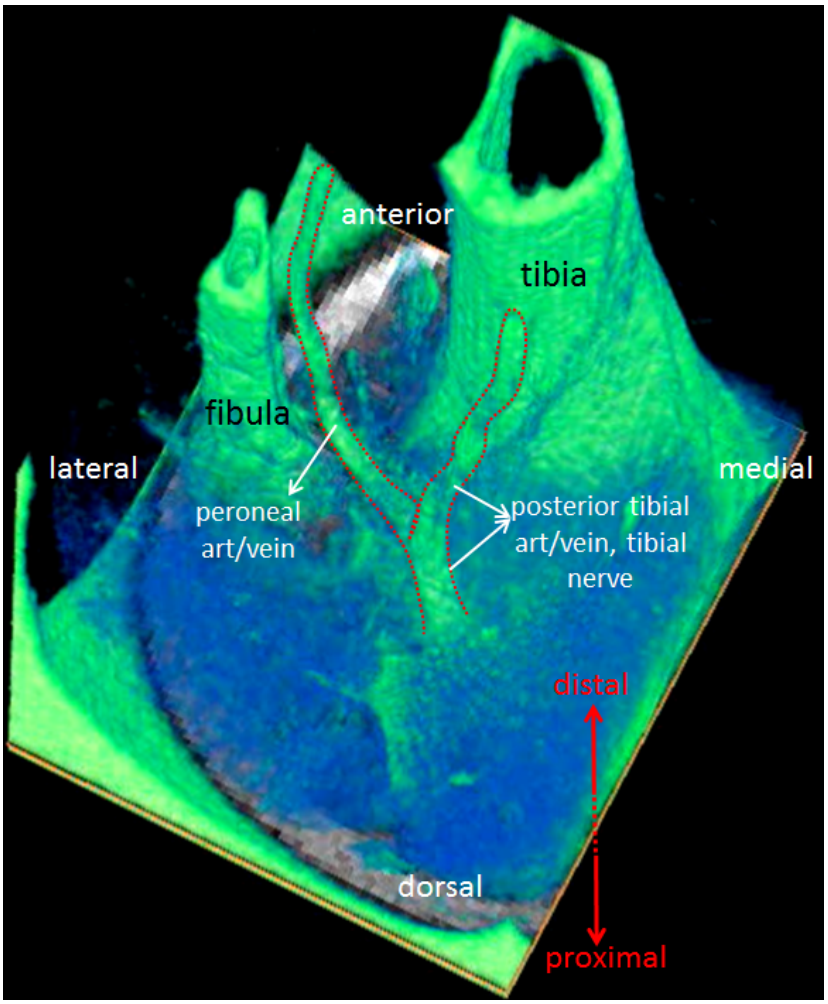

Figure C.5 Sample branching of a neurovascular tract. The neurovascular tracts surrounding posterior artery, vein, and nerve branch to peroneal artery and vein. These branches form a continuous connection between deep posterior and peroneal compartments.

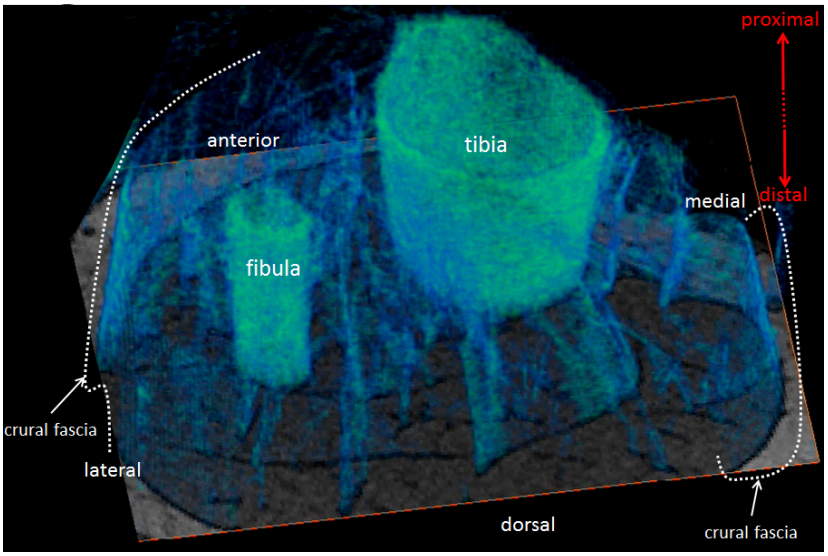

Figure C.6 Reconstruction of connective tissues. Blue fibers denote the connective tissues. White lines delimit the parts of crural fascia in medial and lateral peripherals.

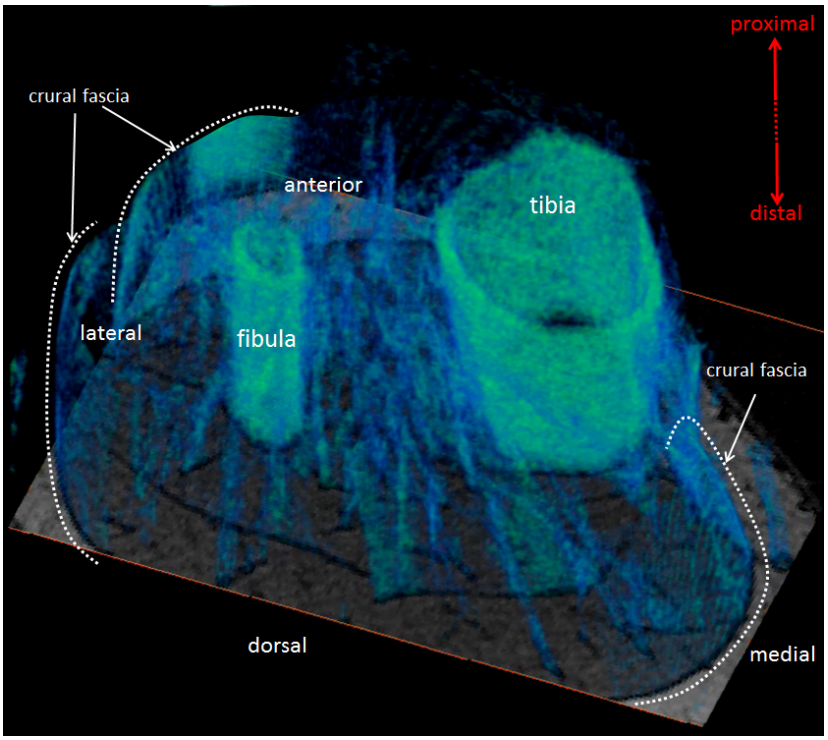

Figure C.7 Reconstruction of connective tissues. Blue fibers denote the connective tissues. White lines delimit the parts of crural fascia in medial and lateral peripherals.

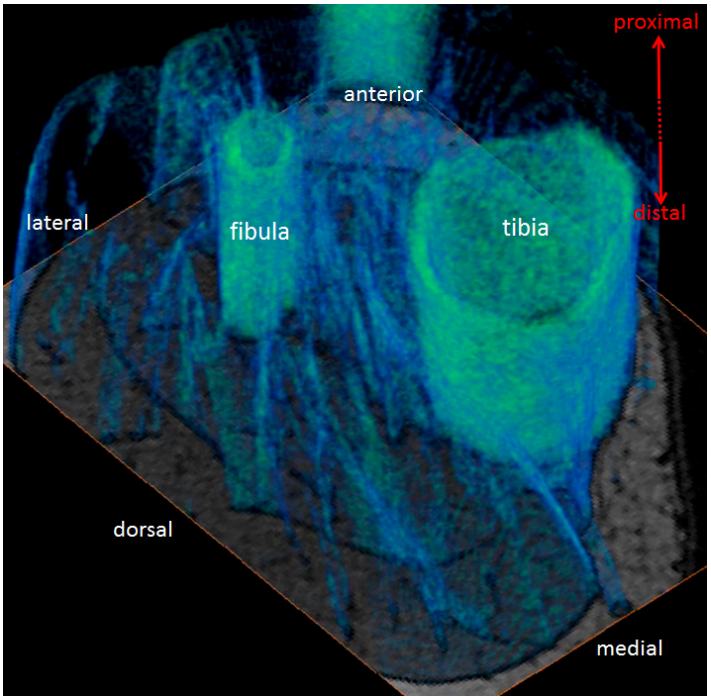

Figure C.8 Reconstruction of connective tissues. Blue fibers denote the connective tissues mostly in m. soleus and deep posterior compartment.

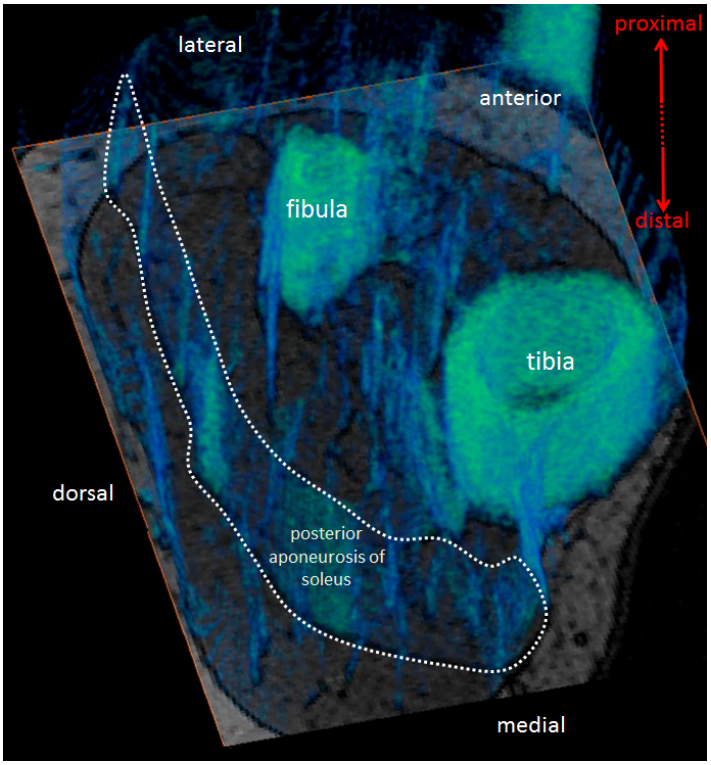

Figure C.9 Reconstruction of connective tissues. Blue fibers denote the connective tissues mostly in m. soleus and deep posterior compartment. White line delimits the posterior aponeurosis of m. soleus.

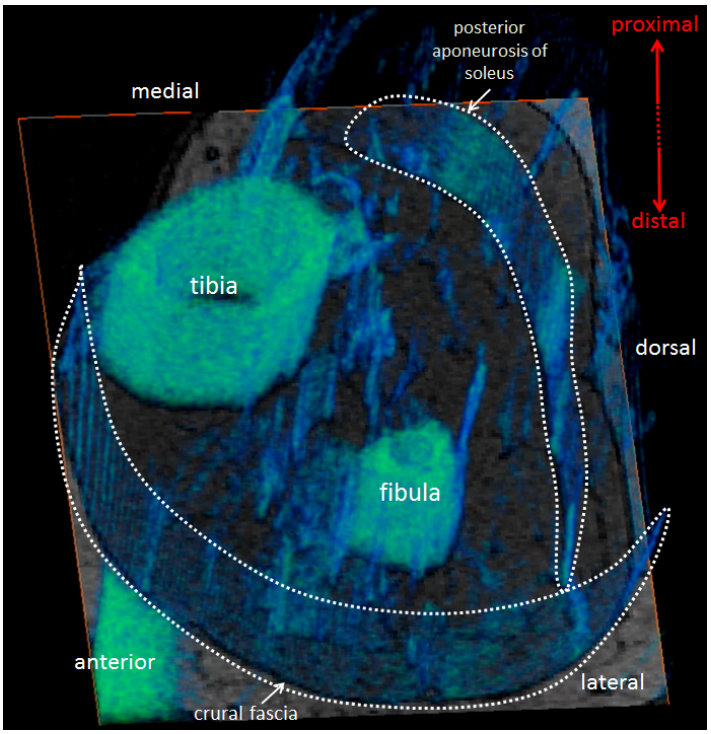

Figure C.10 Reconstruction of connective tissues. Blue fibers denote the connective tissues mostly in deep posterior compartment. White lines delimit the anterior part of crural fascia and the posterior aponeurosis of m. soleus.

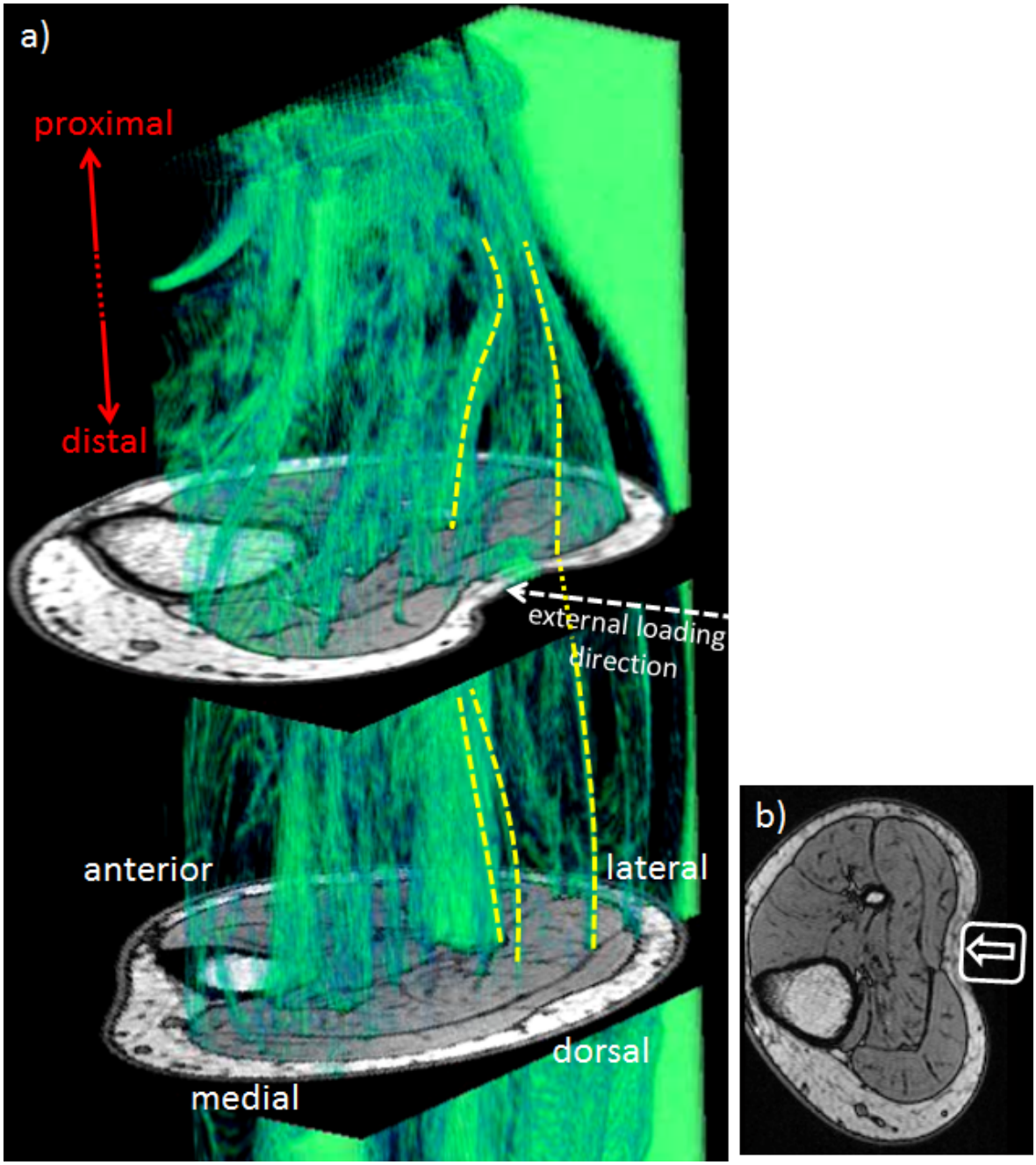

Figure C.11 Reconstruction of connective tissues as mechanical loading was applied. a) Green fibers denote the continuous structures of connective tissues in deep and superficial posterior compartments containing deep flexors, m. soleus, and m. gastrocnemius. Yellow lines show how external mechanical loading deforms connective tissues. b) The direction of external mechanical loading was shown on transverse slice.

REFERENCES

1. Berthier, C., and S. Blaineau, "Supramolecular organization of the subsarcolemmal cytoskeleton of adult skeletal muscle fibers. a review," *Biology of the Cell*, Vol. 89, no. 7, pp. 413–434, 1997.

2. Trotter, J. A., and P. P. Purslow, "Functional morphology of the endomysium in series fibered muscles," *J Morphol*, Vol. 212, no. 2, pp. 109–22, 1992.

3. Passerieux, E., R. Rossignol, A. Chopard, A. Carnino, J. F. Marini, T. Letellier, and J. P. Delage, "Structural organization of the perimysium in bovine skeletal muscle: Junctional plates and associated intracellular subdomains," *J Struct Biol*, Vol. 154, no. 2, pp. 206–16, 2006.

4. Passerieux, E., R. Rossignol, T. Letellier, and J. P. Delage, "Physical continuity of the perimysium from myofibers to tendons: involvement in lateral force transmission in skeletal muscle," *J Struct Biol*, Vol. 159, no. 1, pp. 19–28, 2007.

5. Tidball, J. G., "Myotendinous junction injury in relation to junction structure and molecular composition," *Exerc Sport Sci Rev*, Vol. 19, pp. 419–45, 1991.

6. Saladin, K. S., *Anatomy & physiology : the unity of form and function*, New York, NY: McGraw-Hill, 2012.

7. Rijkelijkhuizen, J. M., H. J. M. Meijer, G. C. Baan, and P. A. Huijing, "Myofascial force transmission also occurs between antagonistic muscles located within opposite compartments of the rat lower hind limb," *Journal of Electromyography and Kinesiology*, Vol. 17, no. 6, pp. 690–697, 2007.

8. Yucesoy, C. A., G. Baan, and P. A. Huijing, "Epimuscular myofascial force transmission occurs in the rat between the deep flexor muscles and their antagonistic muscles," *J Electromyogr Kinesiol*, Vol. 20, no. 1, pp. 118–26, 2010.

9. Huijing, P., "Muscular force transmission: a unified, dual or multiple system? a review and some explorative experimental results," *Arch Physiol Biochem*, Vol. 107, no. 4, pp. 292–311, 1999.

10. Huijing, P. A., G. C. Baan, and G. T. Rebel, "Non-myotendinous force transmission in rat extensor digitorum longus muscle," *J Exp Biol*, Vol. 201, no. Pt 5, pp. 683–91, 1998.

11. Huijing, P. A., and G. C. Baan, "Myofascial force transmission causes interaction between adjacent muscles and connective tissue: effects of blunt dissection and compartmental fasciotomy on length force characteristics of rat extensor digitorum longus muscle," *Arch Physiol Biochem*, Vol. 109, no. 2, pp. 97–109, 2001.

12. Huijing, P. A., and G. C. Baan, "Extramuscular myofascial force transmission within the rat anterior tibial compartment: proximo-distal differences in muscle force," *Acta Physiol Scand*, Vol. 173, no. 3, pp. 297–311, 2001.

13. Maas, H., G. C. Baan, and P. A. Huijing, "Intermuscular interaction via myofascial force transmission: effects of tibialis anterior and extensor hallucis longus length on force transmission from rat extensor digitorum longus muscle," *J Biomech*, Vol. 34, no. 7, pp. 927–40, 2001.

14. Huijing, P. A., and G. C. Baan, "Myofascial force transmission: muscle relative position and length determine agonist and synergist muscle force," *J Appl Physiol*, Vol. 94, no. 3, pp. 1092–107, 2003.

15. Yucesoy, C. A., B. H. Koopman, G. C. Baan, H. J. Grootenboer, and P. A. Huijing, "Effects of inter- and extramuscular myofascial force transmission on adjacent synergistic muscles: assessment by experiments and finite-element modeling," *J Biomech*, Vol. 36, no. 12, pp. 1797–811, 2003.

16. Rijkelijkhuizen, J. M., G. C. Baan, A. de Haan, C. J. de Ruiter, and P. A. Huijing, "Extramuscular myofascial force transmission for in situ rat medial gastrocnemius and plantaris muscles in progressive stages of dissection," *J Exp Biol*, Vol. 208, no. Pt 1, pp. 129–40, 2005.

17. Yucesoy, C. A., G. C. Baan, B. H. Koopman, H. J. Grootenboer, and P. A. Huijing, "Pre-strained epimuscular connections cause muscular myofascial force transmission to affect properties of synergistic ehl and edl muscles of the rat," *J Biomech Eng*, Vol. 127, no. 5, pp. 819–28, 2005.

18. Yucesoy, C. A., H. Maas, B. H. Koopman, H. J. Grootenboer, and P. A. Huijing, "Mechanisms causing effects of muscle position on proximo-distal muscle force differences in extra-muscular myofascial force transmission," *Med Eng Phys*, Vol. 28, no. 3, pp. 214–26, 2006.

19. Maas, H., G. C. Baan, P. A. Huijing, C. A. Yucesoy, B. H. F. J. M. Koopman, and H. J. Grootenboer, "The relative position of edl muscle affects the length of sarcomeres within muscle fibers: Experimental results and finite-element modeling," *Journal of Biomechanical Engineering*, Vol. 125, no. 5, pp. 745–753, 2003.

20. Yucesoy, C. A., B. H. Koopman, G. C. Baan, H. J. Grootenboer, and P. A. Huijing, "Extramuscular myofascial force transmission: experiments and finite element modeling," *Arch Physiol Biochem*, Vol. 111, no. 4, pp. 377–88, 2003.

21. Asakawa, D. S., S. S. Blemker, G. E. Gold, and S. L. Delp, "In vivo motion of the rectus femoris muscle after tendon transfer surgery," *J Biomech*, Vol. 35, no. 8, pp. 1029–37, 2002.

22. Asakawa, D. S., S. S. Blemker, G. E. Gold, and S. L. Delp, "Dynamic magnetic resonance imaging of muscle function after surgery," *Skeletal Radiol*, Vol. 35, no. 12, pp. 885–6, 2006.

23. Kreulen, M., M. J. Smeulders, J. J. Hage, and P. A. Huijing, "Biomechanical effects of dissecting flexor carpi ulnaris," *J Bone Joint Surg Br*, Vol. 85, no. 6, pp. 856–9, 2003.

24. Smeulders, M. J. C., and M. Kreulen, "Myofascial force transmission and tendon transfer for patients suffering from spastic paresis: A review and some new observations," *Journal of Electromyography and Kinesiology*, Vol. 17, no. 6, pp. 644–656, 2007.

25. Ates, F., R. N. Ozdeslik, P. A. Huijing, and C. A. Yucesoy, "Muscle lengthening surgery causes differential acute mechanical effects in both targeted and non-targeted synergistic muscles," *J Electromyogr Kinesiol*, Vol. 23, no. 5, pp. 1199–205, 2013.

26. Yucesoy, C. A., F. Ates, U. Akgun, and M. Karahan, "Measurement of human gracilis muscle isometric forces as a function of knee angle, intraoperatively," *J Biomech*, Vol. 43, no. 14, pp. 2665–71, 2010.

27. Ates, F., Y. Temelli, and C. A. Yucesoy, "Human spastic gracilis muscle isometric forces measured intraoperatively as a function of knee angle show no abnormal muscular mechanics," *Clin Biomech (Bristol, Avon)*, Vol. 28, no. 1, pp. 48–54, 2013.

28. Yucesoy, C. A., O. Emre Arikan, and F. Ates, "Btx-a administration to the target muscle affects forces of all muscles within an intact compartment and epimuscular myofascial force transmission," *J Biomech Eng*, Vol. 134, no. 11, p. 111002, 2012.

29. Ates, F., and C. A. Yucesoy, "Effects of btx-a on non-injected bi-articular muscle include a narrower length range of force exertion and increased passive force," *Muscle Nerve*, 2013.

30. Agur, A. M., V. Ng-Thow-Hing, K. A. Ball, E. Fiume, and N. H. McKee, "Documentation and three-dimensional modelling of human soleus muscle architecture," *Clin Anat*, Vol. 16, no. 4, pp. 285–93, 2003.

31. Chow, R. S., M. K. Medri, D. C. Martin, R. N. Leekam, A. M. Agur, and N. H. McKee, "Sonographic studies of human soleus and gastrocnemius muscle architecture: gender variability," *Eur J Appl Physiol*, Vol. 82, no. 3, pp. 236–44, 2000.

32. Finni, T., J. A. Hodgson, A. M. Lai, V. R. Edgerton, and S. Sinha, "Mapping of movement in the isometrically contracting human soleus muscle reveals details of its structural and functional complexity," *J Appl Physiol (1985)*, Vol. 95, no. 5, pp. 2128–33, 2003.

33. Loh, E. Y., A. M. Agur, and N. H. McKee, "Intramuscular innervation of the human soleus muscle: a 3d model," *Clin Anat*, Vol. 16, no. 5, pp. 378–82, 2003.

34. Netter, F., *Atlas of Human Anatomy*, Netter Basic Science, Elsevier Health Sciences, 2010.

35. Ozturk, C., and E. R. McVeigh, "Four-dimensional b-spline based motion analysis of tagged mr images: introduction and in vivo validation," *Phys Med Biol*, Vol. 45, no. 6, pp. 1683–702, 2000.

36. Finni, T., J. A. Hodgson, A. M. Lai, V. R. Edgerton, and S. Sinha, "Nonuniform strain of human soleus aponeurosis-tendon complex during submaximal voluntary contractions in vivo," *J Appl Physiol*, Vol. 95, no. 2, pp. 829–37, 2003.

37. Lee, H. D., T. Finni, J. A. Hodgson, A. M. Lai, V. R. Edgerton, and S. Sinha, "Soleus aponeurosis strain distribution following chronic unloading in humans: an in vivo mr phase-contrast study," *J Appl Physiol*, Vol. 100, no. 6, pp. 2004–11, 2006.

38. Osman, N. F., E. R. McVeigh, and J. L. Prince, "Imaging heart motion using harmonic phase mri," *IEEE Trans Med Imaging*, Vol. 19, no. 3, pp. 186–202, 2000.

39. Zhong, X., F. H. Epstein, B. S. Spottiswoode, P. A. Helm, and S. S. Blemker, "Imaging two-dimensional displacements and strains in skeletal muscle during joint motion by cine dense mr," *J Biomech*, Vol. 41, no. 3, pp. 532–40, 2008.

40. Osman, N. F., S. Sampath, E. Atalar, and J. L. Prince, "Imaging longitudinal cardiac strain on short-axis images using strain-encoded mri," *Magn Reson Med*, Vol. 46, no. 2, pp. 324–34, 2001.

41. Thirion, J. P., "Image matching as a diffusion process: an analogy with maxwell's demons," *Med Image Anal*, Vol. 2, no. 3, pp. 243–60, 1998.

42. Le Bihan, D., J. F. Mangin, C. Poupon, C. A. Clark, S. Pappata, N. Molko, and H. Chabriat, "Diffusion tensor imaging: concepts and applications," *J Magn Reson Imaging*, Vol. 13, no. 4, pp. 534–46, 2001.

43. Le Bihan, D., E. Breton, D. Lallemand, P. Grenier, E. Cabanis, and M. Laval-Jeantet, "Mr imaging of intravoxel incoherent motions: application to diffusion and perfusion in neurologic disorders," *Radiology*, Vol. 161, no. 2, pp. 401–7, 1986.

44. Stejskal, E. O., and J. E. Tanner, "Spin diffusion measurements: Spin echoes in the presence of a time-dependent field gradient," *The Journal of Chemical Physics*, Vol. 42, no. 1, pp. 288–292, 1965.

45. Damon, B. M., Z. Ding, A. W. Anderson, A. S. Freyer, and J. C. Gore, "Validation of diffusion tensor mri-based muscle fiber tracking," *Magn Reson Med*, Vol. 48, no. 1, pp. 97–104, 2002.

46. Sinha, S., U. Sinha, and V. R. Edgerton, "In vivo diffusion tensor imaging of the human calf muscle," *J Magn Reson Imaging*, Vol. 24, no. 1, pp. 182–90, 2006.

47. Heemskerk, A. M., T. K. Sinha, K. J. Wilson, Z. Ding, and B. M. Damon, "Repeatability of dti-based skeletal muscle fiber tracking," *NMR Biomed*, Vol. 23, no. 3, pp. 294–303, 2010.

48. Zaraiskaya, T., D. Kumbhare, and M. D. Noseworthy, "Diffusion tensor imaging in evaluation of human skeletal muscle injury," *J Magn Reson Imaging*, Vol. 24, no. 2, pp. 402–8, 2006.

49. Lundberg, A., "Kinematics of the ankle and foot. in vivo roentgen stereophotogrammetry," *Acta Orthop Scand Suppl*, Vol. 233, pp. 1–24, 1989.

50. Crisco, J., R. McGovern, and S. Wolfe, "Noninvasive technique for measuring in vivo three-dimensional carpal bone kinematics," *J. Ortho. Res.*, Vol. 17, pp. 96–100, 1999.

51. Gilbert, J., G. Wheeler, R. Lingreen, and R. Johnson, "Open stand-up mri: A new instrument for positional neuroimaging," *J. of Spinal Dis.&Tech*, Vol. 19, pp. 151–154, 2006.

52. Stark, D., and W. Bradley, *Magnetic Resonance Imaging*, Mosby, 3 ed., 1999.

53. Haacke, E., R. Brown, M. Thompson, and R. Venkatesan, *Magnetic Resonance Imaging: Physical Principles and Sequence Design*, John Wiley & Sons, 1999.

54. Epstein, F. H., S. D. Wolff, and A. E. Arai, "Segmented k-space fast cardiac imaging using an echo-train readout," *Magn. Reson. Med.*, Vol. 41, no. 3, pp. 609–13, 1999.

55. Meyer, C., B. Hu, D. Nishimura, and A. Makovski, "Fast spiral coronary artery imaging," *Magn. Reson. Med.*, Vol. 28, no. 2, pp. 202–213, 1992.

56. Pruessmann, K., M. Weiger, M. Scheidegger, and P. Boesiger, "Sense: Sensitivity encoding for fast mri," *Magn. Reson. Med.*, Vol. 42, pp. 952–962, 1999.

57. Feinstein, J., F. Epstein, A. Arai, T. Foo, R. Balaban, and S. D. Wolff, "Using cardiac phase to order reconstruction (captor): A method to improve diastolic images," *J. Magn. Reson. Imag.*, Vol. 7, no. 5, pp. 794–798, 1997.

58. Reeder, S., and A. Faranesh, "Ultrafast pulse sequence techniques for cardiac magnetic resonance imaging," *Top Magn Reson Imaging*, Vol. 11, no. 6, pp. 312–330, 2000.

59. Pentland, A., and B. Horowitz, "Recovery of nonrigid motion and structure," *IEEE Trans PAMI*, Vol. 13, pp. 730–742, 1991.

60. Duncan, J., R. Owen, L. Staib, and E. Anandan, "Measurement of non-rigid motion using contour shape descriptors," *IEEE Comput. Soc. Comput. Vision Pattern Recognition*, pp. 318–324, 1991.

61. Shi, E., A. Amini, G. Robinson, A. Sinusas, C. Constable, and J. Duncan, "Shape-based 4d left ventricular myocardial function analysis," in *IEEE Workshop on Biomedical Image Analysis*, pp. 88–97.

62. Stindel, E., J. Udupa, B. Hirsch, and D. Odhner, "An in vivo analysis of the peri-talar joint complex based on mr imaging," *IEEE Trans BME*, Vol. 48, pp. 236–247, 2001.

63. Rhoad, R., J. Klimkiewicz, G. Williams, S. Kesmodel, J. Udupa, J. Kneeland, and J. Iannotti, "A new in vivo technique for 3d shoulder kinematics analysis," *Skeletal Radiology*, Vol. 27, pp. 92–97, 1998.

64. McGregor, A., "Assessment of spinal kinematics using open interventional magnetic resonance imaging," *Clin Orthop*, Vol. 392, pp. 341–348, 2001.

65. Sheehan, F., "Quantitative mr measures of three-dimensional patellar kinematics as a research and diagnostic tool," *Med Sci Sports Exerc*, Vol. 31, no. 10, pp. 1399–1405, 1999.

66. Keir, P. J., "Magnetic resonance imaging as a research tool for biomechanical studies of the wrist," *Semin Musculoskelet Radiol*, Vol. 5, no. 3, pp. 241–250, 2001.

67. Arnold, A., "Accuracy of muscle moment arms estimated from mri-based musculoskeletal models of the lower extremity," *Comput Aided Surgery*, Vol. 5, no. 2, pp. 108–119, 2000.

68. Rentsc, M., "Dynamic magnetic resonance imaging defecography: a diagnostic alternative in the assessment of pelvic floor disorders in proctology," *Dis Colon Rectum*, Vol. 44, no. 7, pp. 999–1007, 2001.

69. Hammer, W. I., "The effect of mechanical load on degenerated soft tissue," *J Bodyw Mov Ther*, Vol. 12, no. 3, pp. 246–56, 2008.

70. Axel, L., and L. Dougherty, "Mr imaging of motion with spatial modulation of magnetization," *Radiology*, Vol. 171, pp. 841–845, 1989.

71. Zhu, Y., and N. J. Pelc, "Three-dimensional motion tracking with volumetric phase contrast cmr velocity imaging," *J. Magn. Reson. Imag.*, Vol. 9, pp. 111–118, 1999.

72. Aletras, A. H., R. S. Balaban, and H. Wen, "High-resolution strain analysis of the human heart with fast-dense," *J. Magn. Reson. Imag.*, Vol. 140, pp. 41–57, 1999.

73. Huijing, P. A., "Epimuscular myofascial force transmission between antagonistic and synergistic muscles can explain movement limitation in spastic paresis," *J Electromyogr Kinesiol*, Vol. 17, no. 6, pp. 708–24, 2007.

74. Huijing, P. A., "Epimuscular myofascial force transmission: a historical review and implications for new research. international society of biomechanics muybridge award lecture, taipei, 2007," *J Biomech*, Vol. 42, no. 1, pp. 9–21, 2009.

75. Kreulen, M., M. J. Smeulders, J. J. Hage, and P. Huijing, "Biomechanical aspects of surgical muscle dissection in a tendon transfer procedure," in *J Hand Surg*, Vol. 27B, p. 55, Sixteenth Century Journal.

76. Smeulders, M. J., M. Kreulen, J. J. Hage, G. C. Baan, and P. A. Huijing, "Progressive surgical dissection for tendon transposition affects length-force characteristics of rat flexor carpi ulnaris muscle," *J Orthop Res*, Vol. 20, no. 4, pp. 863–8, 2002.

77. Smeulders, M. J., M. Kreulen, J. J. Hage, P. A. Huijing, and C. M. van der Horst, "Intraoperative measurement of force-length relationship of human forearm muscle," *Clin Orthop Relat Res*, no. 418, pp. 237–41, 2004.

78. Smeulders, M. J., M. Kreulen, J. J. Hage, P. A. Huijing, and C. M. van der Horst, "Overstretching of sarcomeres may not cause cerebral palsy muscle contracture," *J Orthop Res*, Vol. 22, no. 6, pp. 1331–5, 2004.

79. Smeulders, M. J., M. Kreulen, J. J. Hage, P. A. Huijing, and C. M. van der Horst, "Spastic muscle properties are affected by length changes of adjacent structures," *Muscle Nerve*, Vol. 32, no. 2, pp. 208–15, 2005.

80. Yu, W. S., S. L. Kilbreath, R. C. Fitzpatrick, and S. C. Gandevia, "Thumb and finger forces produced by motor units in the long flexor of the human thumb," *J Physiol*, Vol. 583, no. Pt 3, pp. 1145–54, 2007.

81. Maas, H., H. J. Meijer, and P. A. Huijing, "Intermuscular interaction between synergists in rat originates from both intermuscular and extramuscular myofascial force transmission," *Cells Tissues Organs*, Vol. 181, no. 1, pp. 38–50, 2005.

82. Grieve, D., S. Pheasant, and P. Cavanagh, *Prediction of gastrocnemius length from knee and ankle joint posture.*, Vol. VI, pp. 405–412. Baltimore, MD: University Park Press, international series on biomechanics, 2a, ed., 1978.

83. Visser, J. J., J. E. Hoogkamer, M. F. Bobbert, and P. A. Huijing, "Length and moment arm of human leg muscles as a function of knee and hip-joint angles," *Eur J Appl Physiol Occup Physiol*, Vol. 61, no. 5-6, pp. 453–60, 1990.

84. Cachier, P., X. Pennec, and N. Ayache, "Fast non-rigid matching by gradient descent: study and improvement of the 'demons' algorithm," Tech. Rep. RR-3706, INRIA, 1999.

85. Kroon, D. J., and C. H. Slump, "Mri modalitiy transformation in demon registration," in *ISBI'09: Proceedings of the Sixth IEEE international conference on Symposium on Biomedical Imaging*, pp. 963–966, IEEE Press.

86. Wang, H., L. Dong, J. O'Daniel, R. Mohan, A. S. Garden, K. K. Ang, D. A. Kuban, M. Bonnen, J. Y. Chang, and R. Cheung, "Validation of an accelerated 'demons' algorithm for deformable image registration in radiation therapy," *Phys Med Biol*, Vol. 50, no. 12, pp. 2887–905, 2005.

87. Moglo, K. E., and A. Shirazi-Adl, "Cruciate coupling and screw-home mechanism in passive knee joint during extension–flexion," *J Biomech*, Vol. 38, no. 5, pp. 1075–83, 2005.

88. Yaman, A., M. J. Ledesma-Carbayo, G. Baan, P. Huijing, C. Ozturk, and C. A. Yucesoy, "Assessment using mri shows that inter-synergistic as well as inter-antagonistic epimuscular myofascial force transmission has sizable effects within the entire human lower leg, in vivo.," 2009.

89. Bonn, A., *Specimen Anatomico-Medicum Inaugurate de Continuationibus Membranarum, quod publico; ac solemni disquisitioni submisit.* PhD thesis, 1763.

90. Bonn, A., *Specimen anatomico-medicum inaugurale De continuationibus membranarum, quod publicae ac solemni disquisitioni submisit Andreas Bonn, Amstelaedamo-Batavus. Ad diem 14. octobris MDCCLXIII*, Apud Henricum Beman: Roterodami, 1769.

91. Maas, H., and T. G. Sandercock, "Are skeletal muscles independent actuators? force transmission from soleus muscle in the cat," *J Appl Physiol*, Vol. 104, no. 6, pp. 1557–67, 2008.

92. Herbert, R. D., P. D. Hoang, and S. C. Gandevia, "Are muscles mechanically independent?," *J Appl Physiol (1985)*, Vol. 104, no. 6, pp. 1549–50, 2008.

93. Bojsen-Moller, J., S. Schwartz, K. K. Kalliokoski, T. Finni, and S. P. Magnusson, "Intermuscular force transmission between human plantarflexor muscles in vivo," *J Appl Physiol (1985)*, Vol. 109, no. 6, pp. 1608–18, 2010.

94. Yucesoy, C. A., and P. A. Huijing, "Substantial effects of epimuscular myofascial force transmission on muscular mechanics have major implications on spastic muscle and remedial surgery," *J Electromyogr Kinesiol*, Vol. 17, no. 6, pp. 664–79, 2007.

95. De Bruin, M., M. J. Smeulders, M. Kreulen, P. Huijing, and R. T. Jaspers, "A comparison of intramuscular connective tissue content in spastic muscle versus healthy controls," in *11th Triennial Congress of the International Federation of Societies for Surgery of the Hand*, pp. 256–257.

96. Huijing, P. A., N. C. Voermans, G. C. Baan, T. E. Buse, B. G. van Engelen, and A. de Haan, "Muscle characteristics and altered myofascial force transmission in tenascin-x-deficient mice, a mouse model of ehlers-danlos syndrome," *J Appl Physiol*, Vol. 109, no. 4, pp. 986–95, 2010.

97. Huijing, P. A., "Muscle as a collagen fiber reinforced composite: a review of force transmission in muscle and whole limb," *J Biomech*, Vol. 32, no. 4, pp. 329–45, 1999.

98. Yucesoy, C. A., B. H. Koopman, P. A. Huijing, and H. J. Grootenboer, "Three-dimensional finite element modeling of skeletal muscle using a two-domain approach: linked fiber-matrix mesh model," *J Biomech*, Vol. 35, no. 9, pp. 1253–62, 2002.

99. Chaudhry, H., C.-Y. Huang, R. Schleip, Z. Ji, B. Bukiet, and T. Findley, "Viscoelastic behavior of human fasciae under extension in manual therapy," *Journal of Bodywork and Movement Therapies*, Vol. 11, no. 2, pp. 159–167, 2007.

100. Street, S. F., "Lateral transmission of tension in frog myofibers: a myofibrillar network and transverse cytoskeletal connections are possible transmitters," *J Cell Physiol*, Vol. 114, no. 3, pp. 346–64, 1983.

101. Norkin, C., and D. White, *Measurement of joint motion: a guide to goniometry*, F.A. Davis, 1995.

102. Weis, J., A. Ericsson, and A. Hemmingsson, "Chemical shift artifact-free imaging: a new option in mri?," *Magn Reson Imaging*, Vol. 16, no. 7, pp. 839–44, 1998.

103. Matsumoto, M., and T. Nishimura, "Mersenne twister: a 623-dimensionally equidistributed uniform pseudo-random number generator," *ACM Trans. Model. Comput. Simul.*, Vol. 8, no. 1, pp. 3–30, 1998.

104. Huijing, P. A., A. Yaman, C. Ozturk, and C. A. Yucesoy, "Effects of knee joint angle on global and local strains within human triceps surae muscle: Mri analysis indicating in vivo myofascial force transmission between synergistic muscles," *Surg Radiol Anat*, Vol. 33, no. 10, pp. 869–79, 2011.

105. Hioki, S., T. Fukubayashi, K. Ikeda, M. Niitsu, and N. Ochiai, "Effect of harvesting the hamstrings tendon for anterior cruciate ligament reconstruction on the morphology and movement of the hamstrings muscle: a novel mri technique," *Knee Surg Sports Traumatol Arthrosc*, Vol. 11, no. 4, pp. 223–7, 2003.

106. MJ, L.-c., A. Bajo, C. S. Marta, E. Perez-david, I. Caso, G.-f. Ma, A. Santos, and M. Desco, "Cardiac motion analysis from cine mr sequences using non-rigid registration techniques," *Computers in Cardiology*, Vol. 33, pp. 65–68, 2008.

107. Mansi, T., J.-M. Peyrat, M. Sermesant, H. Delingette, J. Blanc, Y. Boudjemline, and N. Ayache, "Physically-constrained diffeomorphic demons for the estimation of 3d myocardium strain from cine-mri," 2009.

108. Ledesma-Carbayo, M. J., A. Santos, J. Kybic, P. Mahia-Casado, M. A. Garcia-Fernandez, N. Malpica, E. Perez-David, and M. Desco, "Myocardial strain analysis of echocardiographic sequences using nonrigid registration," in *Computers in Cardiology*, pp. 313–316.

109. Ledesma-Carbayo, M. J., J. Kybic, M. Desco, A. Santos, M. Suhling, P. Hunziker, and M. Unser, "Spatio-temporal nonrigid registration for ultrasound cardiac motion estimation," *IEEE Trans Med Imaging*, Vol. 24, no. 9, pp. 1113–26, 2005.

110. Ledesma-Carbayo, M. J., P. MahÃa-Casado, A. Santos, E. PÃ©rez-David, M. A. GarcÃa-FernÃ¡ndez, and M. Desco, "Cardiac motion analysis from ultrasound sequences using nonrigid registration: Validation against doppler tissue velocity," *Ultrasound in Medicine & Biology*, Vol. 32, no. 4, pp. 483–490, 2006.

111. Klein, A., J. Andersson, B. A. Ardekani, J. Ashburner, B. Avants, M. C. Chiang, G. E. Christensen, D. L. Collins, J. Gee, P. Hellier, J. H. Song, M. Jenkinson, C. Lepage, D. Rueckert, P. Thompson, T. Vercauteren, R. P. Woods, J. J. Mann, and R. V. Parsey, "Evaluation of 14 nonlinear deformation algorithms applied to human brain mri registration," *Neuroimage*, Vol. 46, no. 3, pp. 786–802, 2009.

112. Chang, J., T. S. Suh, and D. S. Lee, "Development of a deformable lung phantom for the evaluation of deformable registration," *J Appl Clin Med Phys*, Vol. 11, no. 1, p. 3081, 2010.

113. Fedorov, A., E. Billet, M. Prastawa, G. Gerig, A. Radmanesh, S. K. Warfield, R. Kikinis, and N. Chrisochoides, "Evaluation of brain mri alignment with the robust hausdorff distance measures," *Advances in Visual Computing, Pt I, Proceedings*, Vol. 5358, pp. 594–603, 2008.

114. Vercauteren, T., X. Pennec, A. Perchant, and N. Ayache, "Diffeomorphic demons: efficient non-parametric image registration," *Neuroimage*, Vol. 45, no. 1 Suppl, pp. S61–72, 2009.

115. Swammerdam, J., *Bybel der natuure door Jan Swammerdam, Amsteldammer, of, Historie der insecten [microform] : tot zeekere zoorten gebracht : door voorbeelden, ontleedkundige onderzoekingen van veelerhande kleine gediertens, als ook door kunstige kopere*

plaaten opgeheldert : verrykt met ontelbaare waarnemingen van nooit ontdekte zeldzaamheden in de natuur / alles in de Hollandsche, des auteurs moedertaale, beschreven ; hier by komt een voorreeden, waar in het leven van den auteur beschreven is door Herman Boerhaave ; de Latynsche overzetting heeft bezorgt Hieronimus David Gaubius, Landmarks of science., Leyden: I. Severinus, B. Vander Aa, Pieter Vander Aa, 1737.

116. Baskin, R. J., and P. J. Paolini, "Muscle volume changes," *J Gen Physiol*, Vol. 49, no. 3, pp. 387–404, 1966.

117. Huyghe, J. M., T. Arts, D. H. van Campen, and R. S. Reneman, "Porous medium finite element model of the beating left ventricle," *Am J Physiol*, Vol. 262, no. 4 Pt 2, pp. H1256–67, 1992.

118. Wisnes, A., and A. KirkebÃ¸, "Regional distribution of blood flow in calf muscles of rat during passive stretch and sustained contraction," *Acta Physiologica Scandinavica*, Vol. 96, no. 2, pp. 256–266, 1976.

119. Sejersted, O. M., and A. R. Hargens, "Intramuscular pressures for monitoring different tasks and muscle conditions," *Adv Exp Med Biol*, Vol. 384, pp. 339–50, 1995.

120. Valic, Z., J. B. Buckwalter, and P. S. Clifford, "Muscle blood flow response to contraction: influence of venous pressure," *J Appl Physiol*, Vol. 98, no. 1, pp. 72–6, 2005.

121. Stranden, E., and A. Kroese, "Venodynamics in healthy subjects and in patients with venous dysfunction," *Scope on Phlebology and Lymphology*, Vol. 5, pp. 4–12, 1998.

122. Yucesoy, C. A., "Epimuscular myofascial force transmission implies novel principles for muscular mechanics," *Exerc Sport Sci Rev*, Vol. 38, no. 3, pp. 128–34, 2010.

123. Huijing, P. A., R. W. van de Langenberg, J. J. Meesters, and G. C. Baan, "Extramuscular myofascial force transmission also occurs between synergistic muscles and antagonistic muscles," *Journal of Electromyography and Kinesiology*, Vol. 17, no. 6, pp. 680–689, 2007.

124. Kubo, K., H. Kanehisa, Y. Kawakami, and T. Fukunaga, "Influence of static stretching on viscoelastic properties of human tendon structures in vivo," *J Appl Physiol*, Vol. 90, no. 2, pp. 520–7, 2001.

125. Nourbakhsh, M. R., and C. G. Kukulka, "Relationship between muscle length and moment arm on emg activity of human triceps surae muscle," *Journal of Electromyography and Kinesiology*, Vol. 14, no. 2, pp. 263–273, 2004.

126. Heemskerk, A. M., G. J. Strijkers, A. Vilanova, M. R. Drost, and K. Nicolay, "Determination of mouse skeletal muscle architecture using three-dimensional diffusion tensor imaging," *Magnetic Resonance in Medicine*, Vol. 53, no. 6, pp. 1333–1340, 2005.

127. Budzik, J., V. Le Thuc, X. Demondion, M. Morel, D. Chechin, and A. Cotten, "In vivo mr tractography of thigh muscles using diffusion imaging: initial results," *European Radiology*, Vol. 17, no. 12, pp. 3079–3085, 2007.

128. Yaman, A., G. Baan, P. Huijing, C. Ozturk, and C. Yucesoy, "In vivo human muscle mri shows myofascial force transmission induced serial inhomogeneity of sarcomere lengths," in *Workshop on Multi-Scale Muscle Mechanics*.

129. Hatakenaka, M., H. Yabuuchi, S. Sunami, T. Kamitani, Y. Takayama, K. Nishikawa, and H. Honda, "Joint position affects muscle proton diffusion: Evaluation with a 3-t mr system," *AJR Am J Roentgenol*, Vol. 194, no. 2, pp. W208–11, 2010.

130. Danowski, B. A., K. Imanaka-Yoshida, J. M. Sanger, and J. W. Sanger, "Costameres are sites of force transmission to the substratum in adult rat cardiomyocytes," *J Cell Biol*, Vol. 118, no. 6, pp. 1411–20, 1992.

131. Hijikata, T., H. Wakisaka, and S. Niida, "Functional combination of tapering profiles and overlapping arrangements in nonspanning skeletal muscle fibers terminating intrafascicularly," *Anat Rec*, Vol. 236, no. 4, pp. 602–10, 1993.

132. Huijing, P. A., "Muscle, the motor of movement: properties in function, experiment and modelling," *J Electromyogr Kinesiol*, Vol. 8, no. 2, pp. 61–77, 1998.

133. Yaman, A., C. Ozturk, P. A. Huijing, and C. A. Yucesoy, "Magnetic resonance imaging assessment of mechanical interactions between human lower leg muscles in vivo," *J Biomech Eng*, Vol. 135, no. 9, pp. 91003–9, 2013.

134. Cox, R. W., "Afni: Software for analysis and visualization of functional magnetic resonance neuroimages," *Computers and Biomedical Research*, Vol. 29, no. 3, pp. 162–173, 1996.

135. Mori, S., B. J. Crain, V. P. Chacko, and P. C. M. Van Zijl, "Three-dimensional tracking of axonal projections in the brain by magnetic resonance imaging," *Annals of Neurology*, Vol. 45, no. 2, pp. 265–269, 1999.

136. Englund, E. K., C. P. Elder, Q. Xu, Z. Ding, and B. M. Damon, "Combined diffusion and strain tensor mri reveals a heterogeneous, planar pattern of strain development during isometric muscle contraction," *Am J Physiol Regul Integr Comp Physiol*, Vol. 300, no. 5, pp. R1079–90, 2011.

137. Hatakenaka, M., H. Yabuuchi, Y. Matsuo, T. Okafuji, T. Kamitani, T. Setoguchi, K. Nishikawa, and H. Honda, "Effect of passive muscle length change on apparent diffusion coefficient: detection with clinical mr imaging," *Magn Reson Med Sci*, Vol. 7, no. 2, pp. 59–63, 2008.

138. Schwenzer, N. F., G. Steidle, P. Martirosian, C. Schraml, F. Springer, C. D. Claussen, and F. Schick, "Diffusion tensor imaging of the human calf muscle: distinct changes in fractional anisotropy and mean diffusion due to passive muscle shortening and stretching," *NMR Biomed*, Vol. 22, no. 10, pp. 1047–53, 2009.

139. Morgan, D. L., N. P. Whitehead, A. K. Wise, J. E. Gregory, and U. Proske, "Tension changes in the cat soleus muscle following slow stretch or shortening of the contracting muscle," *J Physiol*, Vol. 522 Pt 3, pp. 503–13, 2000.

140. Willems, M. E., and P. A. Huijing, "Heterogeneity of mean sarcomere length in different fibres: effects on length range of active force production in rat muscle," *Eur J Appl Physiol Occup Physiol*, Vol. 68, no. 6, pp. 489–96, 1994.

141. Poupon, C., A. Roche, J. Dubois, J. F. Mangin, and F. Poupon, "Real-time mr diffusion tensor and q-ball imaging using kalman filtering," *Med Image Anal*, Vol. 12, no. 5, pp. 527–34, 2008.

142. Casaseca-de-la Higuera, P., A. Tristan-Vega, S. Aja-Fernandez, C. Alberola-Lopez, C. F. Westin, and R. San Jose Estepar, "Optimal real-time estimation in diffusion tensor imaging," *Magn Reson Imaging*, Vol. 30, no. 4, pp. 506–17, 2012.

143. Manduca, A., T. E. Oliphant, M. A. Dresner, J. L. Mahowald, S. A. Kruse, E. Amromin, J. P. Felmlee, J. F. Greenleaf, and R. L. Ehman, "Magnetic resonance elastography: non-invasive mapping of tissue elasticity," *Med Image Anal*, Vol. 5, no. 4, pp. 237–54, 2001.

144. Mariappan, Y. K., K. J. Glaser, and R. L. Ehman, "Magnetic resonance elastography: a review," *Clin Anat*, Vol. 23, no. 5, pp. 497–511, 2010.

145. Bensamoun, S. F., S. I. Ringleb, L. Littrell, Q. Chen, M. Brennan, R. L. Ehman, and K. N. An, "Determination of thigh muscle stiffness using magnetic resonance elastography," *J Magn Reson Imaging*, Vol. 23, no. 2, pp. 242–7, 2006.

146. Garfin, S. R., C. M. Tipton, S. J. Mubarak, S. L. Woo, A. R. Hargens, and W. H. Akeson, "Role of fascia in maintenance of muscle tension and pressure," *J Appl Physiol Respir Environ Exerc Physiol*, Vol. 51, no. 2, pp. 317–20, 1981.

147. Lundon, K., *The effect of mechanical load on soft connective tissues.*, ch. 2, pp. 15–30. Boston, MA: Bartlett and Jones Publishers, 2007.

148. Yang, G., H. J. Im, and J. H. Wang, "Repetitive mechanical stretching modulates il-1beta induced cox-2, mmp-1 expression, and pge2 production in human patellar tendon fibroblasts," *Gene*, Vol. 363, pp. 166–72, 2005.

149. Nicolakis, P., C. B. Erdogmus, J. Kollmitzer, K. Kerschan-Schindl, M. Sengstbratl, M. Nuhr, R. Crevenna, and V. Fialka-Moser, "Long-term outcome after treatment of temporomandibular joint osteoarthritis with exercise and manual therapy," *Cranio : the journal of craniomandibular practice*, Vol. 20, no. 1, pp. 23–27, 2002.

150. Gross, A. R., T. Kay, M. Hondras, C. Goldsmith, T. Haines, P. Peloso, C. Kennedy, and J. Hoving, "Manual therapy for mechanical neck disorders: a systematic review," *Man Ther*, Vol. 7, no. 3, pp. 131–49, 2002.

151. Jensen, O., F. Nielsen, and L. Vosmar, "An open study comparing manual therapy with the use of cold packs in the treatment of post-traumatic headache," *Cephalalgia*, Vol. 10, no. 5, pp. 241–250, 1990.

152. Ceelen, K. K., A. Stekelenburg, J. L. Mulders, G. J. Strijkers, F. P. Baaijens, K. Nicolay, and C. W. Oomens, "Validation of a numerical model of skeletal muscle compression with mr tagging: a contribution to pressure ulcer research," *J Biomech Eng*, Vol. 130, no. 6, p. 061015, 2008.

153. Chaudhry, H., R. Schleip, Z. Ji, B. Bukiet, M. Maney, and T. Findley, "Three-dimensional mathematical model for deformation of human fasciae in manual therapy," *J Am Osteopath Assoc*, Vol. 108, no. 8, pp. 379–90, 2008.

154. Chaudhry, H., B. Bukiet, and T. Findley, "Mathematical analysis of applied loads on skeletal muscles during manual therapy," *J Am Osteopath Assoc*, Vol. 108, no. 12, pp. 680–8, 2008.

155. Loghmani, M. T., and S. J. Warden, "Instrument-assisted cross-fiber massage accelerates knee ligament healing," *J Orthop Sports Phys Ther*, Vol. 39, no. 7, pp. 506–14, 2009.

156. Meltzer, K. R., and P. R. Standley, "Modeled repetitive motion strain and indirect osteopathic manipulative techniques in regulation of human fibroblast proliferation and interleukin secretion," *J Am Osteopath Assoc*, Vol. 107, no. 12, pp. 527–36, 2007.

157. Hicks, M. R., T. V. Cao, D. H. Campbell, and P. R. Standley, "Mechanical strain applied to human fibroblasts differentially regulates skeletal myoblast differentiation," *J Appl Physiol (1985)*, Vol. 113, no. 3, pp. 465–72, 2012.

158. Meltzer, K. R., T. V. Cao, J. F. Schad, H. King, S. T. Stoll, and P. R. Standley, "In vitro modeling of repetitive motion injury and myofascial release," *J Bodyw Mov Ther*, Vol. 14, no. 2, pp. 162–71, 2010.

159. Wang, J. H., F. Jia, G. Yang, S. Yang, B. H. Campbell, D. Stone, and S. L. Woo, "Cyclic mechanical stretching of human tendon fibroblasts increases the production of prostaglandin e2 and levels of cyclooxygenase expression: a novel in vitro model study," *Connect Tissue Res*, Vol. 44, no. 3-4, pp. 128–33, 2003.

160. Threlkeld, A. J., "The effects of manual therapy on connective tissue," *Phys Ther*, Vol. 72, no. 12, pp. 893–902, 1992.

161. Kureshi, A., P. Vaiude, S. N. Nazhat, A. Petrie, and R. A. Brown, "Matrix mechanical properties of transversalis fascia in inguinal herniation as a model for tissue expansion," *J Biomech*, Vol. 41, no. 16, pp. 3462–8, 2008.

162. Toyoda, T., S. Saito, S. Inokuchi, and Y. Yabe, "The effects of tensile load on the metabolism of cultured chondrocytes," *Clin Orthop Relat Res*, no. 359, pp. 221–8, 1999.

163. Buckley, M. J., A. J. Banes, L. G. Levin, B. E. Sumpio, M. Sato, R. Jordan, J. Gilbert, G. W. Link, and R. Tran Son Tay, "Osteoblasts increase their rate of division and align in response to cyclic, mechanical tension in vitro," *Bone Miner*, Vol. 4, no. 3, pp. 225–36, 1988.

164. Chen, Q., S. Bensamoun, J. R. Basford, J. M. Thompson, and K. N. An, "Identification and quantification of myofascial taut bands with magnetic resonance elastography," *Arch Phys Med Rehabil*, Vol. 88, no. 12, pp. 1658–61, 2007.

165. Chen, Q., J. Basford, and K. N. An, "Ability of magnetic resonance elastography to assess taut bands," *Clin Biomech (Bristol, Avon)*, Vol. 23, no. 5, pp. 623–9, 2008.

166. Travell, J. G., and D. G. Simons, *Myofascial Pain and Dysfunction*, Vol. 2, Philadelphia, PA: Lippincott Williams & Wilkins, 1992.

167. Dommerholt, J., and C. F. d. l. Peñas, *Trigger Point Dry Needling: An Evidence and Clinical-Based Approach*, London: Elsevier Health Sciences, 2013.

168. Ge, H. Y., Y. Zhang, S. Boudreau, S. W. Yue, and L. Arendt-Nielsen, "Induction of muscle cramps by nociceptive stimulation of latent myofascial trigger points," *Exp Brain Res*, Vol. 187, no. 4, pp. 623–9, 2008.

169. Xu, Y. M., H. Y. Ge, and L. Arendt-Nielsen, "Sustained nociceptive mechanical stimulation of latent myofascial trigger point induces central sensitization in healthy subjects," *J Pain*, Vol. 11, no. 12, pp. 1348–55, 2010.

170. Prateepavanich, P., V. Kupniratsaikul, and T. Charoensak, "The relationship between myofascial trigger points of gastrocnemius muscle and nocturnal calf cramps," *J Med Assoc Thai*, Vol. 82, no. 5, pp. 451–9, 1999.

171. Nguyen, B. M., "Trigger point therapy and plantar heel pain: A case report," *Foot (Edinb)*, Vol. 20, no. 4, pp. 158–62, 2010.

172. Renan-Ordine, R., F. Alburquerque-Sendin, D. P. de Souza, J. A. Cleland, and C. Fernandez-de Las-Penas, "Effectiveness of myofascial trigger point manual therapy combined with a self-stretching protocol for the management of plantar heel pain: a randomized controlled trial," *J Orthop Sports Phys Ther*, Vol. 41, no. 2, pp. 43–50, 2011.

173. Williams, S., C. Whatman, P. A. Hume, and K. Sheerin, "Kinesio taping in treatment and prevention of sports injuries: a meta-analysis of the evidence for its effectiveness," *Sports Med*, Vol. 42, no. 2, pp. 153–64, 2012.